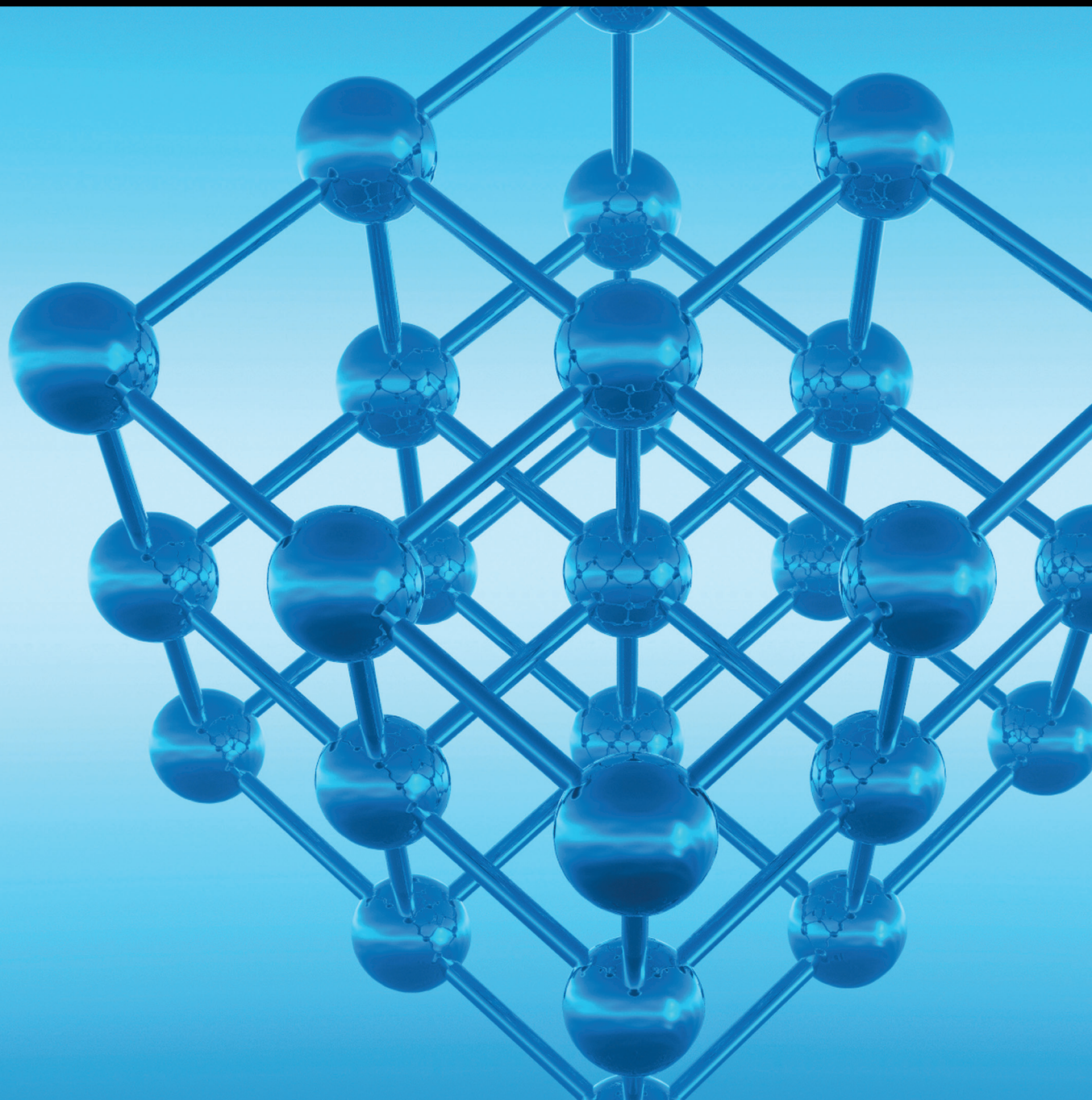


Photonics and Optoelectronics of Low-Dimensional Materials

Lead Guest Editor: Shenghuang Lin

Guest Editors: Gongxun Bai, Zhike Liu, Zaiquan Xu, and Zhixin Hu





Photonics and Optoelectronics of Low-Dimensional Materials

Advances in Condensed Matter Physics

Photonics and Optoelectronics of Low-Dimensional Materials

Lead Guest Editor: Shenghuang Lin

Guest Editors: Gongxun Bai, Zhike Liu, Zaiquan Xu,
and Zhixin Hu



Copyright © 2018 Hindawi. All rights reserved.

This is a special issue published in "Advances in Condensed Matter Physics." All articles are open access articles distributed under the Creative Commons Attribution License, which permits unrestricted use, distribution, and reproduction in any medium, provided the original work is properly cited.

Editorial Board

Bohdan Andraka, USA

Ward Beyermann, USA

Golam M. Bhuiyan, Bangladesh

Luis L. Bonilla, Spain

Ashok Chatterjee, India

Ram N. P. Choudhary, India

Oleg Derzhko, Ukraine

Gayanan Fernando, USA

Jörg Fink, Germany

Yuri Galperin, Norway

Prasenjit Guptasarma, USA

Da-Ren Hang, Taiwan

Jan A. Jung, Canada

Joseph S. Poon, USA

Leonid Pryadko, USA

Charles Rosenblatt, USA

Mohindar S. Seehra, USA

Sergei Sergeenkov, Brazil

Sergio E. Ulloa, USA

Markus R. Wagner, Germany

Gary Wysin, USA

Kiyokazu Yasuda, Japan

Fajun Zhang, Germany

Jiandi Zhang, USA

Contents

Photonics and Optoelectronics of Low-Dimensional Materials

Shenghuang Lin , Gongxun Bai , Zhike Liu, Zaiquan Xu, and Zhixin Hu
Editorial (2 pages), Article ID 7176029, Volume 2018 (2018)

Effects of Deposition Temperature on Structural, Optical Properties and Laser Damage of LaTiO₃ Thin Films

Jianchao Li, Wanmin Yang , Junhong Su, and Chen Yang
Research Article (6 pages), Article ID 7328429, Volume 2018 (2018)

Research on a Micro-Nano Si/SiGe/Si Double Heterojunction Electro-Optic Modulation Structure

Song Feng , Lian-bi Li , and Bin Xue
Research Article (8 pages), Article ID 8297650, Volume 2018 (2018)

Fabrication and Characterization of Two-Dimensional Layered MoS₂ Thin Films by Pulsed Laser Deposition

Lei Jiao, Yuehui Wang, Yusong Zhi, Wei Cui, Zhengwei Chen, Xiao Zhang, Wenjing Jie, and Zhenping Wu 
Research Article (5 pages), Article ID 3485380, Volume 2018 (2018)

Quantum Simulations of Charge Separation at a Model Donor-Acceptor Interface: Role of Delocalization and Local Packing

Allen Kelley, Kush Patel, and Eric R. Bittner 
Research Article (10 pages), Article ID 6834908, Volume 2018 (2018)

Temperature Dependence of the Energy Band Diagram of AlGaN/GaN Heterostructure

Yanli Liu , Dunjun Chen , Kexiu Dong, Hai Lu, Rong Zhang, Youdou Zheng, Zhilin Zhu, Guangfen Wei, and Zhonghai Lin
Research Article (4 pages), Article ID 1592689, Volume 2018 (2018)

Structural and Optical Properties of α -Quartz Cluster with Oxygen-Deficiency Centers

Yin Li , Xi Chen , Chuanghua Yang, Liyuan Wu, and Ru Zhang 
Research Article (9 pages), Article ID 2564803, Volume 2018 (2018)

First-Principles Calculations on Atomic and Electronic Properties of Ge/4H-SiC Heterojunction

Bei Xu, Changjun Zhu, Xiaomin He, Yuan Zang, Shenghuang Lin, Lianbi Li , Song Feng , and Qianqian Lei
Research Article (9 pages), Article ID 8010351, Volume 2018 (2018)

External Electric Field Effect on Shallow Donor Impurity States in Zinc-Blende In_xGa_{1-x}N/GaN Symmetric Coupled Quantum Dots

Guang-Xin Wang, Li-Li Zhang, and Huan Wei
Research Article (7 pages), Article ID 5652763, Volume 2017 (2018)

Surface Plasmon Resonance Enhanced Spontaneous Upconversion and Stimulated Emissions in Glass Ceramics Containing Ba₂LaF₇ Nanocrystals

Sai Li, Wei Lu, Qihua Yang, Dacheng Zhou, Jianbei Qiu, Xuhui Xu, and Xue Yu
Research Article (6 pages), Article ID 5304791, Volume 2017 (2018)

Editorial

Photonics and Optoelectronics of Low-Dimensional Materials

Shenghuang Lin ,¹ Gongxun Bai ,² Zhike Liu,³ Zaiquan Xu,⁴ and Zhixin Hu⁵

¹Department of Applied Physics, The Hong Kong Polytechnic University, Hung Hom, Hong Kong

²College of Materials Science and Engineering, China Jiliang University, Hangzhou, China

³School of Materials Science and Engineering, Shaanxi Normal University, Xi'an, China

⁴Materials and Nanoscale Physics, University of Technology Sydney, Ultimo, NSW, Australia

⁵Department of Chemistry and Institute of Optical Sciences, University of Toronto, Toronto, ON, Canada

Correspondence should be addressed to Gongxun Bai; g.x.bai@connect.polyu.hk

Received 3 April 2018; Accepted 3 April 2018; Published 3 June 2018

Copyright © 2018 Shenghuang Lin et al. This is an open access article distributed under the Creative Commons Attribution License, which permits unrestricted use, distribution, and reproduction in any medium, provided the original work is properly cited.

Recently, the study of low-dimensional materials has gained significant interest for a variety of photonic and optoelectronic applications. Low-dimensional materials exist in a kind of systems in which electronic state wavefunction is confined, at least in one of the three dimensions. Decreasing the dimensionality of the materials to the nanoscale in one, two, or three directions leads to thin film structures (2D), wires (1D), or dots (0D), respectively. Thus the low materials possessing quantum size effects have significantly changed their electronic properties and deeply modified their photonic and optoelectronic performances when compared with their bulk form. Due to their varied electronic and optical properties, low materials have been utilized for a wide range of applications, such as transistors, nonlinear optics, ultrafast optics, electrooptic modulator, photovoltaics, plasmonics, and photodetectors. The importance to these device applications is an enhanced understanding of fundamental structural, electronic, optical, quantum simulations, thermal, and luminescent properties. In this special issue, several authors have been invited to submit original research articles that will motivate the continuing efforts to study the basic physical properties of low-dimensional materials.

Photonic composite containing both Yb^{3+} , Er^{3+} codoped Ba_2LaF_7 and Ag nanocrystals has been fabricated through the melt-quenching and heating treatment method. Due to the surface plasmon resonance of Ag nanoparticles, spontaneous upconversion and stimulated emissions from Yb^{3+} , Er^{3+} ions have been efficiently enhanced in Ba_2LaF_7 nanocrystals. The result suggests an effective way to improve the luminescent

performance for upconversion materials. Based on the effective-mass approximation and variational procedure, the external electric field effect on shallow-donor impurity states has been investigated in zinc-blende $\text{In}_x\text{Ga}_{1-x}\text{N}/\text{GaN}$ symmetric coupled quantum dots. The donor binding energy is studied as a function of the dot thickness, the dot radius, the external electric field, and the impurity position.

Temperature dependence of the energy band diagram of AlGaN/GaN heterostructure has been studied by D. Chen et al. through theoretical calculation and experiment. Their work offers important theoretical and experimental basis for the performance degradation of AlGaN/GaN high electron mobility transistors with increasing temperature. Based on first-principles calculations, the atomic and electronic properties of Ge/4H-SiC heterojunction have been investigated by L. Li et al. Considering the importance in silicon photonics, S. Feng et al. have studied a micro-nano Si/SiGe/Si double heterojunction electron-optic modulation structure. Based on the density functional theory, the structural and optical properties of α -quartz cluster with oxygen-deficiency centers defects have been studied by R. Zhang et al.

Z. Wu et al. have reported the structural and transport properties of wafer-scale 2D layered materials fabricated by pulsed laser deposition method. Based on the deposited uniform 2D few-layer MoS₂, back-gated field effect transistors have been developed. The growth parameters have important effects on the photonic and electronic properties of the thin films. The effects of deposition temperature on structural, optical properties and laser damage of LaTiO₃ thin films

have been studied by C. Yang et al. Organic polymer-based photovoltaic systems provide a practicable alternate to more standard solid-state devices for solar-harvesting applications. A. Kelley et al. have investigated roles of delocalization and local packing based on quantum simulations of charge-separation at a model donor-acceptor interface.

It is believed that the publication of this special issue will be of reference value for readers working in the areas related to low-dimensional materials for photonic and optoelectronic applications.

*Shenghuang Lin
Gongxun Bai
Zhike Liu
Zaiquan Xu
Zhixin Hu*

Research Article

Effects of Deposition Temperature on Structural, Optical Properties and Laser Damage of LaTiO₃ Thin Films

Jianchao Li,^{1,2} Wanmin Yang,¹ Junhong Su,² and Chen Yang²

¹School of Physics and Information Technology, Shaanxi Normal University, Xi'an 710062, China

²School of Photo-Electrical Engineering, Xi'an Technological University, Xi'an 710021, China

Correspondence should be addressed to Wanmin Yang; yangwm@snnu.edu.cn

Received 21 December 2017; Accepted 15 March 2018; Published 2 May 2018

Academic Editor: Gongxun Bai

Copyright © 2018 Jianchao Li et al. This is an open access article distributed under the Creative Commons Attribution License, which permits unrestricted use, distribution, and reproduction in any medium, provided the original work is properly cited.

LaTiO₃ films were prepared under various deposition temperatures using electron beam evaporation on Si and fused quartz substrates. The relationship between the deposition temperature and structure and properties of optics was investigated by XPS, XRD, and various optical testing. The results showed that the LaTiO₃ film is amorphous when the deposition temperature is below 200°C. The refractive index of LaTiO₃ films increases from 1.8302 to 1.9112 at 1064 nm with the rise of deposition temperature. The extinction coefficient of LaTiO₃ films is less than 10⁻⁶ in the range of 350 to 1700 nm. The laser damage threshold increases at first and then decreases with the increase of deposition temperature. The maximum of the laser damage threshold was 18.18 J/cm² when the deposition temperature was 150°C. Compared with TiO₂ film, the chemical structure and the laser damage threshold of LaTiO₃ film are more stable by preparation of electron beam evaporation.

1. Introduction

Thin films began to be applied in the 1930s, and now it has been widely used in optics, microelectronics, materials, and other fields. However, with the application of high-power laser, the optical thin film which is an important part of the optical system has become a weak segment. For decades, the researchers have done a lot of work on improving the damage threshold of the thin film in optics field. For high refractive index materials, researchers focused on HfO₂, TiO₂, ZrO₂, and so on [1–5].

In recent years, with the discovery of high-temperature superconductivity and the development of its physical mechanism, the physical properties of LaTiO₃ due to the strong correlation of La-Ti-O doped with Ag, Cu, Fe, or Sr were extensively researched [6–9]. Meanwhile, the studies indicated that the performance of TiO₂ would be improved by La₂O₃ doped and obtained a high stability refractive index material—LaTiO₃ [10, 11]. Based on that, Philippe Combette studied the morphology, structure, nonconductivity, and dielectric properties of LaTiO₃ films under different deposition parameters (RF power, deposition pressure, and

deposition temperature) [12]. Su Junhong studied the effect of deposition temperature on optical properties and laser damage characteristics of LaTiO₃ films [13]. However, few studies have made a systematic study on the relationship between structure and optical properties of LaTiO₃ thin films.

As we know, the preparing parameters have an important effect on the properties of the film [14, 15]. Therefore, the effects of deposition temperature on the optical and the laser damage properties of LaTiO₃ thin films were studied in this paper.

2. Experimental

LaTiO₃ films were deposited by electron beam evaporation (ZZS500-1/G Chengdu Nanguang Vacuum Technology Co. Ltd., China) on Si (100) and fused quartz substrates. The films were deposited by using the LaTiO₃ pellets (purity 99.99%, provided by Beijing Nonferrous Metal Research Institute) as starting material. Si (100) and fused quartz substrates were cleaned ultrasonically in alcohol solution before deposition. The base pressure was 3×10^{-3} Pa and the working pressure was 2×10^{-2} Pa, oxygen was introduced in the vacuum

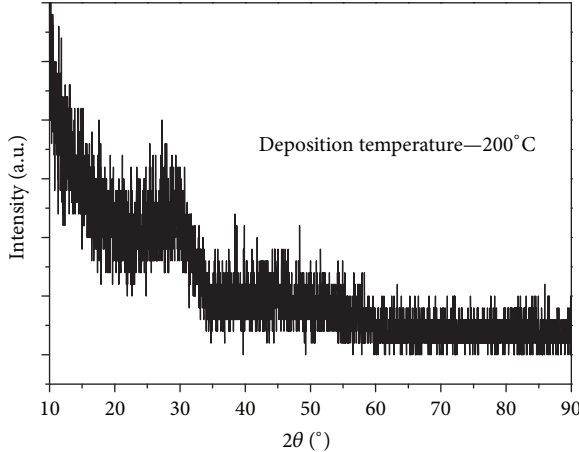


FIGURE 1: XRD spectra of sample deposited at 200°C.

chamber and the gas flow was kept at 4 sccm, the electron beam current was 110 mA, and the deposition temperature, respectively, was 50, 75, 100, 125, 150, 175, and 200°C.

Optical parameters of the LaTiO₃ films, including refractive indexes, extinction coefficient, and physical thickness, were measured by spectroscopic ellipsometry (J.A. Woollam M-2000UI, American). The structure of the samples was measured by X-ray diffraction (XRD, X'Pert PRO MPD) with 2θ angle in the range of 10–90° at room temperature. The transmission spectra of the films were measured by spectrophotometer (HitachiU-3501, Japan). The elemental composition and the element's chemical states of the as-deposited LaTiO₃ films were investigated by X-ray photoelectron spectroscopy (XPS, PHI5400). Laser damage characteristics of LaTiO₃ films were measured by the film and optical element laser damage threshold testing instrument. The laser induced damage threshold (LIDT) of thin films was measured in “1-on-1” regime according to ISO standard 11254-1 by means of 1064 nm Q-switch pulsed laser with a pulse length of 10 ns.

3. Result and Discussion

3.1. Different Deposition Temperature

3.1.1. X-Ray Diffraction Analysis. The XRD spectra shown in Figure 1 revealed that no apparent diffraction peak can be found but an amorphous package around $2\theta = 28^\circ$. It means that the film even deposited at the highest temperature of 200°C is still amorphous.

3.1.2. XPS Spectrum Analysis. Figure 2 shows the XPS characteristic spectra of La, Ti, O, and contamination C, which were detected in the XPS survey spectra of the film prepared at 125°C. The peak of Ti2p3 of 457.97 eV in Figure 2 was close to the value of 457.80 eV in Ti₂O₃ [16]. The peak of La3d5 was 834.12 eV corresponding to 834.80 eV of La₂O₃ [17]. It indicated that the film was essentially composed of La₂O₃ and Ti₂O₃. The XPS results of films deposited at different temperatures are listed in Table 1. It showed that

the ratio of total La and Ti atomic content to O atomic content was approximated to 2:3 and increased slightly with the increase of deposition temperature. It indicates that the increase of deposition temperature benefited the formation of LaTiO₃. Meanwhile, the change of the ratio was not obvious, indicating that the evaporation is stability.

3.1.3. Optical Properties. Optical properties can be characterized by refractive index and transmittance which are important parameters for optical applications [18]. The results of optical constants *n* and *k* of LaTiO₃ films were shown in Figure 3. As shown in Figure 3(a), the refractive index increases with the rise of the deposition temperature in the wavelength range from 350 to 1700 nm. From the analysis of XPS results, it has been known that the difference in composition of the film is small. Therefore, the increase in refractive index could be the major mobility of the film atoms on the substrate at higher deposition temperatures, which would help to achieve high aggregation densities and lead to the increase in the refractive index. Simultaneously, Figure 3(a) showed that the refractive index increased from 1.8302 to 1.9112 at the wavelength of 1064 nm with a small variation of 0.081. However, some studies have shown that the refractive index of TiO₂ films dramatically increases from 1.8458 to 2.0721 when the substrate temperature increased from 50 to 250°C [19]. The variation is as high as 0.2263. Consequently, the refractive index change of LaTiO₃ films is much smaller than that of TiO₂ film with the same change of deposition temperature. In other words, LaTiO₃ film is better than TiO₂ film in structural stability at different deposition temperatures. In addition, some researcher concluded that the refractive index of TiO₂ film deposited by electron beam evaporation at 200°C is 2.07–1.95 in the wavelength of 400–900 nm, while the refractive index of LaTiO₃ film is 2.04–1.93 under the same conditions. Obviously, the refractive index of LaTiO₃ film is almost equal to that of TiO₂ film. From Figure 3(b), it can be seen that the extinction coefficient of all samples is less than 10^{-6} in the wavelength range of 350 to 1700 nm, which showed that the absorption of the film was smaller.

The transmission spectra of samples at different deposition temperatures were shown in Figure 4. With the exception of the transmittance less than 80% at range of 424–480 nm due to optical interference, it can be observed that the transmittance of all samples are greater than 80% at wavelengths over 330 nm. The transmittance curves of 500–700 nm wavelength range were shown in Figure 4. As shown, the higher the deposition temperature, the closer the maximum transmittance of the LaTiO₃ film and the substrate transmittance. At the wavelength of 592 nm, the highest transmittance 93.44% occurs in the 200°C deposited film, which is very close to the substrate transmittance of 93.47%. Coinciding with extinction coefficient curve, the results of transmittance indicated LaTiO₃ films could be used as excellent transparent layers.

3.1.4. Laser Damage Property. In general, multilayer optical coatings were prepared by alternative depositing high and low

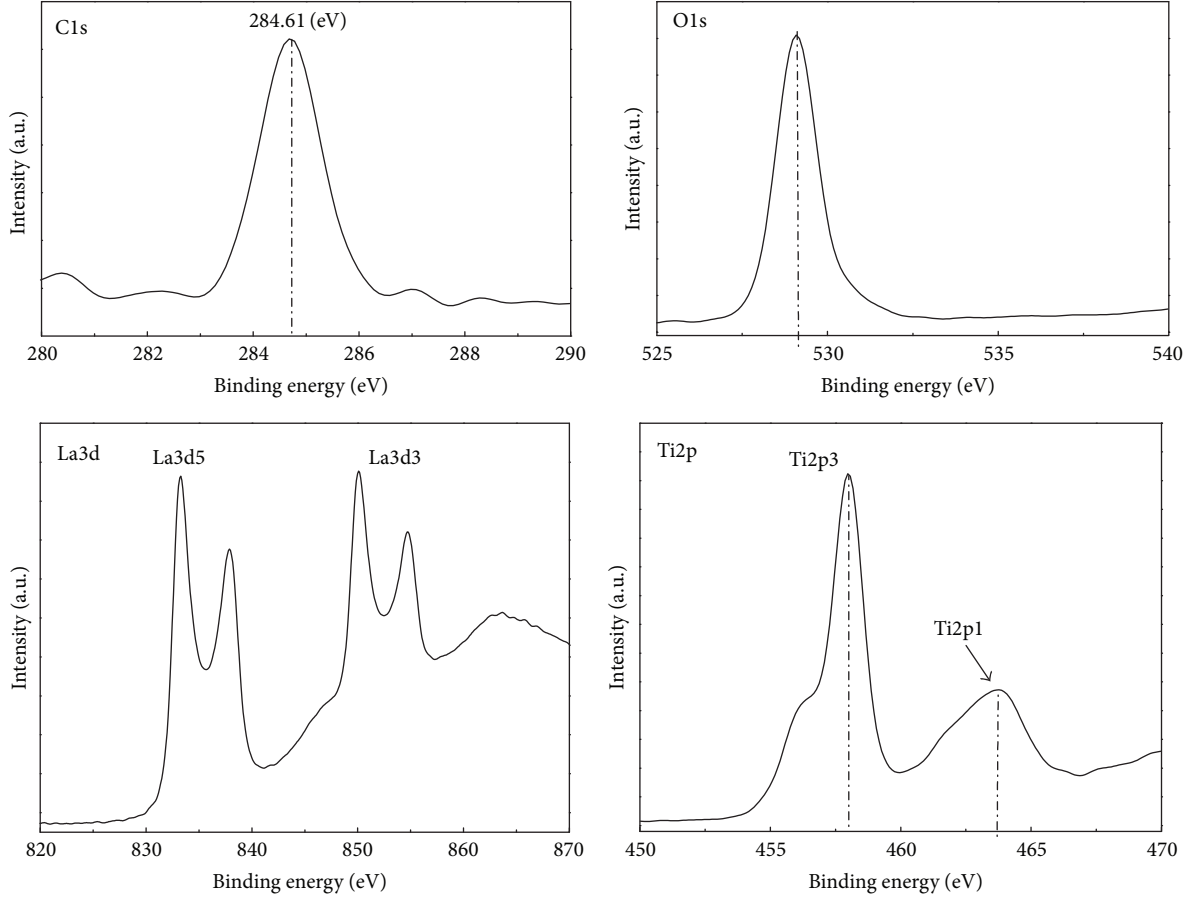


FIGURE 2: XPS spectra of four elements La, Ti, O, and C.

TABLE 1: Content of elements in the films prepared at different deposition temperature.

| Deposition temperature | At (%) | | | | |
|------------------------|--------|-------|-------|-------|--------------------|
| | C1s | La3d | O1s | Ti2p | (La3d + Ti2p): O1s |
| 50 | 6.01 | 22.42 | 58.29 | 13.28 | 0.6125 |
| 75 | 5.79 | 22.27 | 58.82 | 13.12 | 0.6017 |
| 100 | 4.32 | 22.61 | 59.85 | 13.22 | 0.5987 |
| 125 | 4.58 | 22.87 | 59.36 | 13.19 | 0.6075 |
| 150 | 2.46 | 23.30 | 60.74 | 13.50 | 0.6059 |
| 175 | 2.98 | 23.53 | 60.00 | 13.49 | 0.6170 |
| 200 | 3.65 | 23.83 | 58.88 | 13.64 | 0.6364 |

refractive index materials. The high refractive index materials were metal oxide material mostly, which were prone to lose oxygen during deposition process and became a shortcoming of multilayer film in the field of laser damage. Therefore, it was necessary to study the laser damage properties of LaTiO_3 films.

The surface damage morphologies of LaTiO_3 films prepared at 50, 150, and 200°C have been presented in Figure 5. This group of experiments was performed at 180 mJ pulsed laser energy. The damage performance of films deposited at different temperatures was directly analyzed from the damage spot area. As shown in Figure 5, all the samples were

damaged. Among them, the shedding area on the surface of the film deposited at 50°C was the largest one, which indicated the film damage was the most serious. When the deposition temperature was from 150 to 200°C, the shedding area was increased slightly. However, in general, there is no significant difference in damage morphologies of the films prepared at different deposition temperatures.

The LIDT of different deposition temperatures were shown in Figure 6. The LIDT increased with the rise of deposition temperature from 50 to 150°C. The maximum value of LIDT was 18.18 J/cm² at 150°C. However, the LIDT start to decrease when the deposition temperature was higher

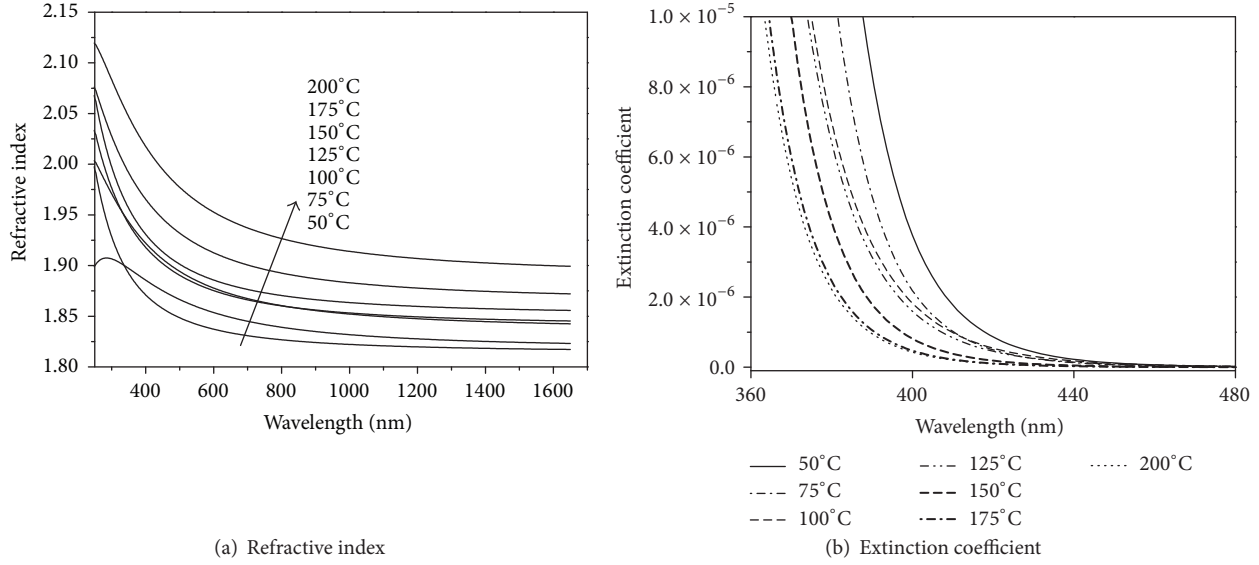


FIGURE 3: Refractive index (a) and extinction coefficient (b) of samples.

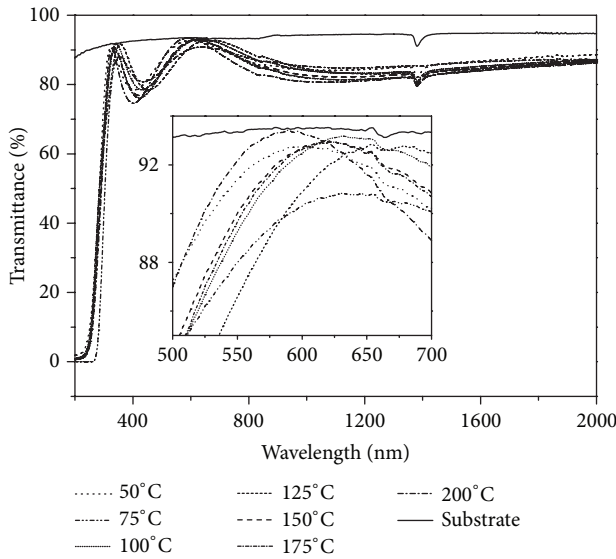


FIGURE 4: Transmittance curve of the films prepared at different deposition temperatures.

than 150°C. The LIDT of the 200°C deposited film closing to 15.91 J/cm² of the 50°C one reaches to 15.78 J/cm². It can be seen that the LIDT of the film did not change monotonically with the increase of deposition temperature and it was the maximum at 150°C.

In combination with XPS analysis, it was found that composition of the film prepared at different temperatures changed slightly so as to have little effect on the LIDT. Therefore, the depositing temperature became the main factor to affect the laser damage property. It concludes that the higher LIDT can be obtained at the higher depositing temperature. Firstly, at the higher deposition temperature the film had higher concentration density and thermal capacity

than that at the lower deposition temperature. Secondly, the higher deposition temperature not only improved the hardness of the films but also enhanced the adhesion between film and substrate. These results dramatically improved the film against the rapid heat expansion when the high energy laser propagated in the film. Finally, the higher deposition temperatures make the atoms of the film to gain more kinetic energy, which would increase the atomic migration velocity and reduce the defects of the film. However, the higher temperature also leads to an increasing internal stress of film, which can be observed from the crack around damage boundary of the film prepared at 200°C and results in the decrease in LIDT.

Compared with the TiO₂ film [20], the LIDT of LaTiO₃ film is about 15.78–18.18 J/cm², which is higher than that of TiO₂ film deposited at 200°C about 4.2 J/cm².

4. Conclusion

The deposition parameters have important effects on the performance of the film. The deposition temperature effects on structural and optical properties and laser damage of LaTiO₃ thin films were studied in this paper. The results show that the refractive index of LaTiO₃ film increased with substrate temperature. The extinction coefficient was less than 10^{-6} in the wavelength range of 350 to 1700 nm, which shows that the absorption of LaTiO₃ film is very small. It can be used as an ideal optical coating material. The LIDT increases at first and then decreases with increase of deposition temperature, and the maximum is 18.18 J/cm² at the deposition temperature of 150°C and is higher than TiO₂ film. But all the differences of performance were small and were insensitive to deposition temperature. Overall, process stability of the LaTiO₃ film is better than those of TiO₂ film. The LaTiO₃ film is an excellent optical coating and laser protection material.

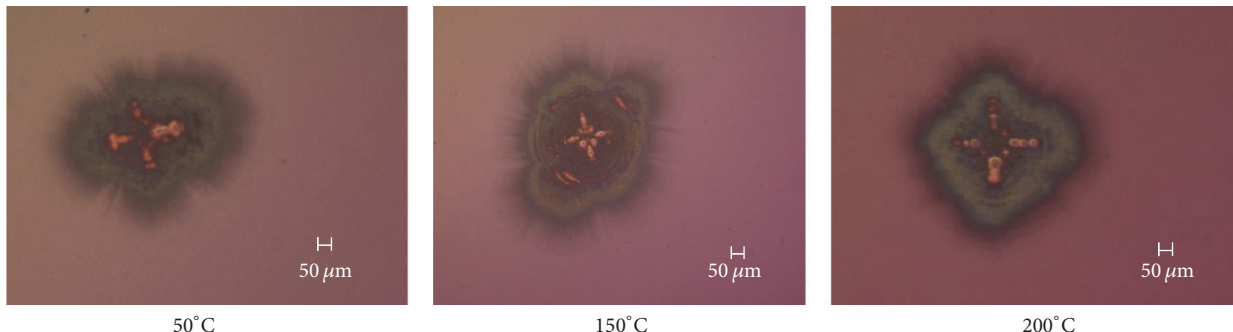


FIGURE 5: Damage morphologies of LaTiO_3 film prepared at different deposition temperature.

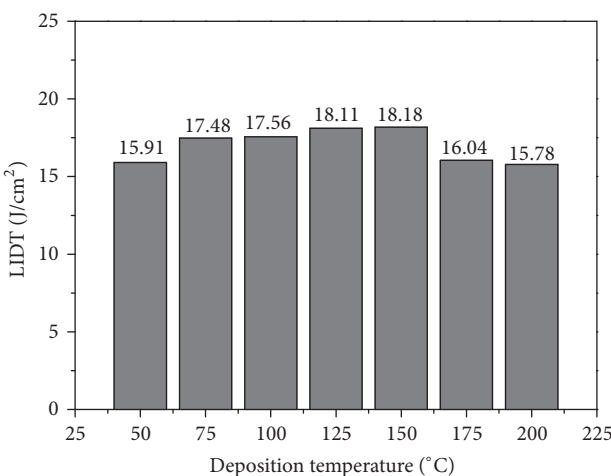


FIGURE 6: LIDT of LaTiO_3 film prepared at different deposition temperatures.

Conflicts of Interest

The authors declare that they have no conflicts of interest.

Acknowledgments

This work is supported by National Natural Science Foundation of China (Grant no. 61378050 and no. 61704134), the Scientific Research Programs Funded by Shaanxi Provincial Education Department (Program no. 17JS046), and the Open Fund of Shaanxi Province Key Laboratory of Thin Films Technology and Optical Test (Program no. ZSKJ201704).

References

- [1] D.-B. Douti, L. Gallais, and M. Commandré, "Laser-induced damage of optical thin films submitted to 343, 515, and 1030 nm multiple subpicosecond pulses," *Optical Engineering*, vol. 53, no. 12, Article ID 122509, 2014.
- [2] A. Hassanpour and A. Bananej, "The effect of time-temperature gradient annealing on microstructure, optical properties and laser-induced damage threshold of TiO_2 thin films," *Optik - International Journal for Light and Electron Optics*, vol. 124, no. 1, pp. 35–39, 2013.
- [3] A. Bananej and A. Hassanpour, "Modification of laser induced damage threshold of ZrO_2 thin films by using time-temperature gradient annealing," *Applied Surface Science*, vol. 258, no. 7, pp. 2397–2403, 2012.
- [4] C. Shunli, Z. Yuan'an, and L. Dawei, "Effect of nanosecond laser pre-irradiation on the femtosecond laser-induced damage of $\text{Ta}_2\text{O}_5/\text{SiO}_2$ high reflector," *Applied Optics*, vol. 51, no. 10, pp. 1495–1502, 2012.
- [5] A. Khalil, K. Farah, R. M. Shahid, A. Mahmood, S. Atiq, and Y. S. Al-Zaghayer, "High Dielectric Constant Study of TiO_2 -Polypyrrole Composites with Low Contents of Filler Prepared by In Situ Polymerization," *Advances in Condensed Matter Physics*, vol. 2016, Article ID 4793434, 2016.
- [6] Y. Chen, Y. Cui, and J.-E. Yao, "Dielectric characteristics of Fe-doped $\text{LaTiO}_3+\delta$ and visible light modulation," *RSC Advances*, vol. 6, no. 103, pp. 101571–101577, 2016.
- [7] F.-F. Jia, H. Zhong, W.-G. Zhang et al., "A novel nonenzymatic ECL glucose sensor based on perovskite $\text{LaTiO}_3\text{-Ag}0.1$ nanomaterials," *Sensors and Actuators B: Chemical*, vol. 212, pp. 174–182, 2015.
- [8] Y. Chen, J. Xu, Y. Cui, G. Shang, J. Qian, and J.-E. Yao, "Improvements of dielectric properties of Cu doped $\text{LaTiO}_3+\delta$," *Progress in Natural Science: Materials International*, vol. 26, no. 2, pp. 158–162, 2016.
- [9] L. H. Gao, Z. Ma, and Q. B. Fan, "First-principle studies of the electronic structure and reflectivity of LaTiO_3 and Sr doped LaTiO_3 ($\text{La}_{1-x}\text{Sr}_x\text{TiO}_3$)," *Journal of Electroceramics*, vol. 27, no. 3-4, pp. 114–119, 2011.
- [10] F. Martin and A. Detlef, "Vapor-deposition material for the production of high-refraction optical coating," United States Patent, 5, 340, 607, 1994.
- [11] A. A. Mozhegorov, A. E. Nikiforov, A. V. Larin, A. V. Efremov, L. É. Gonchar', and P. A. Agzamova, "Structure and the electronic and magnetic properties of LaTiO_3 ," *Physics of the Solid State*, vol. 50, no. 9, pp. 1795–1798, 2008.
- [12] P. Combette, L. Nougaret, A. Giani, and F. Pascal-delannoy, "RF magnetron-sputtering deposition of pyroelectric lithium tantalate thin films on ruthenium dioxide," *Journal of Crystal Growth*, vol. 304, no. 1, pp. 90–96, 2007.
- [13] J. Su, J. Xu, C. Yang, and Y. Cheng, "Influence of deposition temperature on optical and laser-induced damage properties of LaTiO_3 films," *Surface Review and Letters*, vol. 22, no. 6, Article ID 1550070, 2015.
- [14] S. Jena, R. B. Tokas, J. S. Misal et al., "Effect of O₂/Ar gas flow ratio on the optical properties and mechanical stress of

- sputtered HfO₂ thin films," *Thin Solid Films*, vol. 592, pp. 135–142, 2015.
- [15] G. Geng, "Deposition conditions and refractive index of TiO₂ films," *Journal of Vacuum Science and Technology*, vol. 29, no. 3, pp. 273–276, 2009.
- [16] W. S. Lin, C. H. Huang, W. J. Yang, C. Y. Hsu, and K. H. Hou, "Photocatalytic TiO₂ films deposited by rf magnetron sputtering at different oxygen partial pressure," *Current Applied Physics*, vol. 10, no. 6, pp. 1461–1466, 2010.
- [17] A. Chaoumead, Y.-M. Sung, and D.-J. Kwak, "The effects of RF sputtering power and gas pressure on structural and electrical properties of ITiO thin film," *Advances in Condensed Matter Physics*, vol. 2012, Article ID 651587, 7 pages, 2012.
- [18] F. Werfel and O. Brümmer, "Corundum structure oxides studied by XPS," *Physica Scripta*, vol. 28, p. 92, 1983.
- [19] Y. Uwamino, T. Ishizuka, and H. Yamatera, "X-ray photoelectron spectroscopy of rare-earth compounds," *Journal of Electron Spectroscopy and Related Phenomena*, vol. 34, no. 1, pp. 67–78, 1984.
- [20] Z. Yin, Z. Akkerman, B. X. Yang, and F. W. Smith, "Optical properties and microstructure of CVD diamond films," *Diamond and Related Materials*, vol. 6, no. 1, pp. 153–158, 1997.

Research Article

Research on a Micro-Nano Si/SiGe/Si Double Heterojunction Electro-Optic Modulation Structure

Song Feng^{1,2}, Lian-bi Li¹, and Bin Xue¹

¹School of Science, Xian Polytechnic University, Xian 710048, China

²State Key Laboratory of Functional Materials for Informatics, Shanghai Institute of Microsystem and Information Technology, Chinese Academy of Sciences, 865 Changning Road, Shanghai 200050, China

Correspondence should be addressed to Lian-bi Li; xpu_lilianbi@163.com

Received 26 October 2017; Accepted 20 March 2018; Published 2 May 2018

Academic Editor: Zaiquan Xu

Copyright © 2018 Song Feng et al. This is an open access article distributed under the Creative Commons Attribution License, which permits unrestricted use, distribution, and reproduction in any medium, provided the original work is properly cited.

The electro-optic modulator is a very important device in silicon photonics, which is responsible for the conversion of optical signals and electrical signals. For the electro-optic modulator, the carrier density of waveguide region is one of the key parameters. The traditional method of increasing carrier density is to increase the external modulation voltage, but this way will increase the modulation loss and also is not conducive to photonics integration. This paper presents a micro-nano Si/SiGe/Si double heterojunction electro-optic modulation structure. Based on the band theory of single heterojunction, the barrier heights are quantitatively calculated, and the carrier concentrations of heterojunction barrier are analyzed. The band and carrier injection characteristics of the double heterostructure structure are simulated, respectively, and the correctness of the theoretical analysis is demonstrated. The micro-nano Si/SiGe/Si double heterojunction electro-optic modulation is designed and tested, and comparison of testing results between the micro-nano Si/SiGe/Si double heterojunction micro-ring electro-optic modulation and the micro-nano Silicon-On-Insulator (SOI) micro-ring electro-optic modulation, Free Spectrum Range, 3 dB Bandwidth, Q value, extinction ratio, and other parameters of the micro-nano Si/SiGe/Si double heterojunction micro-ring electro-optic modulation are better than others, and the modulation voltage and the modulation loss are lower.

1. Introduction

With the rapid development of optoelectronic technology, optoelectronic devices have entered the nano era [1, 2], and many nanotechnology has been used in silicon photonics [3–5]. The reduced size of the device can improve the utilization rate of the chip area, but also the higher performance of the device is required, and the silicon epitaxial material is selected to make optoelectronic devices with higher performance. For example, the epitaxial InP material on silicon substrate is used to fabricate laser [6], the epitaxial Ge material is used to make detector [7], the epitaxial SiGe material is used to fabricate modulator [8], and so forth. In optoelectronic integration, the electro-optic modulator is a very important device, which is responsible for the conversion of optical signals and electrical signals [9, 10]. For the electro-optic modulator, the carrier density of waveguide region is one of the key parameters. When the injected carrier density of

waveguide region is greater, the change of refractive index is greater, and also the modulator is more easily modulated [11, 12]. The traditional method of increasing carrier density is to increase the external modulation voltage, but this way will increase the modulation loss and also is not conducive to photonics integration [8, 13]. So SiGe technology is one way to solve this problem in silicon photonics. Photonics Electronics Technology Research Association (PETRA) and University of Tokyo have made a high-speed and highly efficient Si optical modulator with strained SiGe layer and demonstrated highly efficient modulations of 0.67 and 0.81 V·cm for $V\pi L$ at dc reverse bias voltages of -0.5 and -2 V_{dc}, respectively, and also demonstrated a high-speed operation of 25 Gbps for the Si-MOD at a wavelength of around 1.3 μ m [14]. University of Toronto has made SiGe BiCMOS linear modulator drivers, and the measured differential gain and bandwidth are over 20 dB and 70 GHz, respectively, and P_{1dB} is -2.5 dBm [15]. Ghent University demonstrated single-wavelength, serial

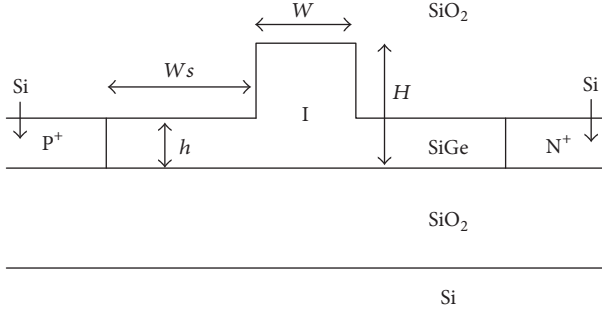


FIGURE 1: Si/SiGe/Si-OI structure.

and real-time 100 GB/s NRZ-OOK transmission over 500 m SSMF with a GeSi EAM implemented on a silicon photonics platform. The device was driven with 2 Vpp without 50 Ω termination, allowing a low-complexity solution for 400 GbE short-reach optical interconnects [16].

This paper presents a micro-nano Si/SiGe/Si double heterojunction electro-optic modulation structure, which can greatly improve the carrier injection concentration and decrease modulation voltage and loss. It is an ideal electro-optic modulator, which is conducive to the photonics integrated circuit miniaturization and integration and also provides a new way for the research of micro-nano optoelectronic devices based on silicon.

2. Structure and Energy Band

Based on the SOI PIN electro-optic modulation structure, a micro-nano Si/SiGe/Si double heterojunction electro-optic modulation structure is presented, which is abbreviated as Silicon/Silicon Germanium/Silicon-On-Insulator (Si/SiGe/Si-OI) structure, as shown in Figure 1. The bottom of the structure is On-Insulator (OI) material, the P+ and N+ regions in the top layer are silicon materials, and the I region is SiGe material in Figure 1. P+ region is doped by B element, and the doping concentration is $1 \times 10^{19} \text{ cm}^{-3}$. N+ region is doped by P element, and the doping concentration is also $1 \times 10^{19} \text{ cm}^{-3}$. I region is N type intrinsic SiGe, and the doping concentration is $1 \times 10^{15} \text{ cm}^{-3}$. In Figure 1, structure parameters are $H = 220 \text{ nm}$, $h = 50 \text{ nm}$, $W = 400 \sim 600 \text{ nm}$, and the width between active region and waveguide (Ws) is a variable value.

In order to facilitate comparison and analysis, two kinds of PIN modulation structures with Si and SiGe materials are established. One is the PIN modulation structure with Si based on the SOI PIN structure, which is abbreviated as SOI structure, as shown in Figure 2(a). The other is the PIN modulation structure with SiGe based on the Silicon Germanium-On-Insulator (SiGe-OI) PIN structure, which is abbreviated as SiGe-OI structure, as shown in Figure 2(b). The doping concentration and structure parameters of two structures are the same as Si/SiGe/Si double heterojunction electro-optic modulation structure.

Si/SiGe/Si-OI structure is composed of P type Si with the high doping concentration, N type SiGe with the low doping

concentration, and N type Si with the high doping concentration. Capital P and N represent Wide Band Gap Semiconductor, and lowercase n represents Narrow Band Gap Semiconductor. So the PIN structure can be equivalent as a Pn heterojunction and a nN heterojunction structure, and the band diagram is shown in Figure 3 under the equilibrium state.

When the PIN structure is working, the main carriers of n region are composed of electron from the P region and hole from the N region, and the barrier height is a key parameter who can influence injection efficiency of electron and hole. After heterojunction band of Si/SiGe/Si-OI structure is analyzed, the hole barrier height of Pn heterojunction of the Si/SiGe/Si-OI structure is represented by the following formula [17]:

$$-qV_D = -k_0 T \ln \frac{n_{i(Si)} n_{i(SiGe)}}{N_D N_A} - \frac{0.73x}{2}, \quad (1)$$

where qV_D is the barrier height, k_0 is the Boltzmann constant, T is the absolute temperature, $n_{i(Si)}$ is the intrinsic carrier concentration of silicon, $n_{i(SiGe)}$ is the intrinsic carrier concentration of Silicon Germanium, N_D is the doping concentration of n region, N_A is the doping concentration of P region, x is the Ge content. Formula (1) indicates that the hole barrier height of Pn heterojunction is related to the doping concentration of P region and n region, the band gap of materials, the temperature, and the Ge content. When the temperature is constant, the lower the doping concentration of P region and n region, the lower the hole barrier height. The narrower the band gap, the higher the intrinsic carrier concentration, and the lower the hole barrier height. The bigger the Ge content, the lower the hole barrier height.

Assuming that $N_A = 10^{19} \text{ cm}^{-3}$, $N_D = 10^{15} \text{ cm}^{-3}$, and the Ge content is 0.2, so the hole barrier height of Pn heterojunction can be calculated equal to $-qV_D = 0.7 \text{ eV}$ at room temperature. For SOI structure and SiGe-OI structure, the Pn junction is homojunction, and the hole barrier height can be analyzed according to the following formula [17]:

$$-qV_{D1,2} = E_{FP} - E_{Fn} = -kT \ln \frac{n_i^2}{N_D N_A}, \quad (2)$$

where E_{FP} is the Fermi level of the P region and E_{Fn} is the Fermi level of the n region. The hole barrier height of Pn homojunctions of the SOI structure can be calculated equal to $-qV_{D1} = 0.82 \text{ eV}$, and the hole barrier height of Pn homojunctions of the SiGe-OI structure can be calculated equal to $-qV_{D2} = 0.733 \text{ eV}$. In the same conditions, the hole barrier height of the Si/SiGe/Si-OI structure is lowest, and the hole barrier height of the SOI structure is highest. This result can be verified by Silvaco CAD software, as shown in Figure 4 [17].

The electron barrier height of nN heterojunction of the Si/SiGe/Si-OI structure can be represented by the following formula [17]:

$$qV'_D = kT \ln \frac{N'_D n_{i(SiGe)}}{N_D n_{i(Si)}} - \frac{0.73x}{2}, \quad (3)$$

where N'_D is the carrier concentration of N region and N_D is the carrier concentration of n region. Formula (3) indicates

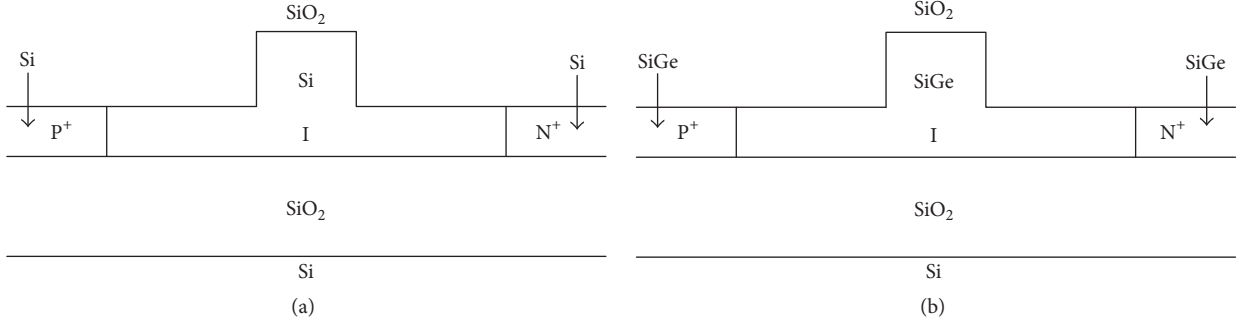


FIGURE 2: Two type modulation structures: (a) SOI structure and (b) SiGe-OI structure.

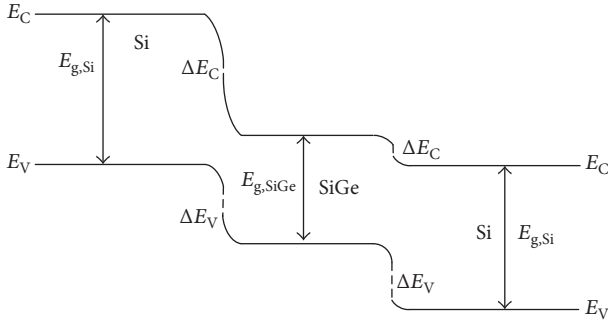


FIGURE 3: The band diagram of Si/SiGe/Si-OI structure under the equilibrium state.

that the electron barrier height of the nN heterojunction of Si/SiGe/Si-OI structure is also related to the doping concentration of N region and n region, the band gap of materials, the temperature, and the Ge content. When the temperature is constant, the lower the doping concentration of N region, the lower the hole barrier height. The higher the doping concentration of n region, the lower the hole barrier height. The wider band gap of n region, the lower the intrinsic carrier concentration, and the lower the hole barrier height. The narrower the band gap of N region, the higher the intrinsic carrier concentration, and the lower the hole barrier height. The smaller the Ge content, the lower the hole barrier height.

Assuming that $N'_D = 10^{19} \text{ cm}^{-3}$, $N_D = 10^{15} \text{ cm}^{-3}$, and the Ge content is 0.2, so the electron barrier height of nN heterojunction can be calculated equal to $qV'_D = 0.2 \text{ eV}$ at room temperature. For SOI structure and SiGe-OI structure, the nN junction is homojunction, and the electron barrier height can be analyzed according to the following formula [17]:

$$qV'_{D1,2} = E_{FN} - E_{Fn} = kT \ln \frac{N'_D}{N_D} \quad (4)$$

The electron barrier height of nN homojunctions of the SOI structure can be calculated equal to $qV'_{D1} = 0.24 \text{ eV}$, and the electron barrier height of nN homojunctions of the SiGe-OI structure can be calculated equal to $qV'_{D2} = 0.24 \text{ eV}$. In the same conditions, the electron barrier height of the Si/SiGe/Si-OI structure is lowest, and the electron barrier height of the

SOI structure is highest. This result can be verified by Silvaco CAD software, as shown in Figure 4.

When the forward bias voltage is set between P region and N region, the original balance between carrier diffusion motion and drift motion is broken, and the PIN device is under nonequilibrium state. Because the doping concentration of the I region is very small, the resistance is very large. The doping concentration of the P region and the N region is very large, and the resistance is very small, so the external positive bias voltage is basically born in the I region. The forward bias voltage produces an electric field opposite to the Built-in Electric Field in the I region, which weakens the intensity of the electric field in the I region and reduces the space charge, so the barrier height decreases. Because the hole barrier height of Pn heterojunction and the electron barrier height of nN heterojunction of Si/SiGe/Si-OI structure all are lower than the barrier height of SiGe-OI structure and SOI structure, so the band of Si/SiGe/Si-OI structure is flattened first under the forward bias voltage. In other words, the Si/SiGe/Si-OI structure has the higher carrier injection at the same forward bias voltage. At 1 V forward voltage, the band simulations of three type modulation structures are shown in Figure 5 [17].

3. Result Analysis

In order to verify that the Si/SiGe/Si-OI structure has better characteristics, the carrier concentration of the SOI structure, the SiGe-OI structure, and the Si/SiGe/Si-OI structure are shown in Figure 6. Figure 6(a) shows the relationship between the electron concentration and modulation voltage for three structures, and Figure 6(b) shows the relationship between the hole concentration and modulation voltage. It can be seen from Figure 6 that, with the increase of modulation voltage, the carrier concentration of three kinds of modulation structure all are gradually increased. When the modulation voltage exceeds 0.6 V, the carrier concentration of the Si/SiGe/Si-OI structure is significantly greater than the carrier concentration of the SOI structure; when the modulation voltage is greater than 0.75 V, the carrier concentration of the Si/SiGe/Si-OI structure is significantly greater than the carrier concentration of SiGe-OI structure; when the modulation voltage is up to 0.9 V, the carrier concentration of the Si/SiGe/Si-OI structure is $6 \times 10^{18} \text{ cm}^{-3}$, but the SOI structure

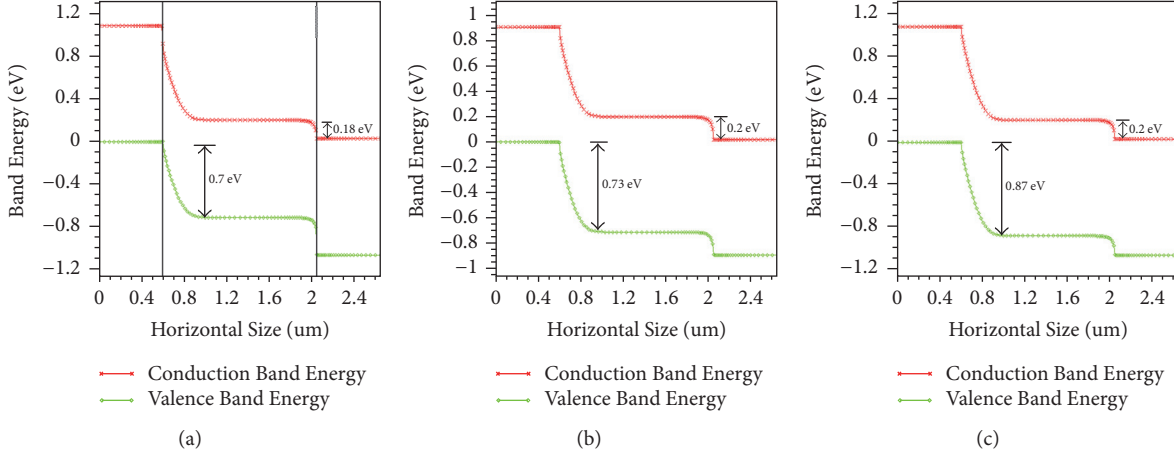


FIGURE 4: The band simulation of three type modulation structures: (a) Si/SiGe/Si-OI structure, (b) SiGe-OI structure, and (c) SOI structure.

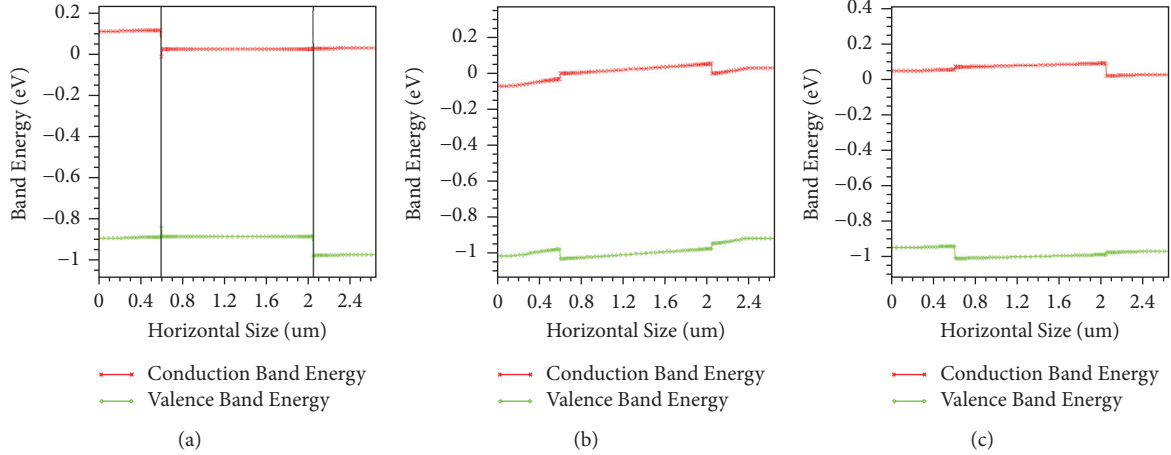


FIGURE 5: At 1 V forward voltage, the band simulation of three type modulation structures: (a) Si/SiGe/Si-OI structure, (b) SiGe-OI structure, and (c) SOI structure.

and the SiGe-OI structure reach the same carrier concentration at 2 V modulation voltage; when the modulation voltage reaches 2 V, the carrier concentration of the Si/SiGe/Si-OI structure could increase to $1.5 \times 10^{19} \text{ cm}^{-3}$. Assuming the SOI structure and the SiGe-OI structure all work at 2 V modulation voltage, so the Si/SiGe/Si-OI structure can work only at 0.9 V modulation voltage. From that we can see the modulation voltage of electro-optic modulator effectively is reduced, and the injection efficiency of electro-optic modulator effectively is improved for the Si/SiGe/Si-OI structure.

In order to verify the correctness of the theoretical analysis and simulation results, we have made the micro-nano Si/SiGe/Si double heterojunction electro-optic modulation, as shown in Figure 7. For the modulation of the optical part, the micro-ring modulation structure is selected. Figure 7(a) shows schematic diagram of the micro-nano Si/SiGe/Si double heterojunction micro-ring electro-optic modulation, Figure 7(b) shows Laser Scanning Confocal Microscopy (LSCM) picture of device by LEXT-OLS4000, Figure 7(c) shows Scanning Electron Microscope (SEM) picture of

micro-ring structure by JSM-6700F, and Figure 7(d) shows SEM of device. The waveguide width is 450 nm, the ridge waveguide height is 220 nm, the planar waveguide height is 50 nm, the gap between waveguide and micro-ring is 200 nm, the micro-ring radius is 10 μm , the doping concentration of P+ region is $1 \times 10^{19} \text{ cm}^{-3}$, the doping concentration of N+ region is $1 \times 10^{19} \text{ cm}^{-3}$, and the doping concentration of I region is $1 \times 10^{15} \text{ cm}^{-3}$. At the same processing conditions and device parameters, the micro-nano SOI micro-ring electro-optic modulation is also made for testing comparison.

The transmission spectrum of the micro-nano Si/SiGe/Si double heterojunction micro-ring electro-optic modulation has been tested, as shown in Figure 8. From that we can see the Free Spectrum Range (FSR) is 9.44 nm, and the 3 dB Bandwidth of the resonant peak is 0.12 nm, near the 1549 nm. The corresponding Q value is 12900, and the extinction ratio of the resonant peak is 11.2 dB.

At the same testing conditions, the transmission spectrum of the micro-nano SOI micro-ring electro-optic modulation has also been tested, as shown in Figure 9. From that

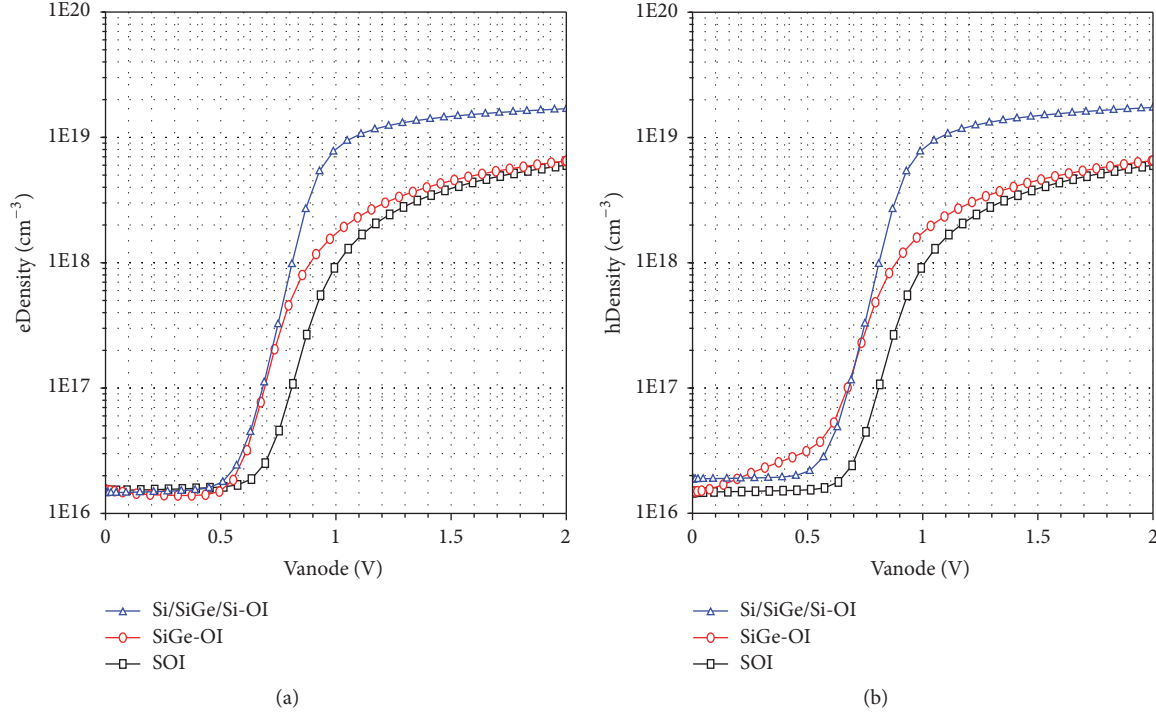


FIGURE 6: The relationship between the carriers concentration and modulation voltage: (a) electron concentration and (b) hole concentration for three structures.

we can see the Free Spectrum Range (FSR) is 9.41 nm, and the 3 dB Bandwidth of the resonant peak is 0.13 nm, near the 1548 nm. The corresponding Q value is 11900, and the extinction ratio of the resonant peak is 7.0 dB.

From the comparison of testing results between the micro-nano Si/SiGe/Si double heterojunction micro-ring electro-optic modulation and the micro-nano SOI micro-ring electro-optic modulation, we can see that Free Spectrum Range, 3 dB Bandwidth, Q value, extinction ratio, and other parameters of the micro-nano Si/SiGe/Si double heterojunction micro-ring electro-optic modulation are better than that of the micro-nano SOI micro-ring electro-optic modulation, and Q value and the extinction ratio are especially greater than that of the micro-nano SOI micro-ring electro-optic modulation.

The test result of the micro-nano Si/SiGe/Si double heterojunction micro-ring electro-optic modulation is shown in Figure 10. The forward bias voltages are 0, 1, 1.1, 1.2 V, respectively. From that we can see the resonant peak has obviously been blue-shifted after the forward bias voltage is set. When the forward bias voltage is 1 V, the value of blue-shift is 0.71 nm.

When the forward bias voltages are 0, 1.5, 1.8, 2 V, respectively, the transmission spectrum of the micro-nano SOI micro-ring electro-optic modulation has been tested, as shown in Figure 11. From that we can see the resonant peak has also obviously been blue-shifted after the forward bias voltage is set, but the modulation effect is worse than Si/SiGe/Si modulation. Only when the forward bias voltage is up to 2 V, the value of blue-shift is 0.71 nm.

From the comparison of testing results between the micro-nano Si/SiGe/Si double heterojunction micro-ring electro-optic modulation and the micro-nano SOI micro-ring electro-optic modulation, we can see that the modulation efficiency of the micro-nano Si/SiGe/Si double heterojunction micro-ring electro-optic modulation is better than that of the micro-nano SOI micro-ring electro-optic modulation at the same processing conditions and testing conditions. In other words, the modulation voltage of the micro-nano Si/SiGe/Si double heterojunction micro-ring electro-optic modulation is lower than that of the micro-nano SOI micro-ring electro-optic modulation, and the modulation power of the micro-nano Si/SiGe/Si double heterojunction micro-ring electro-optic modulation is lower too. So the testing results are consistent with previous theoretical analysis and simulation results.

4. Conclusions

This paper presents a micro-nano Si/SiGe/Si double heterojunction electro-optic modulation structure. Based on the band theory of single heterojunction, the barrier height of the new structure is quantitatively analyzed, and the formulas of barrier height are gotten using the numerical calculus and derivation. The reason of carrier injection enhancement in the new structure is analyzed. On the simulation platform, the new structure, SiGe-OI structure, and SOI structure are simulated. From the comparison of simulation results, when the modulation voltage is up to 0.9 V, the carrier concentration of the new structure is $6 \times 10^{18} \text{ cm}^{-3}$, but the SOI structure and

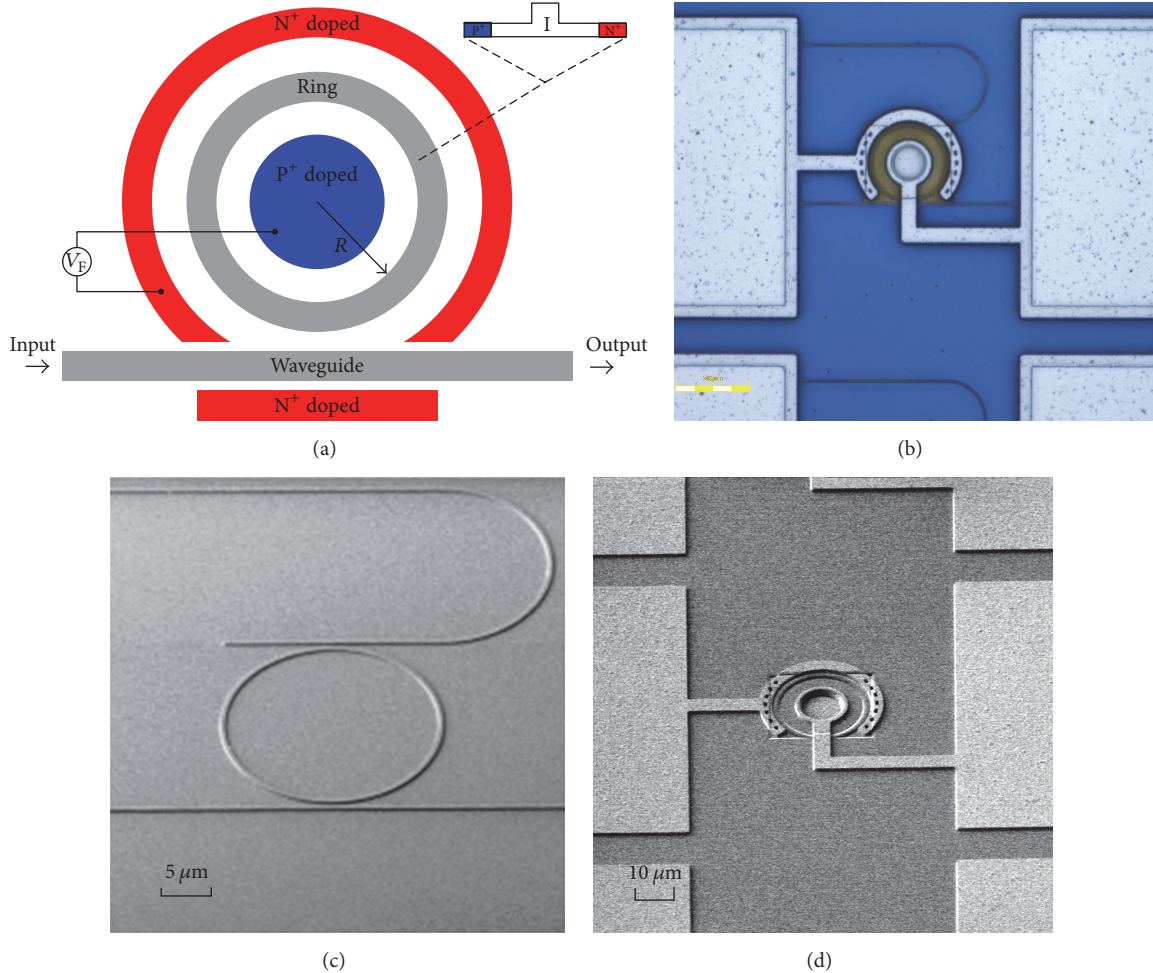


FIGURE 7: (a) Schematic diagram of device, (b) LSCM of device, (c) SEM of micro-ring structure, and (d) SEM of device.

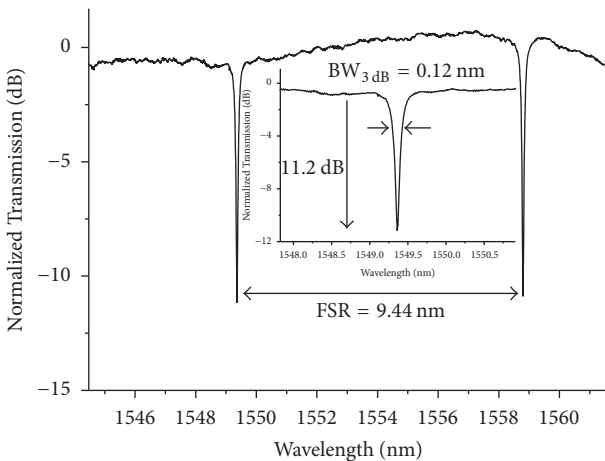


FIGURE 8: The transmission spectrum of the micro-nano Si/SiGe/Si double heterojunction micro-ring electro-optic modulation.

the SiGe-OI structure reach the same carrier concentration at 2 V modulation voltage. Finally, the micro-nano Si/SiGe/Si double heterojunction electro-optic modulation is made and

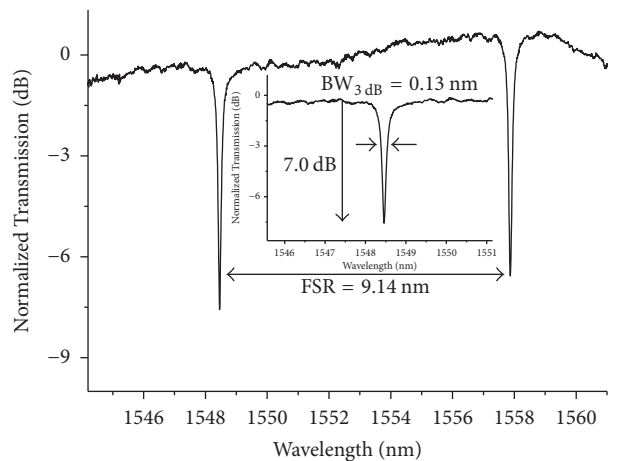


FIGURE 9: The transmission spectrum of the micro-nano SOI micro-ring electro-optic modulation.

tested. Comparison of testing results between the micro-nano Si/SiGe/Si double heterojunction micro-ring electro-optic

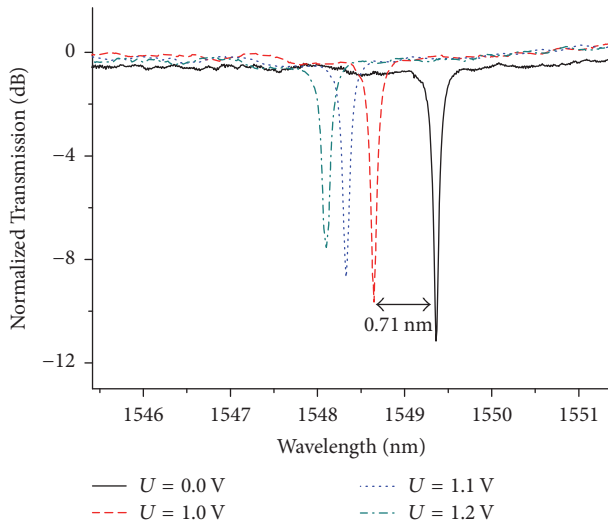


FIGURE 10: The static modulation of the micro-nano Si/SiGe/Si double heterojunction micro-ring electro-optic modulation.

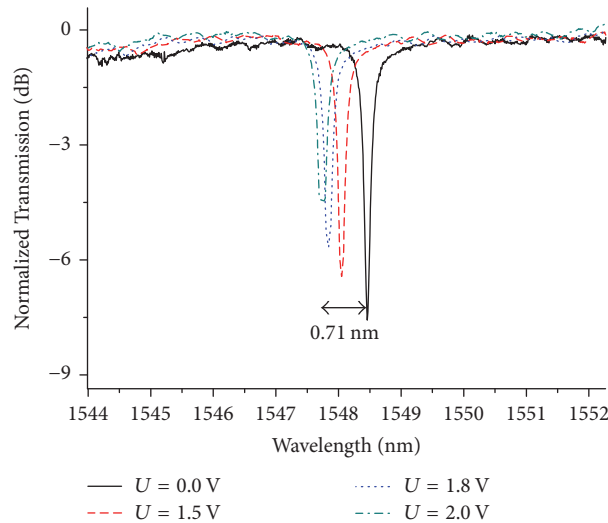


FIGURE 11: The static modulation of the micro-nano SOI micro-ring electro-optic modulation.

modulation and the micro-nano SOI micro-ring electro-optic modulation, Free Spectrum Range, 3 dB Bandwidth, Q value, extinction ratio, and other parameters of the micro-nano Si/SiGe/Si double heterojunction micro-ring electro-optic modulation are better than others, and the modulation voltage and the modulation power are lower. So, the micro-nano Si/SiGe/Si double heterojunction electro-optic modulation structure is an ideal device structure to replace the traditional SOI and SiGe-OI electro-optic modulators structure.

Conflicts of Interest

The authors declare that they have no conflicts of interest.

Acknowledgments

This work was financially supported by National Natural Science Foundation of China (Grant no. 61204080), Natural Science Foundation of Shaanxi Province of China (Grant no. 2017JM6075), Foundation of Shaanxi Provincial Education Department (Grant no. 17JK0335), State Key Laboratory of Functional Materials for Informatics (Grant no. SKL201804), and Shaanxi Province Ordinary University Key Disciplines Construction Projects of Special Funds (Grant no. (2008)169).

References

- [1] K. Singh and D. Kaur, "Vertically arrays of Si-LaNiO₃/BiFeO₃/Au core-shell nano-capacitors for prominent coupled electro-optic effect," *Journal of Applied Physics*, vol. 121, no. 11, Article ID 114103, 2017.
- [2] K. Nozaki, S. Matsuo, T. Fujii et al., "Photonic-crystal nanophotodetector with ultrasmall capacitance for on-chip light-to-voltage conversion without an amplifier," *Optica*, vol. 3, no. 5, pp. 483–492, 2016.
- [3] Q. Fang, J. Song, X. Luo et al., "Low Loss Fiber-to-Waveguide Converter with a 3-D Functional Taper for Silicon Photonics," *IEEE Photonics Technology Letters*, vol. 28, no. 22, pp. 2533–2536, 2016.
- [4] Z. Zhang, J. Hu, H. Chen et al., "Low-crosstalk silicon photonics arrayed waveguide grating," *Chinese Optics Letters*, vol. 15, no. 4, Article ID 041301, 2017.
- [5] Q. Fang, J. Hu, Z. Zhang et al., "A ring-mirrors-integrated silicon photonics arrayed waveguide grating," in *Proceedings of the 2017 Conference on Lasers and Electro-Optics Pacific Rim (CLEO-PR)*, pp. 1-2, Singapore, July 2017.
- [6] J. Bowers, M. Davenport, and S. Liu, "A 20 GHz colliding pulse mode-locked heterogeneous InP-silicon laser," *Cleo: Science Innovations*, vol. SW4C.5, 2017.
- [7] W. Hua and S.-X. Liu, "Nonlinear resonance phenomenon of one-dimensional Bose - Einstein condensate under periodic modulation," *Chinese Physics B*, vol. 23, no. 2, Article ID 020309, 2014.
- [8] S. Akiyama, M. Imai, T. Baba et al., "Compact PIN-diode-based silicon modulator using side-wall-grating waveguide," *IEEE Journal of Selected Topics in Quantum Electronics*, vol. 19, no. 6, pp. 74–84, 2013.
- [9] H. Zwickel, S. Wolf, C. Kieninger et al., "Silicon-organic hybrid (SOH) modulators for intensity-modulation / direct-detection links with line rates of up to 120 Gbit/s," *Optics Express*, vol. 25, no. 20, pp. 23784–23800, 2017.
- [10] S. Heidmann, G. Ulliac, N. Courjal, and G. Martin, "Characterization and control of the electro-optic phase dispersion in lithium niobate modulators for wide spectral band interferometry applications in the mid-infrared," *Applied Optics*, vol. 56, no. 14, pp. 4153–4157, 2017.
- [11] N. Hoppe, C. Rothe, A. Celik et al., "Single waveguide silicon-organic hybrid modulator," *Advances in Radio Science*, vol. 15, pp. 141–147, 2017.
- [12] M. Lauermann, S. Wolf, P. C. Schindler et al., "40 GBd 16QAM signaling at 160 Gb/s in a silicon-organic hybrid modulator," *Journal of Lightwave Technology*, vol. 33, no. 6, Article ID 7015552, pp. 1210–1216, 2015.

- [13] M. Streshinsky, R. Ding, A. Novack et al., “50 Gb/s silicon traveling wave Mach-Zehnder modulator near 1300 nm,” in *Proceedings of the Optical Fiber Communications Conference and Exhibition*, vol. 14560428:1-3, 2014.
- [14] J. Fujikata, M. Noguchi, Y. Kim et al., “High-speed and highly efficient Si optical modulator with strained SiGe layer,” *Applied Physics Express*, vol. 11, no. 3, p. 032201, 2018.
- [15] R. J. A. Baker, J. Hoffman, P. Schvan, and S. P. Voinigescu, “SiGe BiCMOS linear modulator drivers with 4.8-Vpp differential output swing for 120-GBaud applications,” in *Proceedings of the 2017 IEEE Radio Frequency Integrated Circuits Symposium, RFIC 2017*, pp. 260–263, USA, June 2017.
- [16] J. Verbist, M. Verplaetse, S. A. Srinivasan et al., “Real-Time 100 Gb/s NRZ-OOK transmission with a silicon photonics GeSi electro-Absorption modulator,” in *Proceedings of the 6th IEEE Photonics Society Optical Interconnects Conference, OI 2017*, pp. 29-30, USA, June 2017.
- [17] S. Feng, B. Xue, LB. Li et al., “Analysis of Si/SiGe/Si double heterojunction band about a noval structure of PIN electronic modulation,” *Acta Physica Sinica*, vol. 65, no. 5, article 054201, Article ID 054201, 2016.

Research Article

Fabrication and Characterization of Two-Dimensional Layered MoS₂ Thin Films by Pulsed Laser Deposition

Lei Jiao,¹ Yuehui Wang,¹ Yusong Zhi,¹ Wei Cui,¹ Zhengwei Chen,¹ Xiao Zhang,¹ Wenjing Jie,² and Zhenping Wu¹ 

¹State Key Laboratory of Information Photonics and Optical Communications and School of Science, Beijing University of Posts and Telecommunications, Beijing 100876, China

²College of Chemistry and Materials Science, Sichuan Normal University, Chengdu 610066, China

Correspondence should be addressed to Zhenping Wu; zhenpingwu@bupt.edu.cn

Received 25 December 2017; Revised 25 January 2018; Accepted 7 February 2018; Published 15 April 2018

Academic Editor: Zhixin Hu

Copyright © 2018 Lei Jiao et al. This is an open access article distributed under the Creative Commons Attribution License, which permits unrestricted use, distribution, and reproduction in any medium, provided the original work is properly cited.

Direct growth of uniform wafer-scale two-dimensional (2D) layered materials using a universal method is of vital importance for utilizing 2D layers into practical applications. Here, we report on the structural and transport properties of large-scale few-layer MoS₂ back-gated field effect transistors (FETs), fabricated using conventional pulsed laser deposition (PLD) technique. Raman spectroscopy and transmission electron microscopy results confirmed that the obtained MoS₂ layers on SiO₂/Si substrate are multilayers. The FETs devices exhibit a relative high on/off ratio of 5×10^2 and mobility of $0.124 \text{ cm}^2 \text{ V}^{-1} \text{ s}^{-1}$. Our results suggest that the PLD would be a suitable pathway to grow 2D layers for future industrial device applications.

1. Introduction

Atomically layered two-dimensional (2D) materials are intriguing for both electronic and optoelectronic applications, because of their unique electrical, optical, and mechanical properties [1–4]. Among these 2D layered materials, molybdenum dichalcogenides (MoS₂), where the layered S-Mo-S are bonded by van der Waals interactions with Mo and S atoms which are bonded by strong covalent interactions, have attracted extensive interests due to their considerable band gap and high carrier mobility. Both theoretical estimations and experimental observations indicate an indirect to direct energy bandgap transition when MoS₂ is thinned from bulk to monolayer, while its bandgap increases from $\sim 1.2 \text{ eV}$ to $\sim 1.8 \text{ eV}$ [5–8]. Owing to the extraordinary layer-dependent bandgap behavior, MoS₂ is considered a promising candidate to overcome the shortages belonging to zero-bandgap graphene, providing a possible solution for next-generation electronic applications [9]. For instance, monolayer and few-layer MoS₂ based field effect transistors (FETs) have been reported, possessing high on/off ratios exceeding 10^3 [10–12]. The mobility in monolayer MoS₂ FETs

in vacuum reported so far is $8 \text{ cm}^2 \text{ V}^{-1} \text{ s}^{-1}$ [13–15], which is lower than the theoretical value ($410 \text{ cm}^2 \text{ V}^{-1} \text{ s}^{-1}$) [15]. The mobility in few-layer FETs at room temperature could reach $470 \text{ cm}^2 \text{ V}^{-1} \text{ s}^{-1}$ [16]; the value is close to the theoretical value ($200\text{--}500 \text{ cm}^2 \text{ V}^{-1} \text{ s}^{-1}$) estimated through phonon scattering limit [17]. Even with the desirable requirement for industrial applications, to date, most of works have focused on exploring the methods of large scale, high quality MoS₂ thin films. Conventional methods to obtain MoS₂ layers include mechanical exfoliation, chemical vapor deposition (CVD), and PLD [18–20]. However, it is inconvenient to control the scale size and thickness of samples using mechanical exfoliation method. The layer nucleation in CVD methods is difficult with a rigor experimental condition, resulting nonuniform MoS₂ layers. Up to now, PLD method has successfully been employed for the deposition of large-scale layered materials, including graphene, black phosphorous (BP), MoS₂, and InSe [21–23]. One of the main advantages of using PLD is the convenience to control the layer numbers of the large-scale 2D materials by solely varying the pulses numbers. In this work, we report the structural and transport characterization of few-layer MoS₂ back-gated FETs fabricated via PLD technique.

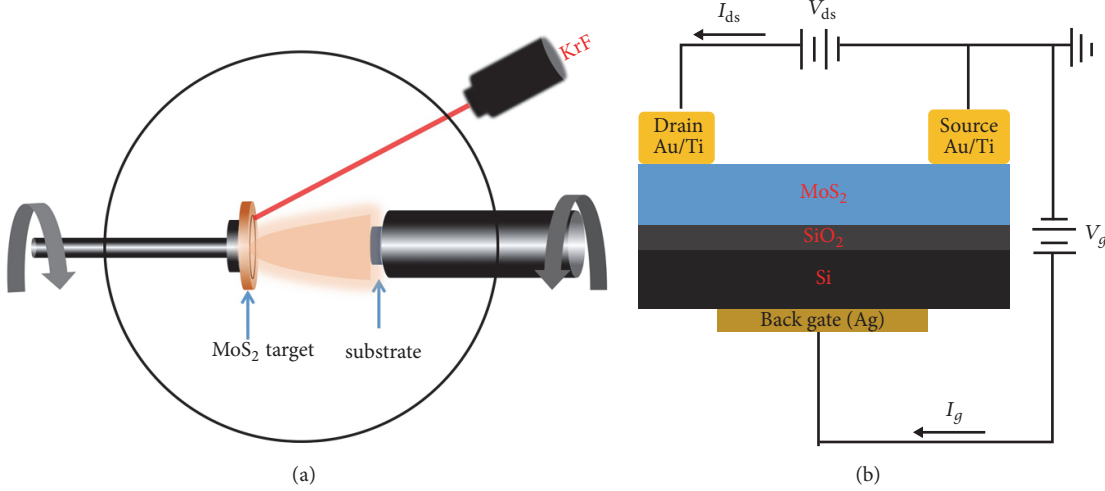


FIGURE 1: Schematic diagram of (a) PLD equipment; (b) MoS₂ back-gated FETs structure.

2. Materials and Methods

Few-layer MoS₂ films with the dimension of 10 mm × 10 mm were fabricated on the surface-cleaned SiO₂ (300 nm)/p⁺-Si wafer by PLD (KrF 248 nm) with a laser energy of 200 mJ/pulses and a frequency of 5 Hz. Figure 1(a) illustrates the experimental setup of the PLD system. A commercial MoS₂ pellet (HeFei Crystal Technical Material Co., Ltd.) was used as the target. The target and substrate distance was set at 5 cm. Before deposition, the chamber was evacuated to a base pressure of $\sim 1 \times 10^{-5}$ Pa to avoid the oxidation of the MoS₂ films. The SiO₂/Si substrates temperature was maintained at 700°C during the growth. Both target and substrate were rotated during the deposition to obtain a uniform film. When the laser pulses strike the MoS₂ target, the formed plasma including atoms and ions will reach substrates. The thickness of MoS₂ films can be controlled by the number of laser pulses. Here the pulse numbers for growth MoS₂ films are set to be 1200 pulses. The atoms valence in MoS₂ was measured by X-ray photoelectron spectroscopy (XPS). Raman spectroscopy and transmission electron microscopy (TEM) were employed to confirm the thickness of MoS₂ films. To construct the FETs structure, radio frequency magnetron sputtering technique was used to deposit Au/Ti electrodes on surface of MoS₂ layers and back of SiO₂/Si substrates. The deposition time of Au/Ti electrodes is 2 min and 20 s, respectively. The schematic diagram of the fabricated FETs device is shown in Figure 1(b). The transport and transfer measurements were conducted in a Keithley 4200 semiconductor characterization system. All the tests were executed at 300 K in atmosphere.

3. Results and Discussion

Raman spectroscopy was a commonly used technique to estimate the thickness of the 2D materials [24]. As shown in Figure 2(a), two prominent characteristic peaks are attributed to the mode of MoS₂ atomic layers vibration (in-plane E_{2g}^1 mode: ~ 382 cm⁻¹ and out-of-plane A_{1g} mode: ~ 407 cm⁻¹).

The distance between E_{2g}^1 and A_{1g} Δf is proportional to thickness of MoS₂ films, the E_{2g}^1 peak exhibits a red shift with a blue shift of the A_{1g} peak when the MoS₂ thickness decreased, and Δf follows an empirical formula: $\Delta f = 26.45 - 15.42/(1 + 1.44n^{0.9})$ cm⁻¹ [25]. According to the formula, the thickness of MoS₂ layers can be deduced: monolayer ~ 18 cm⁻¹, bilayer ~ 22.4 cm⁻¹, trilayer ~ 23 cm⁻¹, and few-layer ~ 25 cm⁻¹. The cross-sectional TEM image (shown in Figure 2(b)) exhibits a sharp and well-defined MoS₂ layers. A 7 nm thick MoS₂ layer was grown on SiO₂/Si wafer with an interlayer spacing ~ 0.68 nm, which is close to the theoretical value of the MoS₂ monolayer thickness (~ 0.65 nm) [26]. These results are consistent with the Raman spectral results, implying that the obtained MoS₂ films ($\Delta f = 25$ cm⁻¹) in this work are few-layer sample.

In order to examine the sulfur deficiency in the MoS₂ films, XPS analysis was carried out. As shown in Figure 3, there are three peaks of Mo 3d, located at 229.18 eV, 232.67 eV, and 235.97 eV. The first two peaks could be assigned to Mo 3d_{5/2} and Mo 3d_{3/2}, respectively. They are correlating to Mo⁴⁺ state in MoS₂. The third core level peak is correlating to Mo⁶⁺ 3d_{3/2} state, and the fitted curves are shown in blue in the image. Due to the existence of Mo⁶⁺, there should be S vacancies in our samples. One possibility is the S missing during the process of the growth of the films. Other possibility is the reaction with oxygen to form MoO₃ after the sample taking out of the chamber. The existence of MoO₃ will exert influence on the optical and electrical characteristics of MoS₂ thin films.

To investigate the electric properties of the MoS₂ film, back-gated FETs were fabricated based on few-layer MoS₂ films grown on SiO₂/Si substrates. As seen from Figure 4(a), the relationship between drain current (I_{ds}) and drain voltage (V_{ds}) at different back-gated voltage (V_g) was investigated, and the step of back-gated voltage is 5 V. A clear n-type semiconducting property was depicted which is consistent with previous reports [27]. The n-type behavior of MoS₂ sample might be due to the impurities or existence of interstitial

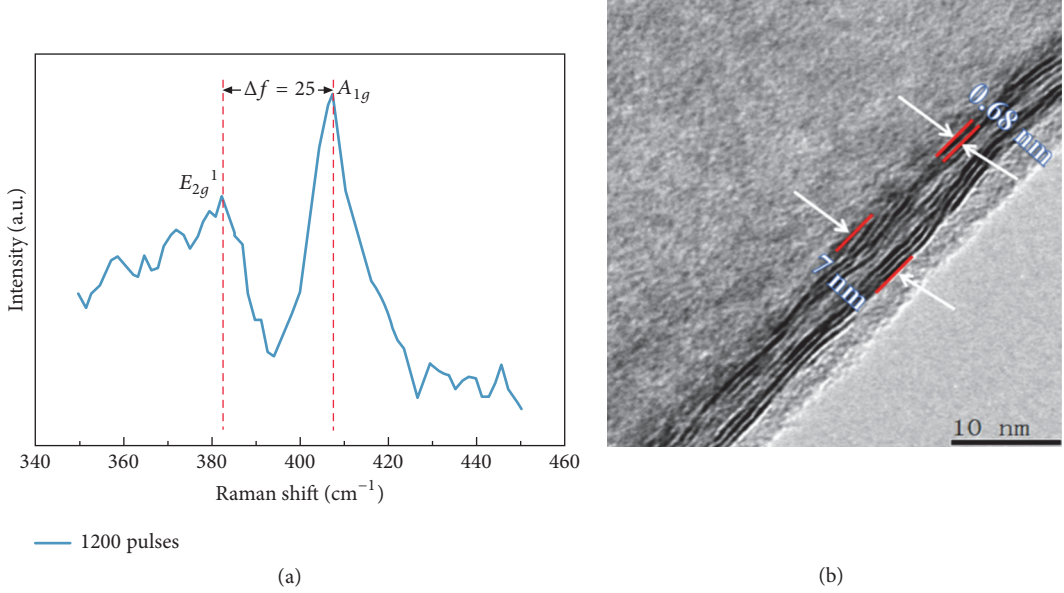


FIGURE 2: (a) Raman image of MoS₂ films. The distance between E_{2g}^1 and A_{1g} is 25 cm⁻¹. (b) Cross-sectional TEM image of few-layer MoS₂ film.

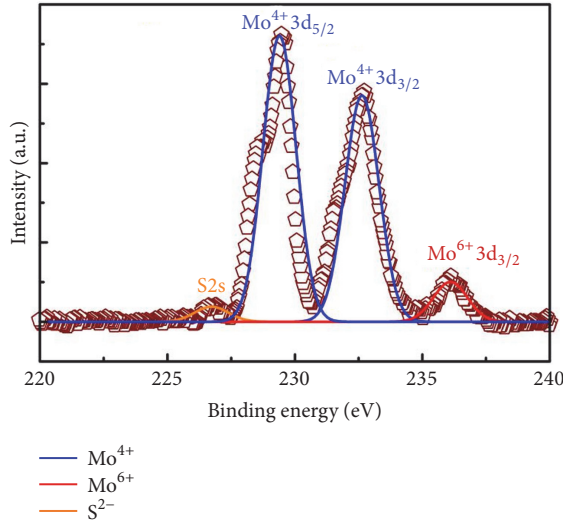


FIGURE 3: The XPS spectra of Mo 3d, S 2s core levels in MoS₂ films.

atoms in the interlayer gap. As shown in Figure 4(b), the off-state leakage current (I_{off}) is ~ 10 nA, while the on-state current (I_{on}) is $\sim 5 \mu\text{A}$; the on/off ratio is about 5×10^2 , and the ratio is compared to the ratio ($\sim 10^3$) of monolayer FETs [10]. The mobility of multilayer MoS₂ FETs can be estimated based on the formula:

$$\mu = \frac{L}{W \times (\epsilon_0 \epsilon_r / d) \times V_{\text{ds}}} \times \frac{dI_{\text{ds}}}{dV_g} \quad (1)$$

and the channel length L is 0.1 mm, the channel width W is 1.5 mm, ϵ_0 is 8.854×10^{-12} F/m, ϵ_r is 3.9 [17], d is the thickness of SiO₂ (300 nm), and V_{ds} in our experiment is 5 V. The value of dI_{ds}/dV_g can be obtained from the linear fit in Figure 4(b).

The mobility of the FETs calculated is $0.124 \text{ cm}^2 \text{V}^{-1} \text{s}^{-1}$, and the value is similar to other multilayer back-gated MoS₂ FETs [28]. A bit low mobility may be due to the impurity phase in the film or the impurities and traps on the surface of SiO₂ films [17]. Moreover, the nonlinear rectifying behavior in $I_{\text{ds}} - V_{\text{ds}}$ curves and the saturation of current in the high positive gate voltage imply a contact resistance between the electrodes and the film, which could also result in an underestimated mobility.

4. Conclusions

In summary, we have reported the PLD grown few-layer MoS₂ based FETs showing good transport characteristics

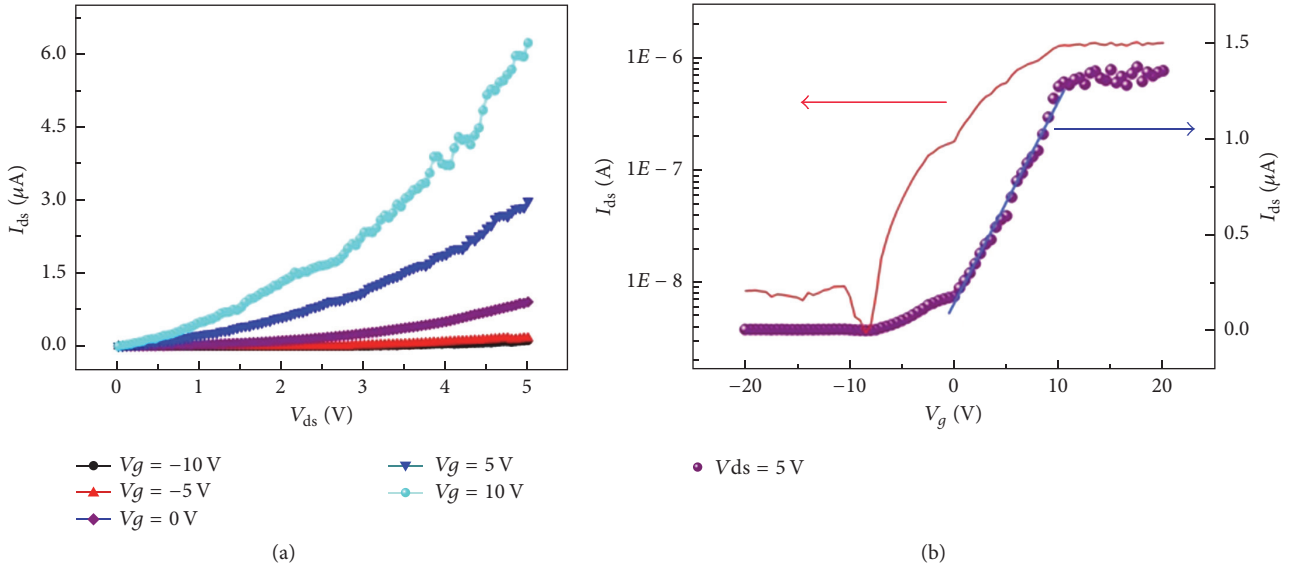


FIGURE 4: FETs characterization of few-layer MoS₂ film. (a) Transport characteristics at different V_g . (b) Transfer curves of MoS₂ thin films in logarithmic and linear scales.

with relatively high ON/OFF ratio ~ 500 , which is comparable to monolayer and few-layer MoS₂ FETs fabricated using CVD-grown samples. Our results suggest that the PLD grown MoS₂ films not only achieve large-scale size, but also present moderate electric properties. The developed PLD method for growth of wafer-scale 2D layered materials may provide a new insight for further electronic applications.

Conflicts of Interest

The authors declare no conflicts of interest.

Acknowledgments

This work was supported by the National Natural Science Foundation of China (nos. 61604100, 11404029, 51572033, and 51172208) and the Fund of State Key Laboratory of Information Photonics and Optical Communications (BUPT).

References

- [1] J. T. Robinson, F. K. Perkins, E. S. Snow, Z. Wei, and P. E. Sheehan, “Reduced graphene oxide molecular sensors,” *Nano Letters*, vol. 8, no. 10, pp. 3137–3140, 2008.
- [2] J. D. Fowler, M. J. Allen, V. C. Tung, Y. Yang, R. B. Kaner, and B. H. Weiller, “Practical chemical sensors from chemically derived graphene,” *ACS Nano*, vol. 3, no. 2, pp. 301–306, 2009.
- [3] A. Zavabeti, J. Z. Ou, B. J. Carey et al., “A liquid metal reaction environment for the room-temperature synthesis of atomically thin metal oxides,” *Science*, vol. 358, no. 6361, pp. 332–335, 2017.
- [4] W. Jie and J. Hao, “Time-dependent transport characteristics of graphene tuned by ferroelectric polarization and interface charge trapping,” *Nanoscale*, vol. 10, no. 1, pp. 328–335, 2018.
- [5] A. J. Grant, T. M. Griffiths, G. D. Pitt, and A. D. Yoffe, “The electrical properties and the magnitude of the indirect gap in the semiconducting transition metal dichalcogenide layer crystals,” *Journal of Physics C: Solid State Physics*, vol. 8, no. 1, article no. 004, pp. L17–L23, 1975.
- [6] K. F. Mak, C. Lee, J. Hone, J. Shan, and T. F. Heinz, “Atomically thin MoS₂: a new direct-gap semiconductor,” *Physical Review Letters*, vol. 105, no. 13, Article ID 136805, 2010.
- [7] Q. H. Wang, K. Kalantar-Zadeh, A. Kis, J. N. Coleman, and M. S. Strano, “Electronics and optoelectronics of two-dimensional transition metal dichalcogenides,” *Nature Nanotechnology*, vol. 7, no. 11, pp. 699–712, 2012.
- [8] Y. Yoon, K. Ganapathi, and S. Salahuddin, “How good can monolayer MoS₂ transistors be?” *Nano Letters*, vol. 11, no. 9, pp. 3768–3773, 2011.
- [9] D. Jariwala, V. K. Sangwan, L. J. Lauhon, T. J. Marks, and M. C. Hersam, “Emerging device applications for semiconducting two-dimensional transition metal dichalcogenides,” *ACS Nano*, vol. 8, no. 2, pp. 1102–1120, 2014.
- [10] X. Tong, E. Ashalley, F. Lin, H. Li, and Z. M. Wang, “Advances in MoS₂-based field effect transistors (FETs),” *Nano-Micro Letters*, vol. 7, no. 3, pp. 203–218, 2015.
- [11] W. Gu, J. Shen, and X. Ma, “Fabrication and electrical properties of MoS₂ nanodisc-based back-gated field effect transistors,” *Nanoscale Research Letters*, vol. 9, article 100, 2014.
- [12] H. Fang, M. Tosun, G. Seol et al., “Degenerate *n*-doping of few-layer transition metal dichalcogenides by potassium,” *Nano Letters*, vol. 13, no. 5, pp. 1991–1995, 2013.
- [13] C.-C. Wu, D. Jariwala, V. K. Sangwan, T. J. Marks, M. C. Hersam, and L. J. Lauhon, “Elucidating the photoresponse of ultrathin MoS₂ field-effect transistors by scanning photocurrent microscopy,” *The Journal of Physical Chemistry Letters*, vol. 4, no. 15, pp. 2508–2513, 2013.
- [14] J. J. McMorrow, C. D. Cress, H. N. Arnold et al., “Vacuum ultraviolet radiation effects on two-dimensional MoS₂ field-effect transistors,” *Applied Physics Letters*, vol. 110, no. 7, Article ID 073102, 2017.
- [15] K. Kaasbjerg, K. S. Thygesen, and K. W. Jacobsen, “Unraveling the acoustic electron-phonon interaction in graphene,” *Physical*

- Review B: Condensed Matter and Materials Physics*, vol. 85, no. 16, article 165440, 2012.
- [16] W. Bao, X. Cai, D. Kim, K. Sridhara, and M. S. Fuhrer, "High mobility ambipolar MoS₂ field-effect transistors: substrate and dielectric effects," *Applied Physics Letters*, vol. 102, no. 4, Article ID 042104, 2013.
 - [17] B. Radisavljevic, A. Radenovic, J. Brivio, V. Giacometti, and A. Kis, "Single-layer MoS₂ transistors," *Nature Nanotechnology*, vol. 6, no. 3, pp. 147–150, 2011.
 - [18] C.-Y. Su, A.-Y. Lu, C.-Y. Wu et al., "Direct formation of wafer scale graphene thin layers on insulating substrates by chemical vapor deposition," *Nano Letters*, vol. 11, no. 9, pp. 3612–3616, 2011.
 - [19] K. S. Novoselov, D. Jiang, F. Schedin et al., "Two-dimensional atomic crystals," *Proceedings of the National Academy of Sciences of the United States of America*, vol. 102, no. 30, pp. 10451–10453, 2005.
 - [20] S. Balendhran, J. Z. Ou, M. Bhaskaran et al., "Atomically thin layers of MoS₂ via a two step thermal evaporation-exfoliation method," *Nanoscale*, vol. 4, no. 2, pp. 461–466, 2012.
 - [21] W. Jie, Z. Yang, F. Zhang, G. Bai, C. W. Leung, and J. Hao, "Observation of room-temperature magnetoresistance in monolayer MoS₂ by ferromagnetic gating," *ACS Nano*, vol. 11, no. 7, pp. 6950–6958, 2017.
 - [22] Z. Yang, W. Jie, C.-H. Mak et al., "Wafer-scale synthesis of high-quality semiconducting two-dimensional layered InSe with broadband photoresponse," *ACS Nano*, vol. 11, no. 4, pp. 4225–4236, 2017.
 - [23] Z. Yang, J. Hao, S. Yuan et al., "Field-effect transistors based on amorphous black phosphorus ultrathin films by pulsed laser deposition," *Advanced Materials*, vol. 27, no. 25, pp. 3748–3754, 2015.
 - [24] H. Li, Q. Zhang, C. C. R. Yap et al., "From bulk to monolayer MoS₂: evolution of raman scattering," *Advanced Functional Materials*, vol. 22, no. 7, pp. 1385–1390, 2012.
 - [25] C. Lee, H. Yan, L. E. Brus, T. F. Heinz, J. Hone, and S. Ryu, "Anomalous lattice vibrations of single-and few-layer MoS₂," *ACS Nano*, vol. 4, no. 5, pp. 2695–2700, 2010.
 - [26] M. M. Benameur, B. Radisavljevic, J. S. Héron, S. Sahoo, H. Berger, and A. Kis, "Visibility of dichalcogenide nanolayers," *Nanotechnology*, vol. 22, no. 12, Article ID 125706, 2011.
 - [27] H. Li, Z. Y. Yin, Q. Y. He et al., "Fabrication of single- and multilayer MoS₂ film-based field-effect transistors for sensing NO at room temperature," *Small*, vol. 8, no. 1, pp. 63–67, 2012.
 - [28] H. Qiu, L. Pan, Z. Yao, J. Li, Y. Shi, and X. Wang, "Electrical characterization of back-gated bi-layer MoS₂ field-effect transistors and the effect of ambient on their performances," *Applied Physics Letters*, vol. 100, no. 12, article 123104, 2012.

Research Article

Quantum Simulations of Charge Separation at a Model Donor-Acceptor Interface: Role of Delocalization and Local Packing

Allen Kelley, Kush Patel, and Eric R. Bittner 

Department of Chemistry, University of Houston, Houston, TX 77204, USA

Correspondence should be addressed to Eric R. Bittner; ebittner@central.uh.edu

Received 28 November 2017; Accepted 20 February 2018; Published 10 April 2018

Academic Editor: Zhixin Hu

Copyright © 2018 Allen Kelley et al. This is an open access article distributed under the Creative Commons Attribution License, which permits unrestricted use, distribution, and reproduction in any medium, provided the original work is properly cited.

Organic Polymer-based photovoltaic systems offer a viable alternative to more standard solid-state devices for light-harvesting applications. In this study, we investigate the electronic dynamics of a model organic photovoltaic (OPV) heterojunction consisting of polyphenylene vinylene (PPV) oligomers and a [6, 6]-phenyl C61-butyric acid methyl ester (PCBM) blend. Our approach treats the classical molecular dynamics of the atoms within an Ehrenfest mean-field treatment of the $\pi-\pi^*$ singly excited states spanning a subset of donor and acceptor molecules near the phase boundary of the blend. Our results indicate that interfacial electronic states are modulated by C=C bond stretching motions and that such motions induce avoided crossings between nearby excited states thereby facilitating transitions from localized excitonic configurations to delocalized charge-separated configurations on an ultrafast time-scale. The lowest few excited states of the model interface rapidly mix allowing low frequency C-C out-of-plane torsions to modulate the potential energy surface such that the system can sample both intermolecular charge-transfer and charge-separated electronic configurations on sub-100 fs time scales. Our simulations support an emerging picture of carrier generation in OPV systems in which interfacial electronic states can rapidly decay into charge-separated and current producing states via coupling to vibronic degrees of freedom.

1. Introduction

Advances in both materials and device fabrication have led to the development of highly efficient organic polymer-based photovoltaic cell (OPV) in which the power conversion efficiency is in excess of 10–11% under standard solar illumination and efficiencies as high as 12% in multijunction OPVs [1]. This increase in power conversion efficiency indicates that mobile charge carriers can be efficiently generated and collected in well-optimized devices; however, the underlying photo-physical mechanism for converting highly bound molecular (Frenkel) excitons into mobile and asymptotically free photo-carriers remains elusive in spite of vigorous, multidisciplinary research activity [2–18].

It is generally recognized that the local microstructure of the interface between the donor and acceptor materials composing a bulk heterojunction cell plays a central role in determining the overall efficiency of an OPV device.

Generally speaking, charge separation in OPV materials occurs when excitons near the donor/acceptor (DA) interface dissociate into either charge-transfer or charge-separated states.



These two states are distinguished by whether or not the positively charged (hole) on an electron donor molecule is directly adjacent to the acceptor anion, termed a charge-transfer state (CT), or if the two charges are separated by one or more molecular units, termed a charge-separated state (CS). In the former (CT) case, the two charges are pinned to the D:A interface by Coulombic forces which are only weakly screened by the low dielectric nature of conjugated organic systems. Curiously, recent ultrafast spectroscopic measurements on optimized polymer:fullerene-based OPV systems indicate that charge carriers begin to appear $\leq 100\text{-fs}$ following photoexcitation [2, 12, 15, 19–22]. Moreover

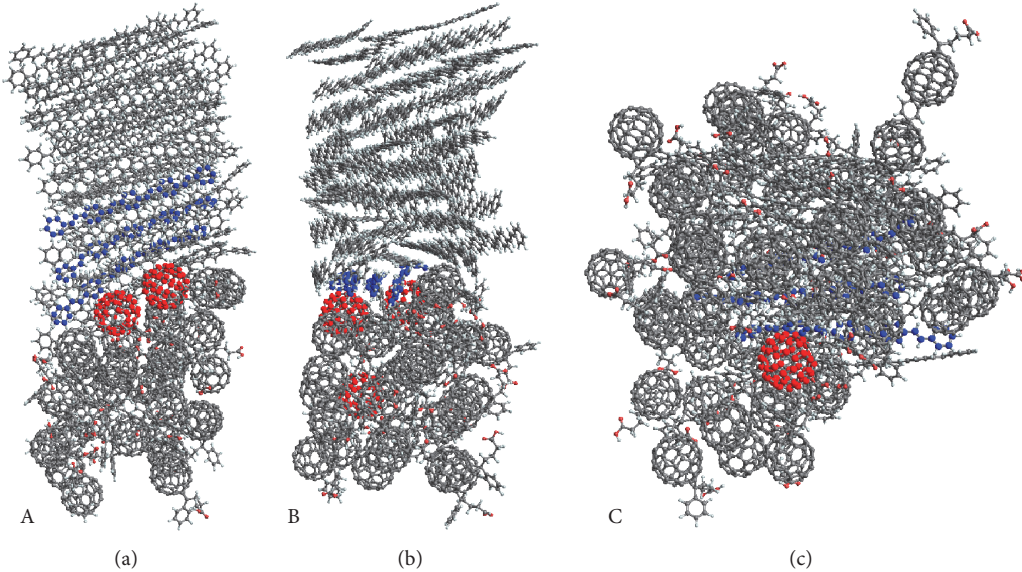


FIGURE 1: Snapshot of the three MD simulation cells: A, B, and C. The red and blue highlighted molecules denote the π -active units in our system.

experiments by Gélinas et al., in which Stark-effect signatures in transient absorption spectra were analysed to probe the local electric field as charge separation proceeds, indicate that electrons and holes separate by as much as 40 Å over the first 100 fs and evolve further on a picosecond time scales to produce unbound and freely mobile charge pairs [4].

It is generally recognized the electronic states at DA interfaces are delocalized over multiple molecular units and may well extend deeply into the bulk. As a result, the spatial extent of these states presents a profound challenge to even state-of-the-art ab initio quantum chemical methods. Moreover, one can not ignore the role of structural fluctuations and intermolecular vibrations in modulating the electronic energies. Recently, Bittner and Silva proposed that energy level fluctuations due to thermal motions can lead to strong quantum mechanical coupling between excitonic and charge-separated states [23]. Central to this theory is the fact that the golden-rule transition rates between states can be determined by examining energy gap fluctuations. This model unifies a number of seeming disparate observations but lacks a desired atomistic basis.

Here we employ a hybrid molecular mechanics/quantum mechanics (MM/QM) approach to sample the electronic excited states of a model bulk heterojunction system. Our approach provides an explicit, semiempirical description of the excited π -electronic states of select molecular units near the interface between phase segregated donor and acceptor molecular units. Our simulations indicate that interfacial electronic states are modulated by C=C bond stretching motions and that such motions induce avoided crossings between nearby excited states thereby facilitating transitions from localized excitonic configurations to delocalized charge-separated configurations on an ultrafast time-scale.

2. Results

Our results build upon a model of charge separation in donor:acceptor blends that we recently reported upon [24]. In this study, we considered a model blend of poly(p-phenylene vinylene) (PPV) donor oligomers and phenyl-C₆₁-butyric acid methyl ester (PCBM) and defined the “ π -active” region by selecting (by hand) a single PCBM and three nearby PPV chains to assess the penetration of a localized electronic state into the bulk region. In this paper we model a phase separated interface between PCBM and PPV oligomers. While the semiempirical treatment does facilitate including up to a few hundred π electrons, we do need to be judicious in choosing the “ π -active” region.

Figure 1 shows representative molecular configurations of the three cases studied in this paper. Each corresponds to a periodic simulation cell in the xy plane following equilibration at 100 K and 1 atm pressure and they are representative of typical interfacial configurations. In each figure, the red and blue colored spheres represent atoms included in the quantum chemical description. In Case A, we selected 2 interfacial PCBM and 3 nearby π -active PPV oligomers that penetrate into the bulk polymer region, including a total of 230 C atoms. In Case B, we selected 3 PCBM and 3 nearby PPV oligomers expanding the π -active molecules that form the interfacial heterojunction, including a total of 288 C atoms. Cases A and B differ solely in the initial selection of the PPV oligomers included in the quantum mechanical subspace. For comparison, in Case C we selected 1 PCBM and 3 PPV oligomers that penetrate into the bulk. In all cases, we employ periodic boundary conditions in xyz as in our previous study [24]. This simulation was set up to be very similar to case A, only adding a single PCBM molecule to the interfacial region.

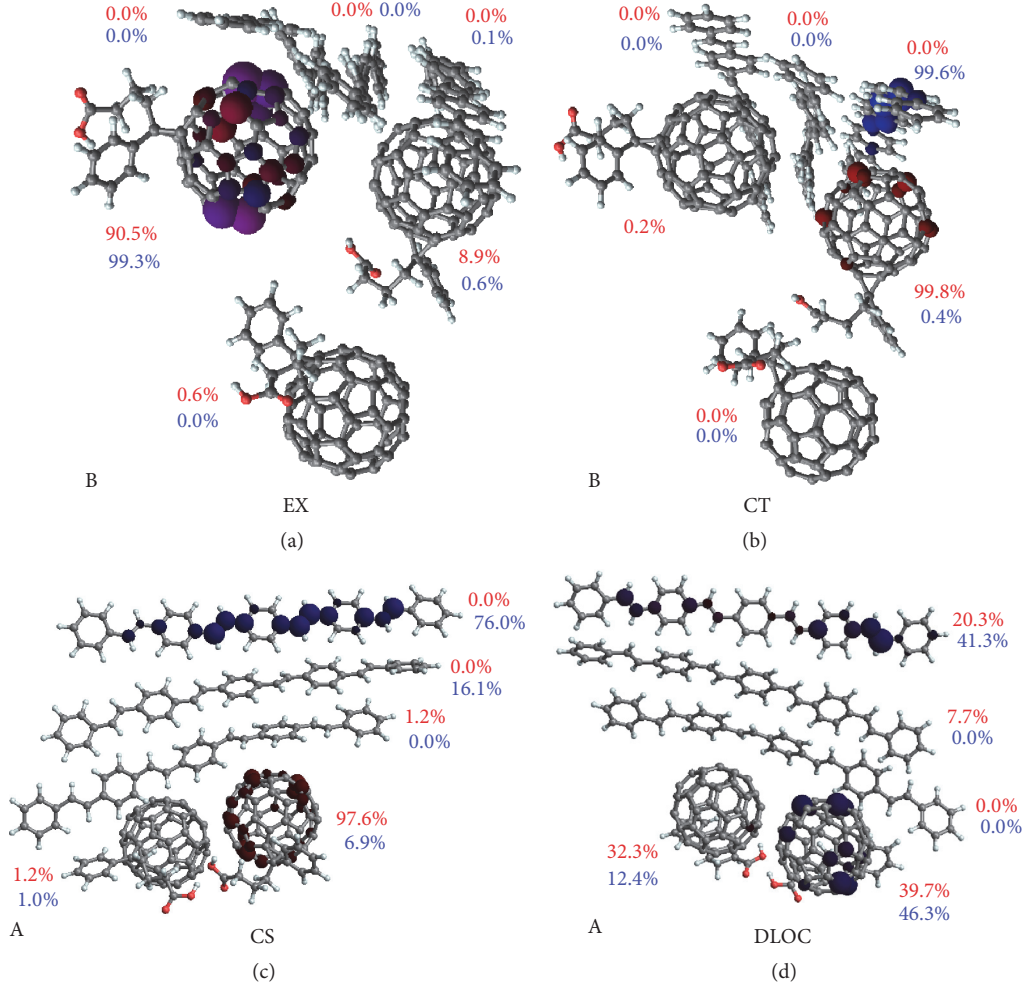


FIGURE 2: The dominant adiabatic states from simulations A (c, d) and B (a, b) as shown in Figure 1. The red and blue numbers denote the electron/hole density as a percent on the indicated molecule. The states correspond to the x -axis in Figure 3. The four snapshots shown represent typical states for our systems. (a, b) from left to right present an exciton located on the PCBM molecule and a charge-transfer state. (c, d) from left to right show a charge-separated state and a partly delocalized state.

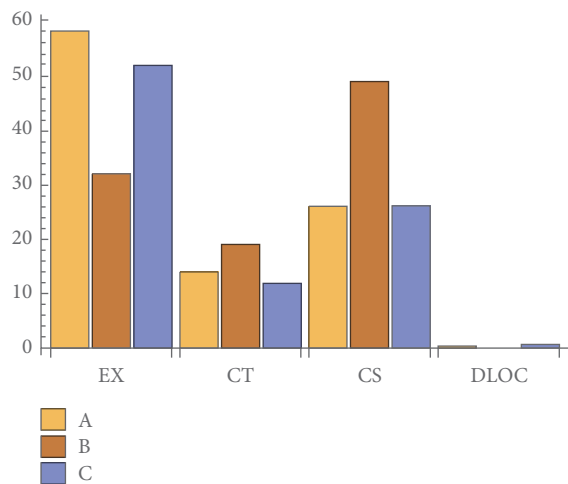


FIGURE 3: Histogram plot of the populations of adiabatic states in systems A, B, and C taken every fs. Each cluster represents a different classification of the adiabatic states as shown in Figure 2.

These three cases are certainly not an exhaustive study of all possible ways that an excitation can localize at an interface and in general one should include all the C atoms as being part of the π system as to include the possibility for both localized and delocalized excitations. However, such study is not computationally feasible and we select these to test the extent that low-lying excitations can penetrate into the bulk region, how this penetration may facilitate charge separation, and the extent that this plays into the mixing between charge-transfer, excitonic, and charge-separated configurations.

Over the course of eight 10 ps simulations, the lowest lying excitation samples a variety of electronic states ranging from localized excitons to charge-separated, charge-transfer, and delocalized states. Figure 2 shows the charge density for four typical eigenstates encountered over the course of a given simulation. We characterize these as follows:

- (i) Excitonic (EX) states characterized as having >50% of the electron/hole density on a single molecule.

- The exciton state populates $\approx 58\%$ of the states for simulation A, $\approx 32\%$ for simulation B, and $\approx 52\%$ for simulation C.
- (ii) Charge-Transfer states (CT) characterized as having $>50\%$ of the electron/hole density occupying adjacent molecules. The charge-transfer state populates $\approx 14\%$ of the states for simulation A, $\approx 19\%$ for simulation B, and $\approx 12\%$ for simulation C.
 - (iii) Charge-Separated (CS) states characterized as having $>50\%$ of the electron/hole density occupying a PCBM and a PPV separated by a single molecule. The charge-separated state are populated $\approx 26\%$ for simulation A, $\approx 49\%$ for simulation B, and $\approx 26\%$ for simulation C.
 - (iv) Delocalized states (DLOC), characterized as having $<50\%$ of the electron/hole density on a single PPV or PCBM molecule.

For the most part, the lowest eigenstates in simulations A and B do fall into the categories above. In simulation C, however, the lowest electronic excited state spends about 10% of its time as an eigenstate that cannot be neatly binned into the above categories and corresponds to a fairly equal mixing between excitonic and charge-transfer states and excitonic and charge-separated states.

The striking difference between the blend (C) and the phase separated cases (A and B) is that the stability of localized excitons is very much determined by the proximity between donor and acceptor molecules. In both A and C, the π electrons spend over half their time in excitonic configurations and less than 30% of their time in charge-separated configurations. In both A and C, the 3 PPV chains included in the π system are stacked into the bulk region away from the PCBMs. In contrast in B, charge-separated configurations, defined as a buildup of negative charge on the more distant PCBM, dominate. Only rarely in all cases was the excited state considered as “delocalized.”

The energy of the lowest excited state following excitation at $t = 0$ fs for simulations A and B is shown in Figure 4(a). After excitation there is very little energetic relaxation in all of the systems simulated. The simulations appear to cycle through many adiabatic states in a short period of time leaving the impression of a weak electron-phonon coupling. This can be rationalized as the electron/hole density often delocalize over multiple molecules and many conjugated C-C bonds. Another striking effect of the systems is the large number of avoided crossings that occur between the lowest lying states. There is also a 20 fs oscillation in the CI energies, driving the systems excited states into many regions of strong coupling. The 20 fs oscillation also appears in the autocorrelation and the Fourier transform of the gap energies, contributing the C=C bond stretching modes around $\approx 1600\text{ cm}^{-1}$. The oscillation is contributed to small thermally activated fluctuations within the simulation, showing that even at 100 K the thermal fluctuations possess sufficient energy to bring these states into regions of strong electronic coupling.

In Figure 4(b) we show a histogram of the 5 lowest excitation energies accumulated over 40 ps of simulation time

following promotion to the lowest excited singlet state. The energies take a Gaussian distribution around their respective means and the distributions overlap. On average there is an energy *difference* between 50 and 70 meV between the first and second excited state energies. This suggests that, on average, there is a dense nearly continuous spectrum of charge-separated excited states that can easily be brought into strong electronic coupling by small fluctuations the system brought about by nuclear motion. *In other words, even though the lowest excited state generally can be considered to be an interfacial charge-transfer state, small nuclear motions rapidly mix electronic configurations allowing such states to become delocalized charge-separated states.*

We next consider the origins of the energy fluctuations evidenced in Figure 4(a). While we only show two 200 fs segments of eight 10 ps simulations over this period, one can see that the excitation energies are modulated and cover a small range. The autocorrelation plots of the band gap energies, shown in Figure 5, show that the correlation times for the three simulations are very short ≈ 8 fs meaning that the system changes rapidly enough that the oscillations observed are independent of one another. By taking the Fourier transform of the gap the IR active modes that contribute to the modulation of the excitation energies inside of the systems are found as shown in Figure 5. The modulation of the excitation energy appears to be heavily dependent upon the torsion, C=C, and C-H stretching modes. In each of the plots three distinct regions can be seen, the low frequency torsional modes occur between 200 and 500 cm^{-1} , the C=C stretching modes occur between 1300 and 1800 cm^{-1} , and the C-H stretching modes occur between 2800 and 3300 cm^{-1} . We conclude that small-scale vibronic fluctuations in the molecular structures and orientations produce significant energetic overlap between different adiabatic states to drive the system from purely excitonic to purely charge-transfer on a rapid time-scale. This is evidenced in the progression of the excitation energies, as small fluctuations in these modes can easily bring the excited states into strong coupling regimes.

According to the model outlined below the mean (Δ_0) and variance (\bar{V}) of the energy gap distributions shown in Figure 4 can be used as input to estimate the state to state transition rate for a two-level system. We take $T_d^{-1} \approx \bar{V}/\hbar$ as an estimate of the decoherence time and we introduce τ as the natural lifetimes of each state. The results are shown in Table 1. The estimated transition rates are consistent with the observations that the systems rapidly sample a wide number of possible configurations over the course of the molecular dynamics simulation. On average, the state to state couplings of 56 meV for simulation A and 48 meV for simulation B are comparable to the average energy gaps between the lowest excited states. The strong electronic coupling allows for rapid transitions; however, larger couplings also imply shorter electronic decoherence times, effectively quenching the ability of charges to separate by tunneling.

3. Discussion

We present here the results of hybrid QM/MM simulations of the excited states of model PPV/PCBM heterojunction interfaces. Our results indicate that varying the blend ratio and

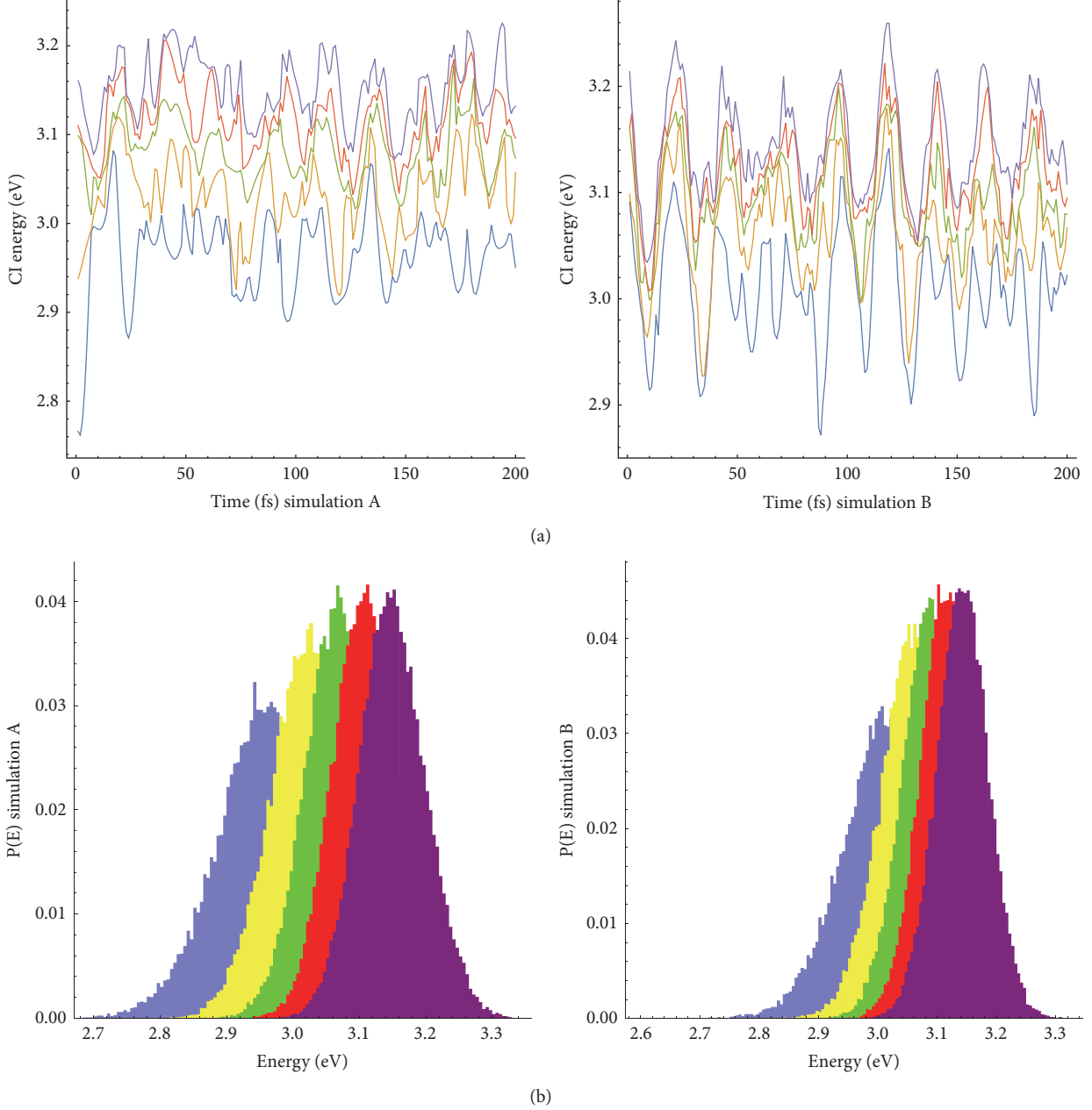


FIGURE 4: (a) Excitation energies for simulations A and B for the first 200 fs following excitation to the lowest SCI state. Each colored line corresponds to the excitation energy from the ground electronic state to one of the lowest 5 singlet excited states. (b) Histogram distributions of the 5 lowest excitation energy levels over a 200 ps simulation. Throughout the simulation, colors of each histogram correspond to the time-histories plotted in (a).

placement of the molecules comprising the heterojunction greatly affect the distribution of states yet have little effect upon the rate constants of the system. We also propose that thermal noise can rapidly change the character of the lowest lying excited state from purely excitonic to charge-separated on a time-scale of sub-100 fs.

Simulations A and C have a very similar placement of molecules, only differing in that simulation A adds a PCBM molecule to the heterojunction. The addition of the PCBM

only slightly changes the distribution of states as seen in Figure 4. The exciton states continue to be the most favoured state inside the system, even slightly increasing in probability, while the delocalized states slightly decrease in probability. Simulation B completely changes the heterojunction, placing three PPV and two PCBM molecules at the interface as seen in Figure 1. The states generated by simulation B are radically different from those seen in simulation A and C as seen in Figure 4. The probability of finding the system in the exciton

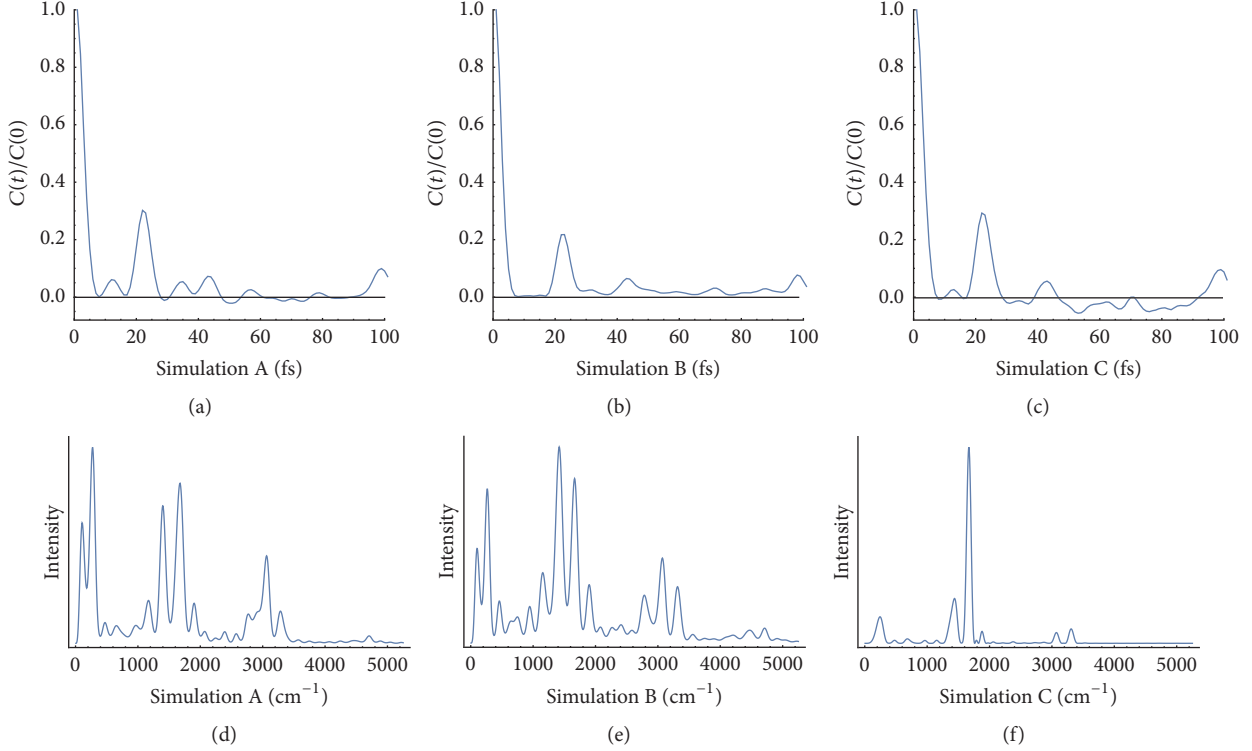


FIGURE 5: (a–c) Autocorrelation of the energy gap between first and second excited states for simulations A, B, and C. The correlation times for all three simulations is 8 fs. (d–f) These plots show the active IR active modes that contribute to the modulation in the CI energies of the systems. Three distinct regions are visible in each plot. The low frequency torsional modes occur between 200 and 500 cm⁻¹, the C=C stretching modes occur between 1300 and 1800 cm⁻¹, and the C-H stretching modes occur between 2800 and 3300 cm⁻¹.

TABLE 1: Estimated excited state ($i \rightarrow f$) transition rates and vibronic couplings for simulations A, B, and C.

| Transition | Δ_o (eV) | $\langle V \rangle$ (eV) | T_d (fs) | k^{-1} (fs) |
|------------|-----------------|--------------------------|------------|---------------|
| A | | | | |
| 1→2 | 0.070 | 0.050 | 13.16 | 19.5 |
| 1→3 | 0.12 | 0.056 | 11.75 | 32.9 |
| 1→4 | 0.16 | 0.063 | 10.45 | 38.9 |
| B | | | | |
| 1→2 | 0.050 | 0.042 | 15.67 | 18.9 |
| 1→3 | 0.09 | 0.049 | 13.43 | 29.3 |
| 1→4 | 0.12 | 0.052 | 12.66 | 40.0 |
| C | | | | |
| 1→2 | 0.11 | 0.057 | 11.41 | 21.8 |
| 1→3 | 0.18 | 0.076 | 8.66 | 28.6 |
| 1→4 | 0.26 | 0.076 | 8.70 | 50.0 |

state is dramatically reduced while the charge-separated state becomes predominant. This result is quite interesting as it highlights that the complexity of simulating heterojunctions resides not only in the size of the system but also on how the donor/accepter interface is chosen.

All three systems start with an exciton localized on the PCBM and dissociating into a charge-transfer state with the

hole (or electron) delocalized over multiple polymer units before localizing to form charge-separated states. There is a wide range of electronic states tightly clustered within a small energy band, allowing small changes in local bond lengths to have a dramatic role in modulating the electronic couplings between excited states. We speculate that the dramatic shift in population seen in simulation B can be caused by disorder in the PPV molecules reducing the band gap by 20 meV. The PPV molecules comprising the interface region undergo large distortions in the C-C torsion angles allowing the molecules to cycle through a larger range of configurations inside of a short time interval. The presence of more π active PPV molecules at the interface also appears to lead to more avoided crossing regions and the ability of the system to more efficiently dissociate excitons into charge-transfer and charge-separated states to a distance to where their Coulombic attraction is comparable to the thermal energy. While the finite size of our system prevents further dissociation of the charges, the results are suggestive that such interstate crossing events driven by bond-fluctuations can efficiently separate the charges. The results presented here corroborate recent ultrafast experimental evidence suggesting that free polarons can form on an ultrafast time scales (sub-100 fs) and that thermally activated low frequency torsional modes are key in effective electron hole separation in PPV/PCBM heterojunctions.

4. Methods

4.1. Simulation Methods. Our simulations employ a modified version of the TINKER molecular dynamics (MD) package [25] in which the MM3 [26] intramolecular bonding parameters are allowed to vary with the local π -electronic density as described by a Parisier-Parr-Pople (PPP) semiempirical Hamiltonian [27, 28]. Similar approaches have been described by Lobaugh and Rossky [29] and Muller and Warshel [30] to include electronic dynamics into an otherwise classical force field description.

We assume that the nuclear dynamics of all atoms in the system evolve according to a classical description

$$m_i \ddot{r}_i(t) = F_i(\mathbf{r}(t), P(t)), \quad (2)$$

where $F_i(\mathbf{r}(t), P(t))$ is the force acting on atom i at time t and $P(t)$ is the instantaneous electronic density for the π -electrons. The Fock operator for the π electrons is given by

$$\begin{aligned} \mathcal{F}_{\mu\mu} &= W_\mu + \frac{1}{2} P_{\mu\mu}^\circ (\mu\mu | \mu\mu) \\ &\quad + \sum_{\rho \neq \mu} (P_{\rho\rho} - Z_\rho) V(r_{\mu\rho}), \end{aligned} \quad (3)$$

$$\mathcal{F}_{\mu\nu} = \beta_{\mu\nu} (r_{\mu\nu}) - \frac{1}{2} P_{\mu\nu}^\circ (\mu\mu | \nu\nu),$$

where W_μ is the valence state potential for a given atom type and we make the zero-differential overlap (ZDO) assumption to write the electronic repulsion integrals as

$$(\mu\nu | \rho\sigma) = (\mu\mu | \rho\rho) \delta_{\mu\nu} \delta_{\rho\sigma}. \quad (4)$$

The Greek indices correspond to atom-centred basis orbitals. Note that we specifically distinguish P° as the ground state (Hartree-Fock) electronic density. Both the hopping integrals $\beta_{\mu\nu}$ and Coulomb repulsion integrals are determined using empirical formulas and depend upon the intermolecular bonding between atoms, accounting for nonplanarity. The molecular orbitals are eigenstates of \mathcal{F}

$$\mathcal{F}\psi_n = \epsilon_n \psi_n, \quad (5)$$

where ψ_n is given as a linear combination of the atom-centred orbitals

$$\psi_n = \sum_\mu c_{n\mu} \chi_\mu. \quad (6)$$

From the $\{c_{n\mu}\}$ coefficients, we obtain the ground state density matrix

$$P_{\mu\nu}^\circ = 2 \sum_{n_{occ}} c_{n\mu} c_{n\nu}. \quad (7)$$

The electronic energy is given by

$$E_{HF} = \text{Tr} [\mathcal{F} P^\circ] \quad (8)$$

and is minimized by imposing the condition

$$\langle [\mathcal{F}, P^\circ] \rangle = 0. \quad (9)$$

Electronic $\pi \rightarrow \pi^*$ excitations are subsequently introduced by using configuration interaction (singles) (CI-S) theory where we write the excited state wave function as a linear combination of elementary excitations between occupied and unoccupied molecular orbitals

$$\begin{aligned} |\Psi_k\rangle &= \sum_{h \in occ} \sum_{e \in unocc} C_k^{eh} |\psi_h \psi_e\rangle \\ &= \sum_{\mu\nu} \left(\sum_{eh} C_k^{eh} c_{e\mu} c_{h\nu} \right) |\chi_\nu \chi_\mu\rangle \\ &= \sum_{\mu\nu} C_k^{\mu\nu} |\chi_\nu \chi_\mu\rangle, \end{aligned} \quad (10)$$

where the $\{C_k^{\mu\nu}\}$ coefficients give the electron/hole amplitude in the atom-centred basis. These are eigenstates of the CI-S Hamiltonian and we used a total of 10 occupied and 10 unoccupied Hartree-Fock molecular orbitals to construct the electron/hole configurations for the CI calculations. The excited state bond charge density matrix is constructed by assuming that electron densities are added to the unoccupied orbitals and hole densities are subtracted from the Hartree-Fock ground state; namely,

$$P_{\mu\nu} = P_{\mu\nu}^\circ + P_{\mu\nu}^e - P_{\mu\nu}^h, \quad (11)$$

where

$$\begin{aligned} P_{\mu\nu}^e &= \sum_\sigma C_k^{\mu\sigma} C_k^{\nu\sigma} \\ P_{\mu\nu}^h &= \sum_\sigma C_k^{\sigma\mu} C_k^{\sigma\nu}. \end{aligned} \quad (12)$$

In the former, we sum over the occupied orbitals (holes) and in the latter we sum over unoccupied orbitals. $P_{\mu\nu}^e$ is interpreted as the “bond charge” matrix whereby the diagonal elements give the net π -electron count on site μ and the off-diagonal $P_{\mu\nu}^e$ terms give the π -bond order between sites μ and ν . Consequently, excitations systematically move electron density from atom to atom and change the local bond orders.

Within the force field, bond force field parameters are modified by assuming a linear interpolation between single and double bonds. For example, we write the bond force constant between C atoms i and j as

$$k = k_2 - \delta k (1 - P_{ij}), \quad (13)$$

where k_2 is the force constant for a C=C double bond when $P_{ij} = 1$, k_1 is the bond force constant for a C-C single bond when $P_{ij} = 0$, and $\delta k = (k_2 - k_1)$. In a similar definition, we interpolate the equilibrium bond lengths between single- and double bonds as

$$l = l_2 + \delta l (1 - P_{ij}). \quad (14)$$

This treatment is not limited to C-C bonds but is applied to all heavy atoms contributing to the π system. While the MM3 parameter set was originally intended to account for the electronic ground state, we assume that the parameters

are transferable to the lower lying excited states. Modifying the equilibrium bond orders and bond lengths allows the MM calculation to respond to the migration of charge.

During the equilibration steps we assume the system to be in its electronic ground state, after which we excite the system to the first excited state and allow the system to respond to the change in the electronic density within the adiabatic Born-Oppenheimer approximation. It is important to note that the excited state we prepare is not the state which carries the most oscillator strength to the ground nor do we account for nonadiabatic surface hopping-type transitions in our approach [31–33]. The dynamics simulations shown reflect the longer-time fate of the lowest lying excited state populations and sample possible configurations that can be accessed by the system. The combination of a classical MD force field with a semiempirical description of a selected few molecules within the system seems to be a suitable compromise between a fully ab initio approach which would be limited to only a few molecules and short simulation times and a fully classical MD description which would neglect any transient changes in the local electronic density [22].

4.2. Estimating State to State Rates. We can estimate the state \rightarrow state rates using the model by Bittner et al. [23, 24]. Consider a two-state system with coupling λ in which the energy gap $\Delta(t)$ fluctuates in time around its average $\bar{\Delta}$. In a two-state basis the Hamiltonian can be written as

$$H = \frac{\Delta(t)}{2} \hat{\sigma}_z + \lambda \hat{\sigma}_x, \quad (15)$$

where $\hat{\sigma}_k$ are Pauli matrices. Note that (15) can be transformed such that fluctuations are in the off-diagonal coupling, becoming

$$H = \frac{\Delta_0}{2} \hat{\sigma}_z + \delta V(t) \hat{\sigma}_x, \quad (16)$$

where $\Delta_0 = \bar{\Delta} + \lambda$ and $\delta \bar{V}(t) = 0$. The fluctuations in the electronic energy levels are attributed to thermal and bond-vibrational motions of polymer chains which can be related to the spectral density, $S(\omega)$, via

$$\bar{V}^2 = \delta \bar{V}^2(t) = \int_{-\infty}^{+\infty} \frac{d\omega}{2\pi} S(\omega). \quad (17)$$

Averaging over the environmental noise, we can write the average energy gap as $\hbar \bar{\Omega} = \sqrt{\Delta_0^2 + \bar{V}^2}$ with eigenstates

$$\begin{aligned} |\Psi+\rangle &= \cos \theta |0\rangle + \sin \theta |1\rangle \\ |\Psi-\rangle &= -\sin \theta |0\rangle + \cos \theta |1\rangle, \end{aligned} \quad (18)$$

where $\tan 2\theta = |\bar{V}|/\Delta_0$ defines the mixing angle between original kets. Consequently, by analysing energy gap fluctuations, we can obtain an estimate of both the coupling between states as well as transition rates. To estimate the average transition rate between states the equations of motion for the

reduced density matrix for a two-level system coupled to a dissipative environment are used.

$$\begin{aligned} \dot{\rho}_{11} &= -\frac{i}{\hbar} V (\rho_{21} - \rho_{12}) - \frac{1}{\tau_1} \rho_{11} \\ \dot{\rho}_{22} &= \frac{i}{\hbar} V (\rho_{21} - \rho_{12}) - \frac{1}{\tau_2} \rho_{22} \\ \dot{\rho}_{12} &= -\frac{i}{\hbar} V (\rho_{22} - \rho_{11}) - \frac{1}{T_d} \rho_{12} - \frac{\Delta_0}{i\hbar} \rho_{12} \\ \dot{\rho}_{21} &= \frac{i}{\hbar} V (\rho_{22} - \rho_{11}) - \frac{1}{T_d} \rho_{21} + \frac{\Delta_0}{i\hbar} \rho_{21}. \end{aligned} \quad (19)$$

τ_1 and τ_2 have been introduced as the lifetimes of each state and T_d is the decoherence time for the quantum superposition. The decoherence time can be related to the spectral density via $T_d^{-1} = \bar{V}/\hbar$. Taking T_d to be short compared to the lifetimes of each state, we can write the population of the initial states as

$$\rho_{11}(t) = \exp \left[-\left(\frac{1}{\tau_1} - k \right) t \right], \quad (20)$$

where k is the average state to state transition rate. If we integrate over all time we obtain an equation of the form

$$\int_0^\infty \rho_{11}(t) dt = \left(\frac{1}{\tau_1} + k \right)^{-1} \quad (21)$$

suggesting a form for the exact solution of (6). Taking the Laplace transform of the equations of motion (6) and assuming that our initial population is in state 1 ($\rho_{11}(0) = 1$) the equations of motion become a series of algebraic equations

$$\begin{aligned} -1 &= -\frac{i}{\hbar} V (\rho_{21} - \rho_{12}) - \frac{1}{\tau_1} \rho_{11} \\ 0 &= \frac{i}{\hbar} V (\rho_{21} - \rho_{12}) - \frac{1}{\tau_2} \rho_{22} \\ 0 &= -\frac{i}{\hbar} V (\rho_{22} - \rho_{11}) - \frac{1}{T_d} \rho_{12} - \frac{\Delta_0}{i\hbar} \rho_{12} \\ 0 &= \frac{i}{\hbar} V (\rho_{22} - \rho_{11}) - \frac{1}{T_d} \rho_{21} + \frac{\Delta_0}{i\hbar} \rho_{21} \end{aligned} \quad (22)$$

which produces a rate constant of the form

$$k = 2 \frac{\bar{V}^2}{\hbar^2} \frac{T_d}{(T_d \Delta_0 / \hbar)^2 + 1}. \quad (23)$$

Conflicts of Interest

The authors declare no financial conflicts of interest.

Authors' Contributions

Eric R. Bittner conceived the project. Allen Kelley performed the simulations and Kush Patel assisted with analysis. All authors contributed to the Results and Discussion and Kush Patel assisted with the drafting of the Methods section.

Acknowledgments

The work at the University of Houston was funded in part by the National Science Foundation (CHE-1362006, CHE-1664971, and MRI-1531814) and the Robert A. Welch Foundation (E-1337).

References

- [1] Z. He, C. Zhong, S. Su, M. Xu, H. Wu, and Y. Cao, "Enhanced power-conversion efficiency in polymer solar cells using an inverted device structure," *Nature Photonics*, vol. 6, no. 9, pp. 591–595, 2012.
- [2] M. Tong, N. E. Coates, D. Moses, A. J. Heeger, S. Beaupré, and M. Leclerc, "Charge carrier photogeneration and decay dynamics in the poly(2,7-carbazole) copolymer PCDTBT and in bulk heterojunction composites with PC70 BM," *Physical Review B: Condensed Matter and Materials Physics*, vol. 81, no. 12, Article ID 125210, 2010.
- [3] L. G. Kaake, D. Moses, and A. J. Heeger, "Coherence and uncertainty in nanostructured organic photovoltaics," *The Journal of Physical Chemistry Letters*, vol. 4, no. 14, pp. 2264–2268, 2013.
- [4] S. Gélinas, A. Rao, A. Kumar et al., "Ultrafast long-range charge separation in organic semiconductor photovoltaic diodes," *Science*, vol. 343, no. 6170, pp. 512–516, 2014.
- [5] E. Collini and G. D. Scholes, "Coherent intrachain energy migration in a conjugated polymer at room temperature," *Science*, vol. 323, no. 5912, pp. 369–373, 2009.
- [6] S. Mukamel, "Comment on ‘coherence and uncertainty in nanostructured organic photovoltaics’," *The Journal of Physical Chemistry A*, vol. 117, no. 40, pp. 10563–10564, 2013.
- [7] N. R. Monahan, K. W. Williams, B. Kumar, C. Nuckolls, and X. Zhu, "Direct observation of entropy-driven electron-hole pair separation at an organic semiconductor interface," *Physical Review Letters*, vol. 114, no. 24, 2015.
- [8] F. Provencher, N. Bérubé, A. W. Parker et al., "Direct observation of ultrafast long-range charge separation at polymer-fullerene heterojunctions," *Nature Communications*, vol. 5, article no. 4288, 2014.
- [9] G. S. Engel, T. R. Calhoun, E. L. Read et al., "Evidence for wavelike energy transfer through quantum coherence in photosynthetic systems," *Nature*, vol. 446, no. 7137, pp. 782–786, 2007.
- [10] D. Beljonne, E. Hennebicq, C. Daniel et al., "Excitation migration along oligophenylenevinylene-based chiral stacks: delocalization effects on transport dynamics," *The Journal of Physical Chemistry B*, vol. 109, no. 21, pp. 10594–10604, 2005.
- [11] H. Tamura, E. R. Bittner, and I. Burghardt, "Exciton dissociation at donor-acceptor polymer heterojunctions: quantum nonadiabatic dynamics and effective-mode analysis," *The Journal of Chemical Physics*, vol. 126, no. 2, p. 021103, 2007.
- [12] G. Grancini, M. Maiuri, D. Fazzi et al., "Hot exciton dissociation in polymer solar cells," *Nature Materials*, vol. 12, no. 1, pp. 29–33, 2013.
- [13] A. Troisi, "How quasi-free holes and electrons are generated in organic photovoltaic interfaces," *Faraday Discussions*, vol. 163, pp. 377–392, 2013.
- [14] H. Tamura, J. G. Ramon, E. R. Bittner, and I. Burghardt, "Phonon-driven ultrafast exciton dissociation at donor-acceptor polymer heterojunctions," *Physical Review Letters*, vol. 100, no. 10, 2008.
- [15] C.-X. Sheng, T. Basel, B. Pandit, and Z. V. Vardeny, "Photoexcitation dynamics in polythiophene/fullerene blends for photovoltaic applications," *Organic Electronics*, vol. 13, no. 6, pp. 1031–1037, 2012.
- [16] X. Yang, T. E. Dykstra, and G. D. Scholes, "Photon-echo studies of collective absorption and dynamic localization of excitation in conjugated polymers and oligomers," *Physical Review B: Condensed Matter and Materials Physics*, vol. 71, no. 4, 2005.
- [17] H. Tamura and I. Burghardt, "Ultrafast charge separation in organic photovoltaics enhanced by charge delocalization and vibronically hot exciton dissociation," *Journal of the American Chemical Society*, vol. 135, no. 44, pp. 16364–16367, 2013.
- [18] Y. Gao, T. P. Martin, E. T. Niles, A. J. Wise, A. K. Thomas, and J. K. Grey, "Understanding morphology-dependent polymer aggregation properties and photocurrent generation in poly-thiophene/fullerene solar cells of variable compositions," *The Journal of Physical Chemistry C*, vol. 114, no. 35, pp. 15121–15128, 2010.
- [19] N. S. Sariciftci and A. J. Heeger, "Reversible, metastable, ultrafast photoinduced electron transfer from semiconducting polymers to buckminsterfullerene and in the corresponding donor/acceptor heterojunctions," *International Journal of Modern Physics B*, vol. 08, no. 03, pp. 237–274, 1994.
- [20] N. Banerji, S. Cowan, M. Leclerc, E. Vauthey, and A. J. Heeger, "Exciton formation, relaxation, and decay in PCDTBT," *Journal of the American Chemical Society*, vol. 132, no. 49, pp. 17459–17470, 2010.
- [21] N. Banerji, "Sub-picosecond delocalization in the excited state of conjugated homopolymers and donor-acceptor copolymers," *Journal of Materials Chemistry C*, vol. 1, no. 18, pp. 3052–3066, 2013.
- [22] A. E. Jailaubekov, A. P. Willard, J. R. Tritsch et al., "Hot charge-transfer excitons set the time limit for charge separation at donor/acceptor interfaces in organic photovoltaics," *Nature Materials*, vol. 12, no. 1, pp. 66–73, 2013.
- [23] E. R. Bittner and C. Silva, "Noise-induced quantum coherence drives photo-carrier generation dynamics at polymeric semiconductor heterojunctions," *Nature Communications*, vol. 5, article no. 3119, 2014.
- [24] E. R. Bittner and A. Kelley, "The role of structural fluctuations and environmental noise in the electron/hole separation kinetics at organic polymer bulk-heterojunction interfaces," *Physical Chemistry Chemical Physics*, vol. 17, no. 43, pp. 28853–28859, 2015.
- [25] J. W. Ponder, "TINKER: Software Tools for Molecular Design," <http://dasher.wustl.edu/tinker/>, 2004.
- [26] N. L. Allinger, F. Li, L. Yan, and J. C. Tai, "Molecular mechanics (MM3) calculations on conjugated hydrocarbons," *Journal of Computational Chemistry*, vol. 11, no. 7, pp. 868–895, 1990.
- [27] J. A. Pople, "Electron interaction in unsaturated hydrocarbons," *Transactions of the Faraday Society*, vol. 49, pp. 1375–1385, 1953.
- [28] R. Pariser and R. G. Parr, "A semi-empirical theory of the electronic spectra and electronic structure of complex unsaturated molecules. II," *The Journal of Chemical Physics*, vol. 21, no. 5, pp. 767–776, 1953.
- [29] J. Lobaugh and P. J. Rossky, "Solvent and intramolecular effects on the absorption spectrum of betaine-30," *The Journal of Physical Chemistry A*, vol. 104, no. 5, pp. 899–907, 2000.
- [30] R. P. Muller and A. Warshel, "Ab initio calculations of free energy barriers for chemical reactions in solution," *The Journal of Physical Chemistry C*, vol. 99, no. 49, pp. 17516–17524, 1995.

- [31] J. C. Tully, "Molecular dynamics with electronic transitions," *The Journal of Chemical Physics*, vol. 93, no. 2, pp. 1061–1071, 1990.
- [32] J. C. Tully and R. K. Pkeston, "Trajectory surface hopping approach to nonadiabatic molecular collisions: the reaction of H⁺ with D₂," *The Journal of Chemical Physics*, vol. 55, no. 2, pp. 562–572, 1971.
- [33] G. Granucci and M. Persico, "Critical appraisal of the fewest switches algorithm for surface hopping," *The Journal of Chemical Physics*, vol. 126, no. 13, Article ID 134114, 2007.

Research Article

Temperature Dependence of the Energy Band Diagram of AlGaN/GaN Heterostructure

Yanli Liu ,¹ Dunjun Chen ,² Kexiu Dong,³ Hai Lu,² Rong Zhang,² Youdou Zheng,² Zhilin Zhu,¹ Guangfen Wei,¹ and Zhonghai Lin¹

¹Key Laboratory of Intelligent Information Processing in Universities of Shandong,

School of Information and Electronic Engineering, Shandong Technology and Business University, Yantai 264005, China

²Key Laboratory of Advanced Photonic and Electronic Materials, School of Electronic Science and Engineering,

Nanjing University, Nanjing 210093, China

³School of Electronic and Electrical Engineering, Chuzhou University, Chuzhou 239000, China

Correspondence should be addressed to Yanli Liu; yanliliu0727@163.com and Dunjun Chen; djchen@nju.edu.cn

Received 5 January 2018; Accepted 30 January 2018; Published 1 April 2018

Academic Editor: Shenghuang Lin

Copyright © 2018 Yanli Liu et al. This is an open access article distributed under the Creative Commons Attribution License, which permits unrestricted use, distribution, and reproduction in any medium, provided the original work is properly cited.

Temperature dependence of the energy band diagram of AlGaN/GaN heterostructure was investigated by theoretical calculation and experiment. Through solving Schrodinger and Poisson equations self-consistently by using the Silvaco Atlas software, the energy band diagram with varying temperature was calculated. The results indicate that the conduction band offset of AlGaN/GaN heterostructure decreases with increasing temperature in the range of 7 K to 200 K, which means that the depth of quantum well at AlGaN/GaN interface becomes shallower and the confinement of that on two-dimensional electron gas reduces. The theoretical calculation results are verified by the investigation of temperature dependent photoluminescence of AlGaN/GaN heterostructure. This work provides important theoretical and experimental basis for the performance degradation of AlGaN/GaN HEMT with increasing temperature.

1. Introduction

AlGaN/GaN high electron mobility transistor (HEMT) has attracted great interest for high temperature, high frequency, and high power applications due to its intrinsic material advantages, such as wide band gap, high breakdown electric field, high electron saturation velocity, and high two-dimensional electron gas (2DEG) concentration [1–3]. Although the performance of AlGaN/GaN HEMT has made remarkable progress [4–7], the reliability, especially at high temperature, has been and remains a major constraint in realizing the true potentials of such devices [8–10]. Improvements of reliability require a better understanding of the degradation mechanism. The performance degradation of AlGaN/GaN HEMTs with increasing temperature can be largely attributed to the effect of temperature on 2DEG transport properties [10–12]. The intrinsic physical reason for that is the energy band diagram of AlGaN/GaN heterostructure varies with temperature, which should be fully investigated.

However, there have been few reports on the temperature dependence of the energy band structure of AlGaN/GaN heterostructures until now. Wang et al. [13] calculated the energy band diagram of AlGaN/GaN heterostructure at room temperature, 250°C and 500°C, just to explain that the 2DEG density decreases with increasing temperature. But there is not detailed analysis and discussion. In this work, the temperature dependence of the energy band structure of AlGaN/GaN heterostructure was investigated by theoretical calculation and experimental verification.

2. Theoretical Calculation

The AlGaN/GaN heterostructure used in this study consists of a 2 μm thick GaN buffer layer and a 25 nm thick AlGaN barrier layer, as shown in Figure 1. The Al composition of the AlGaN layer is 0.3. The n-type doping level in both GaN and AlGaN layers is set to be $1 \times 10^{16} \text{ cm}^{-3}$, to keep consistent with the level for unintentionally doped samples

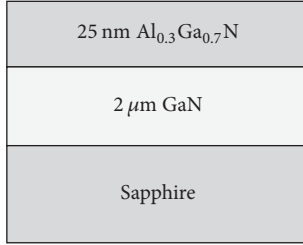


FIGURE 1: Schematic of AlGaN/GaN heterostructure.

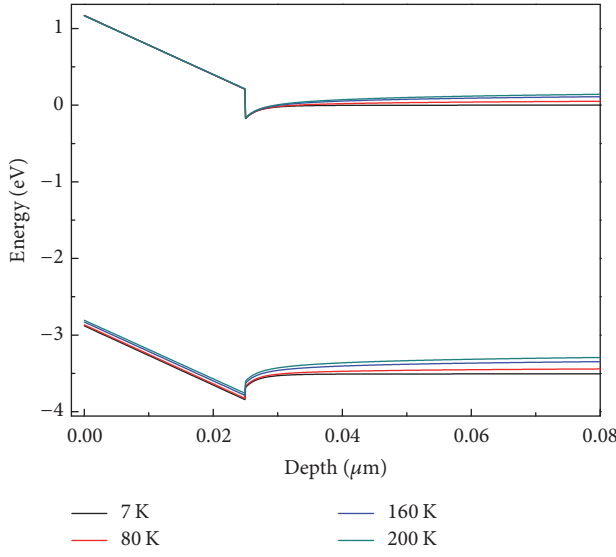


FIGURE 2: The energy band diagrams of AlGaN/GaN heterostructure at different temperature.

in experiment. Considering the screening effect caused by defects, the polarization charge densities are assumed to be 40% of the calculated values [14].

Through solving the Schrodinger and Poisson equations self-consistently by using the Silvaco Atlas software [15], the temperature dependent energy band diagram of AlGaN/GaN heterostructure can be calculated. The calculation results with temperature lower than 200 K are shown in Figure 2. It can be seen that the conduction and valence band energies of both GaN and AlGaN layers increase with increasing temperature, especially in the GaN layer. Compared with the conduction band, the valence band shows larger shift with varying temperature. So, the energy band gaps of GaN and AlGaN layers decrease with increasing temperature. This is consistent with temperature dependent band gap shrinkage effect [16, 17].

Besides the energy band gaps, the conduction band offset of AlGaN/GaN heterostructure also changes with temperature. The conduction band profile near the AlGaN/GaN interface with varying temperature is shown in Figure 3. It can be seen that the conduction band offset between AlGaN and GaN layers decreases with increasing temperature, which means that the depth of the quantum well at AlGaN/GaN interface becomes shallower and the confinement of that

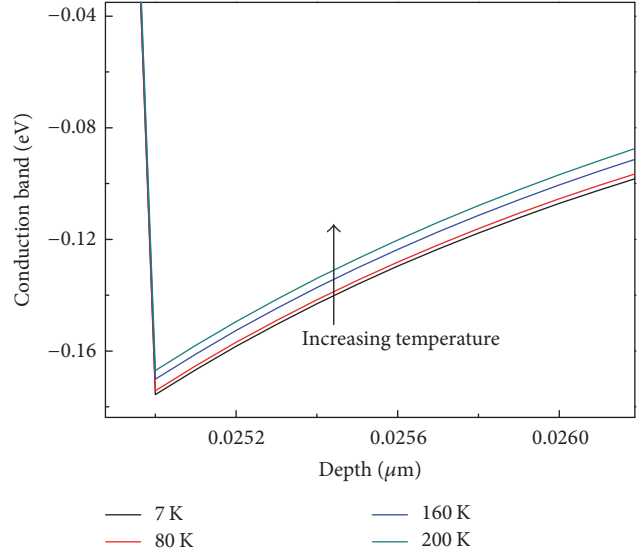


FIGURE 3: The conduction band profile of the AlGaN/GaN interface for different temperature.

on 2DEG reduces. In addition, the 2DEG concentration in unintentionally doped AlGaN/GaN heterostructures shows a direct proportional relationship to the conduction band offset, according to the following equation [13]:

$$n_s(x) = \frac{\sigma(x)}{e} - \left(\frac{\epsilon_0 \epsilon(x)}{d_{\text{AlGaN}} e^2} \right) [e\phi_b(x) + E_F(x) - \Delta E_c(x)], \quad (1)$$

where $\sigma(x)$ is the polarization-induced bound charge, $\epsilon(x)$ is the relative dielectric constant of AlGaN, d_{AlGaN} is the thickness of the $\text{Al}_x\text{Ga}_{1-x}\text{N}$ barrier layer, $e\phi_b(x)$ is the Schottky barrier of the gate contact on top of AlGaN, $E_F(x)$ is the Fermi level with respect to the GaN conduction-band-edge energy, and $\Delta E_c(x)$ is the conduction band offset at AlGaN/GaN interface. So, the 2DEG concentration decreases with increasing temperature due to the reduction of the conduction band offset ΔE_c . The same temperature dependence of the 2DEG concentration has been measured by Khan et al. [18]. Therefore, the performance of AlGaN/GaN HEMT will degrade with increasing temperature [19]. The detailed temperature dependence of the energy band gaps and conduction band offset in AlGaN/GaN heterostructure is shown in Figure 4.

3. Experimental Verification

In order to verify the theoretical calculation, we investigated temperature dependent photoluminescence (PL) of AlGaN/GaN heterostructure, which can directly reflect the energy band structure of the measured samples. In this work, PL measurements were performed on the $\text{Al}_{0.3}\text{Ga}_{0.7}\text{N}/\text{GaN}$ heterostructure between 7 K and 200 K. The light source was a He-Cd laser with a wavelength of 325 nm.

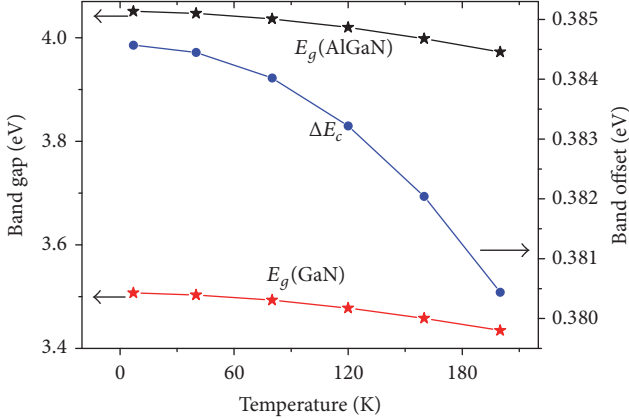


FIGURE 4: Temperature dependence of the energy band gaps of AlGaN and GaN and the conduction band offset of AlGaN/GaN heterostructure.

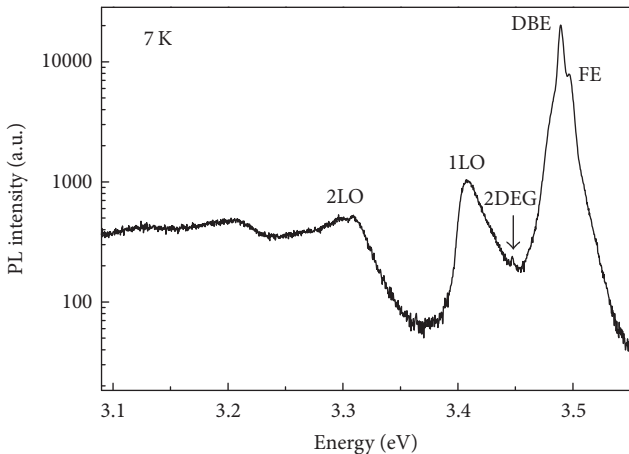


FIGURE 5: PL spectrum of AlGaN/GaN heterostructure at 7 K.

Figure 5 shows the PL spectrum of the AlGaN/GaN heterostructure at 7 K. The free exciton (FE) and donor bound exciton (DBE) emissions in GaN are located at 3.498 eV and 3.489 eV, respectively, and are much stronger than other peaks. These two emissions are near-band-edge emissions, which can directly reflect the band gap of corresponding material. The broad peaks at 3.408 eV and 3.309 eV are attributed to the one and two longitudinal optical (LO) phonon replicas of the GaN FE emission, respectively. The weak peak at 3.448 eV is attributed to recombination between 2DEG and photoexcited holes. Due to the strong built-in internal electric field near AlGaN/GaN heterointerface, the photoexcited holes diffuse rapidly into the flat-band region of GaN. Therefore, the probability of recombination between 2DEG and photoexcited holes is low and its intensity is very weak.

Figure 6 shows the PL spectra of AlGaN/GaN heterostructure with varying temperature in the range of 7 K to 160 K. The inset shows the PL spectrum at 200 K. It can be seen from Figure 6 that the GaN FE and DBE emissions

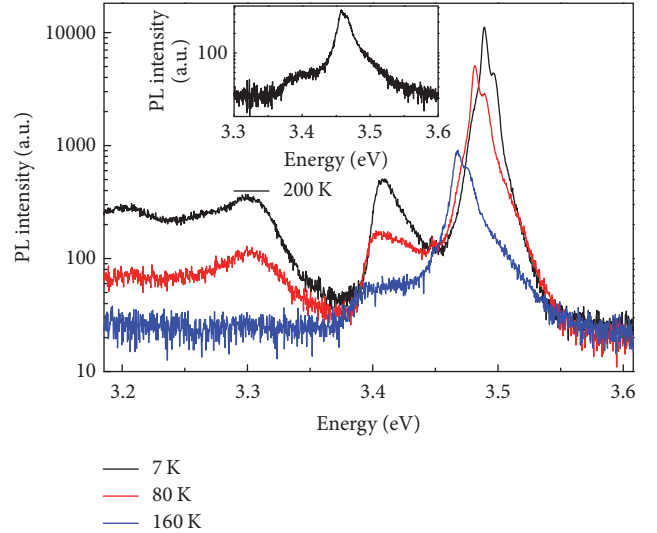


FIGURE 6: PL spectra of AlGaN/GaN heterostructure in the temperature range of 7 K to 160 K. The inset shows the PL spectrum of AlGaN/GaN heterostructure at 200 K.

exhibit obvious red shift with increasing temperature, indicating the reduction of the band gap of GaN layer. This is consistent with the result of theoretical calculation. The intensity of the 2DEG PL peak is very weak and decreases with increasing temperature. As shown in the inset of Figure 6, this peak disappears when the temperature reaches 200 K. Different from the GaN FE and DBE peaks, the 2DEG PL peak shows unobvious shift with increasing temperature. It demonstrates that the energy separation between the ground state of 2DEG and the valence band of flat-band region in GaN layer does not change obviously with varying temperature in the range of 7 K to 200 K. Additionally, the energy separation between GaN FE and 2DEG PL peak gradually decreases with increasing temperature, which indicates the depth of quantum well at AlGaN/GaN interface becomes shallower. Therefore, the confinement of the interface quantum well on 2DEG decreases with increasing temperature. It is also consistent with the theoretical calculation results.

4. Conclusions

In summary, temperature dependence of the energy band diagram of AlGaN/GaN heterostructure was investigated. Through theoretical calculation and experiment verification, it is confirmed that the band gaps of both AlGaN and GaN layers and the conduction band offset of AlGaN/GaN heterostructure decrease with increasing temperature in the range of 7 K to 200 K. So the depth of quantum well at AlGaN/GaN interface becomes shallower and the confinement of that on 2DEG reduces. This work provides important theoretical and experimental basis for the performance degradation of AlGaN/GaN HEMT with increasing temperature.

Conflicts of Interest

The authors declare that there are no conflicts of interest regarding the publication of this paper.

Acknowledgments

This work was supported by the National Natural Science Foundation of China (nos. 61634002, 61474060, and 61174007), National Key R&D Program of China (2017YFB0402900), the Natural Science Foundation of Shandong Province (ZR2016FP09), the Project of Shandong Province Higher Educational Science and Technology Program (J16LN04), the Key Project of Jiangsu Province (BE2016174), the Yantai Key R&D Program (nos. 2017ZH063, 2017ZH064, and 2016ZH053), the PhD Start-Up Fund of Shandong Technology and Business University (BS201608), and the Natural Science Foundation of Anhui Province (1708085MF149).

References

- [1] U. K. Mishra, P. Parikh, and Y.-F. Wu, "AlGaN/GaN HEMTs—an overview of device operation and applications," *Proceedings of the IEEE*, vol. 90, no. 6, pp. 1022–1031, 2002.
- [2] A. Eblabla, X. Li, I. Thayne, D. J. Wallis, I. Guiney, and K. Elgaid, "High performance GaN high electron mobility transistors on low resistivity silicon for X-band applications," *IEEE Electron Device Letters*, vol. 36, no. 9, pp. 899–901, 2015.
- [3] Y. Tang, K. Shinohara, D. Regan et al., "Ultrahigh-speed GaN high-electron-mobility transistors with fTfmax of 454/444 GHz," *IEEE Electron Device Letters*, vol. 36, no. 6, pp. 549–551, 2015.
- [4] L. F. Eastman, V. Tilak, V. Kaper et al., "Progress in high-power, high frequency AlGaN/GaN HEMTs," *Physica Status Solidi (a) – Applications and Materials Science*, vol. 194, no. 2, pp. 433–438, 2015.
- [5] S. Huang, X. Liu, J. Zhang et al., "High RF Performance Enhancement-Mode Al₂O₃/AlGaN/GaN MIS-HEMTs Fabricated with High-Temperature Gate-Recess Technique," *IEEE Electron Device Letters*, vol. 36, no. 8, pp. 754–756, 2015.
- [6] M. Zhang, X.-H. Ma, M.-H. Mi et al., "Improved on-state performance of AlGaN/GaN Fin-HEMTs by reducing the length of the nanochannel," *Applied Physics Letters*, vol. 110, no. 19, Article ID 193502, pp. 287–292, 2017.
- [7] L. Shen, D. Zhang, X. Cheng et al., "Performance Improvement and Current Collapse Suppression of Al₂O₃/AlGaN/GaN HEMTs Achieved by Fluorinated Graphene Passivation," *IEEE Electron Device Letters*, vol. 38, no. 5, pp. 596–599, 2017.
- [8] G. Meneghesso, G. Verzellesi, F. Danesin et al., "Reliability of GaN high-electron-mobility transistors: State of the art and perspectives," *IEEE Transactions on Device and Materials Reliability*, vol. 8, no. 2, pp. 332–343, 2008.
- [9] Y. C. Chou, D. Leung, I. Smorchkova et al., "Degradation of AlGaN/GaN HEMTs under elevated temperature lifetesting," *Microelectronics Reliability*, vol. 44, no. 7, pp. 1033–1038, 2004.
- [10] J. Yang, X. Zhang, and C. Lv, "Study on the reliability of AlGaN/GaN HEMTs at high temperature," in *Proceedings of the 2011 International Conference on Electric Information and Control Engineering (ICEICE '11)*, pp. 774–777, China, April 2011.
- [11] A. M. Darwish, B. D. Huebschman, E. Viveiros, and H. A. Hung, "Dependence of GaN HEMT millimeter-wave performance on temperature," *IEEE Transactions on Microwave Theory and Techniques*, vol. 57, no. 12, pp. 3205–3211, 2009.
- [12] G. J. Syaranamual, W. A. Sasangka, R. I. Made et al., "Role of two-dimensional electron gas (2DEG) in AlGaN/GaN high electron mobility transistor (HEMT) ON-state degradation," *Microelectronics Reliability*, vol. 64, pp. 589–593, 2016.
- [13] M. J. Wang, B. Shen, F. J. Xu et al., "High temperature dependence of the density of two-dimensional electron gas in Al_{0.18}Ga_{0.82}N/GaN heterostructures," *Applied Physics A: Materials Science & Processing*, vol. 88, no. 4, pp. 715–718, 2007.
- [14] K. Dong, D. Chen, B. Liu et al., "Characteristics of polarization-doped N-face III-nitride light-emitting diodes," *Applied Physics Letters*, vol. 100, no. 7, Article ID 073507, 2012.
- [15] A. Abou-Elnour and K. Schuenemann, "A comparison between different numerical methods used to solve Poisson's and Schroedinger's equations in semiconductor heterostructures," *Journal of Applied Physics*, vol. 74, no. 5, pp. 3273–3276, 1993.
- [16] N. Sarkar and S. Ghosh, "Temperature dependent band gap shrinkage in GaN: Role of electron-phonon interaction," *Solid State Communications*, vol. 149, no. 31–32, pp. 1288–1291, 2009.
- [17] N. Nepal, J. Li, M. L. Nakarmi, J. Y. Lin, and H. X. Jiang, "Temperature and compositional dependence of the energy band gap of AlGaN alloys," *Applied Physics Letters*, vol. 87, no. 24, Article ID 242104, pp. 1–3, 2005.
- [18] A. Khan, F. Shah, J. Siddiq, and T. Vasen, "High temperature transport properties of AlGaN/GaN heterostructures," *Nd.Edu*, vol. 1, pp. 1–4, 2010.
- [19] B. A. Polash and H. Huq, "High temperature performance measurement and analysis of GaN HEMTs," in *Proceedings of the Society of Photo-Optical Instrumentation Engineers (SPIE)*, vol. 6894, January 2008.

Research Article

Structural and Optical Properties of α -Quartz Cluster with Oxygen-Deficiency Centers

Yin Li ,^{1,2} Xi Chen ,^{1,3} Chuanghua Yang,⁴ Liyuan Wu,¹ and Ru Zhang ,^{1,3}

¹State Key Laboratory of Information Photonics and Optical Communications, Beijing University of Posts and Telecommunications, Beijing 100876, China

²School of Science, Beijing University of Posts and Telecommunications, Beijing 100876, China

³School of Ethnic Minority Education, Beijing University of Posts and Telecommunications, Beijing 102209, China

⁴School of Physics and Telecommunication Engineering, Shaanxi University of Technology, Hanzhong 723001, China

Correspondence should be addressed to Ru Zhang; optics219@163.com

Received 27 August 2017; Accepted 26 November 2017; Published 1 April 2018

Academic Editor: Zhike Liu

Copyright © 2018 Yin Li et al. This is an open access article distributed under the Creative Commons Attribution License, which permits unrestricted use, distribution, and reproduction in any medium, provided the original work is properly cited.

The structural and optical properties of α -quartz cluster with oxygen-deficiency centers (ODCs) defects have been investigated based on the density functional theory (DFT). For cluster models with ODC(I) defect, with the increasing of cluster size and shape, the equilibrium length of Si-Si bond decreases. The excitation peaks of cluster models with ODC(I) defect are from 6.87 eV to 7.39 eV, while the excitation peaks of cluster models with ODC(II) defect are from 5.20 eV to 5.47 eV. We also study the interconversion between ODCs ($\equiv\text{Si}-\text{Si}\equiv$ bond and divalent Si) induced by UV irradiation. Our study predicted the existence of a metastable structure of ODC(I) for the first time in literature. Our results are in good agreement with the previous results and provide strong theoretical support to the viability of the processes.

1. Introduction

As one of the most important crystalline oxides, α -quartz is widely used in microelectronics, piezoelectric devices, optical elements, and geological dating, as well as a support in heterogeneous catalysis and other fields of research and technology. Up to now, a large number of experimental and theoretical studies have been devoted to the characterization of the structure of point defects in α -quartz [1–3]. Among many defect centers in α -quartz, oxygen-deficiency centers (ODCs) are believed to play a vital role in the irradiation process and subsequent photostructural changes [4] and thus have attracted much attention in research [5–10].

The crystal structure and symmetry determine that at least two distinct diamagnetic ODCs can form in SiO_2 and they are commonly denoted as ODC(I) and ODC(II), giving rise to the photoabsorption bands at ~ 7.6 and ~ 5.0 eV, respectively [4, 11]. ODC(I) is a general consensus of the “relaxed oxygen vacancy,” namely, the $\equiv\text{Si}-\text{Si}\equiv$ bond, having

a Si-Si bond distance about 2.3 Å [4]. As for ODC(II), there has been a large amount of controversy [4, 12–14] on the structural model. At least two alternatives were proposed. One is the “unrelaxed oxygen monovacancy,” namely, the $\equiv\text{Si}\cdots\text{Si}\equiv$ bond, having a $\text{Si}\cdots\text{Si}$ distance similar to that of regular Si-O-Si bonding (3.1 Å) [11], and the other is the “divalent Si,” having two Si-O bonds and a lone pair of electrons in a Si sp^2 hybrid orbital [15–17].

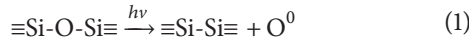
It has been found that the completely unrelaxed geometry with a Si-Si distance of 3.1 Å is not a stable arrangement and is unlikely for the ground state [17]. Indeed, the observed optical properties of ODC(II) can be reproduced almost satisfactorily by the divalent Si model rather than the unrelaxed oxygen vacancy model [18–20]. It seems that ODC(II) is more inclined to the divalent Si model. On the other hand, some researchers have shown that even a puckered unrelaxed oxygen vacancy proposed originally for α -quartz has a barrier of only ~ 0.2 –0.3 eV against the relaxation into the stable $\equiv\text{Si}-\text{Si}\equiv$ bond [21, 22]. It was suggested that an interconversion

TABLE 1: Structural properties of the six cluster models with ODC defects in Figure 1.

| Cluster size | Bond length (Å) | | | Bond angle (degree) | |
|---|-----------------|-------|-------|---------------------|--------|
| | d_1 | d_2 | d_3 | O-Si-O | Si-O-H |
| Si_2H_6 | 2.34 | 1.48 | 1.48 | — | — |
| $\text{Si}_2\text{O}_6\text{H}_6$ | 2.67 | 1.65 | 1.64 | 105.89 | 127.82 |
| $\text{Si}_5\text{O}_{15}\text{H}_{12}$ | 2.53 | 1.77 | 1.65 | 107.17 | 132.68 |
| $\text{Si}_8\text{O}_{24}\text{H}_{18}$ | 2.43 | 1.62 | 1.63 | 109.25 | 131.94 |
| SiO_2H_2 | 1.63 | 1.63 | 0.80 | 100.90 | — |
| $\text{Si}_3\text{O}_8\text{H}_6$ | 1.67 | 1.64 | 1.62 | 107.70 | 132.19 |

may occur between the divalent defect and the relaxed oxygen vacancy upon ultraviolet irradiation, although a detailed mechanism of this interconversion is unknown.

In theoretical studies, it is generally accepted that the main intrinsic defect process in SiO_2 is the Frenkel mechanism, that is, formation of a pair of an oxygen monovacancy (Si-Si bond) and an interstitial oxygen atom (O^0) from a regular Si-O-Si bond. This mechanism has been verified in amorphous SiO_2 [23–28], where its disordered structure influences both the defect creation and migration. Furthermore, clear experimental evidence for (1) in the ordered lattice of crystalline SiO_2 has been given [29]. However, the remaining main unsolved question about ODC(II) is to explain the observed close relationships between ODC(II) and ODC(I). Both centers accommodate the same amount of oxygen deficiency and it is suggested that at some configurations they can interconvert. Details of this process in α -quartz are still not unambiguously established [30]



In order to reveal preferable structure of α -quartz cluster with ODC(I) defect and the intrinsic mechanism of structural conversion from ODC(I) to ODC(II) in α -quartz clusters, we apply the first-principles calculation to different cluster models. The size and shape effect of cluster models is included. Our study predicted the existence of a metastable structure of ODC(I) for the first time in literature. Our results also suggested the mechanism of structural conversion from ODC(I) to ODC(II) in α -quartz clusters. We applied the first-principle calculation based on density functional theory (DFT) and time dependent density functional theory (TDDFT) implemented in ORCA program to the electronic structure properties and optical properties. Our paper is organized as follows. In Section 2, the models and methods are described. The results and discussions are presented in Section 3. Finally, a summary of the main conclusions of this work is given in Section 4.

2. Computational Methods

We have studied clusters with various size. The formulas are Si_2H_2 , $\text{Si}_2\text{O}_6\text{H}_6$, $\text{Si}_5\text{O}_{15}\text{H}_{12}$, $\text{Si}_8\text{O}_{24}\text{H}_{18}$, SiO_2H_2 , and $\text{Si}_3\text{O}_8\text{H}_6$, as shown in Figure 1.

In order to avoid the spurious states caused by the $-\text{O}^0$ defects located the boundary of the cluster, we use hydrogen atoms to passivate all clusters. The distance between the

capping hydrogen atoms and the oxygen atoms is 0.80 Å [31]. In the process of optimization, the interior atoms were allowed to move freely, while the terminal hydrogen atoms and surface oxygen atoms were frozen. The main geometrical parameters are given for each cluster in Table 1.

The ORCA quantum chemistry program was used in all calculations. DFT and the hybrid density functional B3LYP method [32, 33] were employed to perform the geometry optimization. Following geometry optimization, TDDFT (nroots = 16) was used for the sake of calculating the electronic excited states. Triple- ζ -quality basis sets with one set of polarization functions (TZVP) were employed for the Si, O, and H atoms, respectively [34]. In the self-consistent field calculations, tight scf convergence and a dense integration grid were selected. The maximum element of the direct inversion of iterative subspaces (DIIS) error vector is set as 5×10^{-7} . The structural optimization is allowed to be relaxed until the maximum force on each atom becomes less than 0.01 eV/Å and maximum energy change between two steps is smaller than 1×10^{-8} Eh. The density change is no more than 1×10^{-7} Eh [35, 36].

3. Results and Discussion

3.1. Preferable Structure of α -Quartz Cluster with ODC(I) Defect. ODC(I) defect pair is created by shifting an interstitial oxygen atom (O^0) from a regular Si-O-Si bond and constitutes a pair of an oxygen monovacancy (Si-Si bond) (see (1)). In (1), bonds with three oxygen atoms were represented by \equiv . For the purpose of finding out the cluster models which have the stable structure, prediction of the apposite Si-Si band length becomes a key object. The Si-Si band length (d_1) increased from 2.0 Å to 3.5 Å, which is the main structure change, as shown in Figures 1(a)–1(d). Figure 2 shows the relationship between the total energy and Si-Si bond length in singlet state of four clusters with ODC(I) defects. The total energy of the α -quartz clusters will have the lowest value along with the increasing of the Si-Si bond length. The cluster size can represent a bulk structure. In order to describe the singlet state adequately, relaxation processes were performed with four cluster models.

To improve the accuracy of the calculations, we consider the parent molecule disilane, Si_2H_6 cluster model (see Figure 1(a)). The cluster model contains a direct Si-Si bond. As a result of the structural scan and geometry optimization, we have found that, in Figure 2(a), the equilibrium bond length in singlet state of Si_2H_6 cluster model is 2.34 Å, similar to

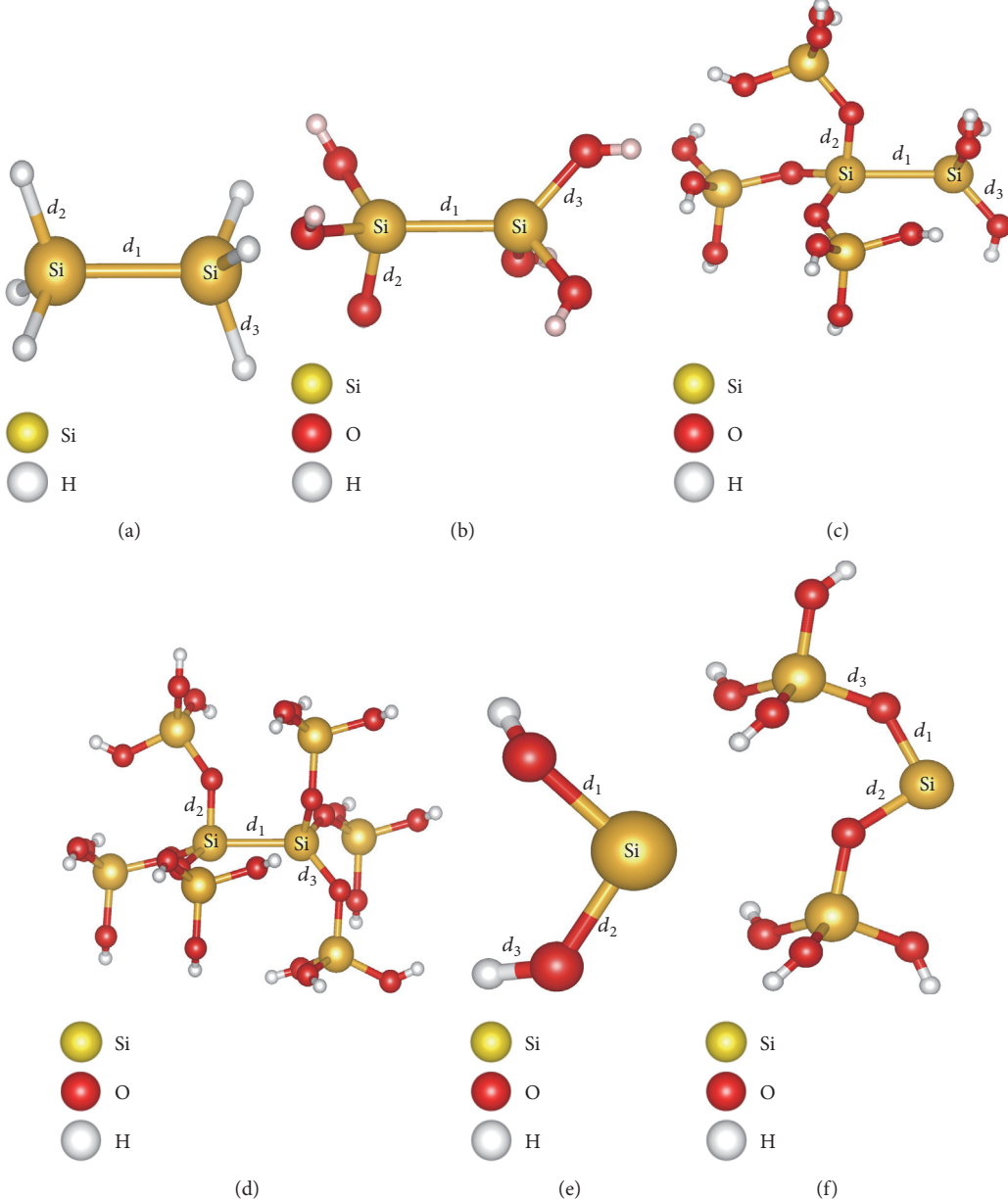


FIGURE 1: Illustrations of each of the six clusters used for $S_0 \rightarrow S_1$ transition energy for α -quartz cluster configurations with oxygen-deficiency centers. (a) Si_2H_6 with ODC(I), (b) $\text{Si}_2\text{O}_6\text{H}_6$ with ODC(I), (c) $\text{Si}_5\text{O}_{15}\text{H}_{12}$ with ODC(I), (d) $\text{Si}_8\text{O}_{24}\text{H}_{18}$ with ODC(I), (e) $\text{Si}_2\text{O}_2\text{H}_2$ with ODC(II), and (f) $\text{Si}_3\text{O}_8\text{H}_6$ with ODC(II). We use hydrogen atoms to passivate the oxygen atoms which terminate our cluster models.

the ordinary Si-Si bond length of 2.36 Å [31]. However, Figures 2(b)-2(d) show that the singlet state equilibrium bond lengths of $\text{Si}_2\text{O}_6\text{H}_6$, $\text{Si}_5\text{O}_{15}\text{H}_{12}$, and $\text{Si}_8\text{O}_{24}\text{H}_{18}$ cluster models are 2.67 Å, 2.53 Å, and 2.43 Å. With the increasing of cluster size and shape, the equilibrium Si-Si bond length decreases.

3.2. Electronic Structure Properties and Optical Properties of ODC(I). We compared the electronic density of states (DOS) of the four clusters with ODC(I) defects (see Figure 1) so that the geometric effect on the electronic structure can be seen clearly. Figure 3 shows the total electronic DOS for Si_2H_6 , $\text{Si}_2\text{O}_6\text{H}_6$, $\text{Si}_5\text{O}_{15}\text{H}_{12}$, and $\text{Si}_8\text{O}_{24}\text{H}_{18}$ clusters. In a nutshell,

the electronic DOS of all the clusters shows notable structural sensitivity. The DOS for Si_2H_6 cluster reveals more uniform distributions than the other three cases, because of the small size. When the valence band states participate in optical transitions of point defects, the structural dependence of electronic state will result in different OA spectra.

The wave function of highest occupied molecular orbital (HOMO) and the electron localization function (ELF) are used to analyze the electronic structure of cluster with ODC(I) defect. We calculate the ELF and the wave function of HOMO on four clusters (see Figures 1(a)-1(d)) to clarify the charge distribution around ODC(I) defect. From the electron

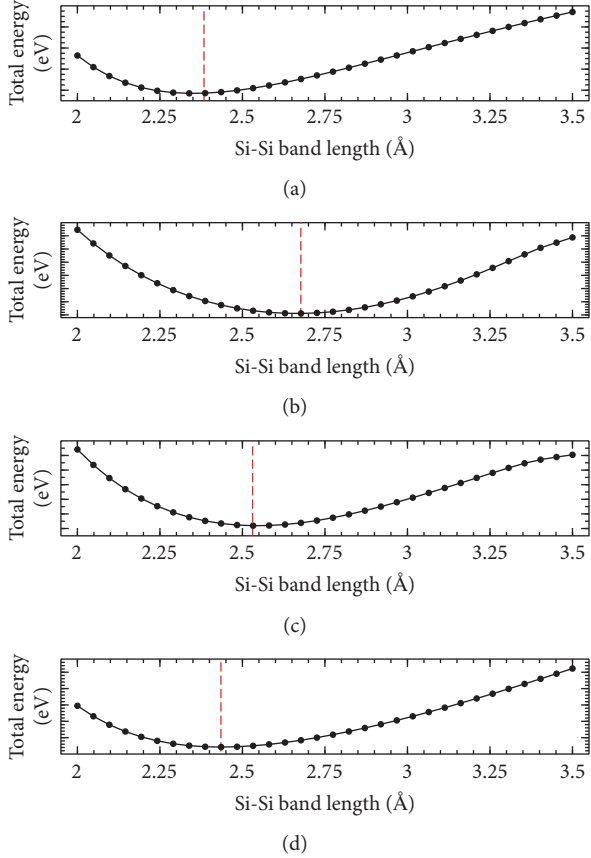


FIGURE 2: The relationship between total energy and Si-Si bond length in the four clusters with ODC(I) defects. (a) Si_2H_6 , (b) $\text{Si}_2\text{O}_6\text{H}_6$, (c) $\text{Si}_5\text{O}_{15}\text{H}_{12}$, and (d) $\text{Si}_8\text{O}_{24}\text{H}_{18}$.

density, we can approximately derive ELF, introduced by Becke and Edgecombe [37]. The ELF pictures are shown in Figure 4. For the singlet state of the clusters, the ELF was, respectively, computed using the DFT/B3LYP, at the stable geometry of the singlet state. The nature of bonding between Si-Si atoms and charge transfer process is shown in the ELF. The transition can be depicted as an excitation from the top valence band to the ODC(I) defect level in the gap. The excited electron of the ODC(I) defect is located mainly on the central silicon atom. Figures 4(e)–4(h) show the wave function of HOMO. The excited electron transfer in the ODC(I) defect can be found in here too.

Table 2 and Figure 5 show the optical properties calculated from four clusters with ODC(I) defects by TDDFT-B3LYP, neglecting other paramagnetic defects. The singlet-to-singlet ($s_0 \rightarrow s_1$) excitation energy of Si_2H_6 cluster was calculated to be 7.39 eV, which agrees well with the previously reported excitation energies (~7.6 eV) [36, 38]. On the other hand, the calculated $s_0 \rightarrow s_1$ excitation energy of $\text{Si}_2\text{O}_6\text{H}_6$, $\text{Si}_5\text{O}_{15}\text{H}_{12}$, and $\text{Si}_8\text{O}_{24}\text{H}_{18}$ clusters was 6.87~7.04 eV. These excitation energy values are only slightly smaller than the experimental $s_0 \rightarrow s_1$ transition energy (~7.6 eV), because the basis sets (def2-TZVP) may not be flexible for highly energy. Analyzing these data, the nature of the 7.6 eV absorption band

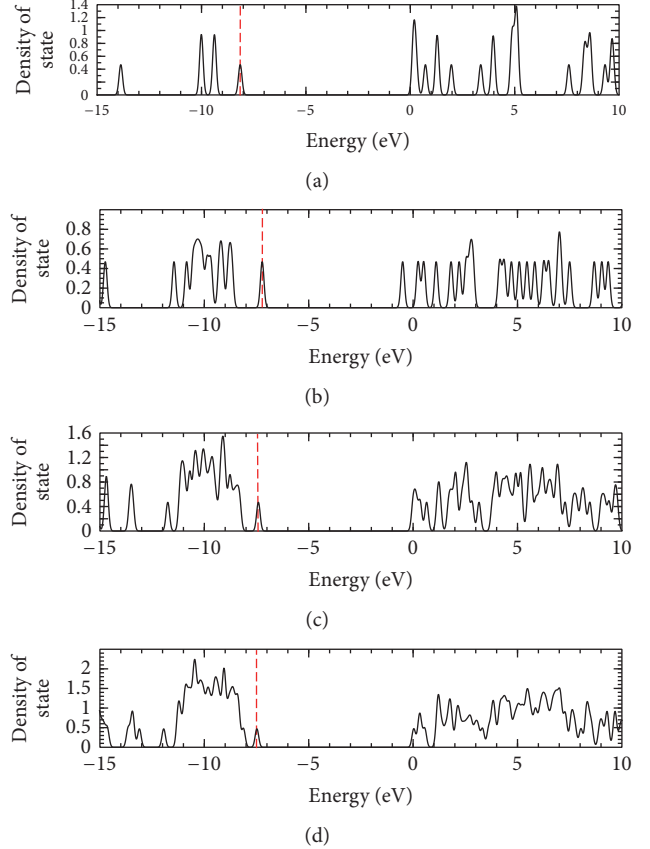


FIGURE 3: Total density of states (TDOS) of four clusters with ODC(I) defect. (a) Si_2H_6 , (b) $\text{Si}_2\text{O}_6\text{H}_6$, (c) $\text{Si}_5\text{O}_{15}\text{H}_{12}$, and (d) $\text{Si}_8\text{O}_{24}\text{H}_{18}$. The red vertical dashed lines align to highlight highest occupied molecular orbital (HOMO) level.

cannot be ascribed to a single point defect in α -quartz with ODC(I) defects. It can be explained as a manifestation of the localized states of the disordered structure of silica modified by an oxygen deficit.

3.3. Electronic Structure Properties and Optical Properties of ODC(II). The ODC(II) defect has been the subject of considerable interest since the discovery of the photorefractive effect in SiO_2 , and consequently, their microscopic structure and optical properties have been extensively studied using the cluster approach. Figure 6 shows the DOS of the α -quartz cluster models with ODC(II) defects computed by DFT-B3LYP. We calculate the total electronic DOS for SiO_2H_2 and $\text{Si}_3\text{O}_8\text{H}_6$ clusters (see Figures 1(e) and 1(f)), so that we can explore the geometric effect on the electronic structure. On the whole, the electronic DOS of the cluster shows remarkable structural sensitivity. We note that the details of the electronic structure are essentially dependent on the α -quartz cluster size and shape. Such structural dependence of electronic state will result in different excitation energy when these valence band states participate in optical transition of point defects.

To further illustrate the electronic structure of cluster with ODC(II) defect, we also present the electron localization

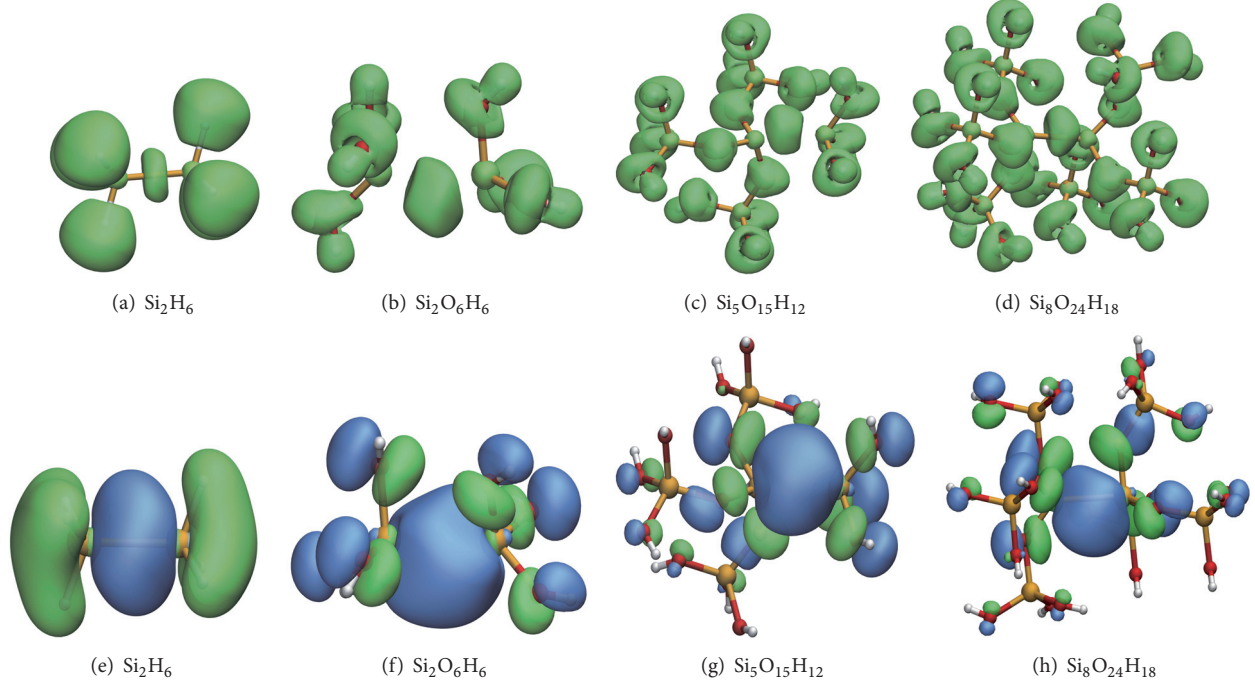


FIGURE 4: (a)–(d) ELF of the Si-Si band in α -quartz cluster configurations with ODC(I); (e)–(h) orbital wave function of HOMO in α -quartz cluster configurations with ODC(I). Green and blue color represent positive and negative phase of the orbital wave function, respectively.

TABLE 2: Summary of computed $s_0 \rightarrow s_1$ transition energy of the cluster configurations with ODC(I) defects, neglecting other paramagnetic defects.

| Cluster size | Transition energy (eV) | Oscillator strength f | Reference value (eV) |
|---|------------------------|----------------------------|----------------------|
| Si_2H_6 | 7.39 | 0.03 | 8.66 ^a |
| $\text{Si}_2\text{O}_6\text{H}_6$ | 6.87 | 0.44 | 7.47 ^a |
| $\text{Si}_5\text{O}_{15}\text{H}_{12}$ | 7.04 | 0.15 | 7.60 ^b |
| $\text{Si}_8\text{O}_{24}\text{H}_{18}$ | 6.88 | 0.09 | |

^aReference [27]. ^bReference [29].

function (ELF) (see Figures 7(a) and 7(b)) and the wave function (see Figures 7(c) and 7(d)) of HOMO on the two clusters. In order to research the charge distribution around ODC(II) defect, we plotted the ELF. For the singlet state of the clusters, the ELF was, respectively, computed using the DFT/B3LYP. The nature of divalent Si and charge transition process can be obtained in the ELF picture. The transition can be described as the lowest singlet excited state corresponding to a single electron promotion from the Si lone pair sp orbital to a vacant p_{π} orbital on the same atom. The excited electron of the ODC(II) defect is located mainly on the central silicon atom. The wave function of HOMO is shown in Figures 7(c) and 7(d). The excited electron transfer in the ODC(II) defect can also be found.

Table 3 shows the optical properties calculated from two clusters with ODC(II) defects by TDDFT-B3LYP, neglecting other paramagnetic defects. $s_0 \rightarrow s_1$ transition energies of the SiO_2 with ODC(II) defects were calculated by Trukhin [10], Lü et al. [8], and Adelstein et al. [7] using different cluster models and different levels of theory. These studies yield

almost the same calculated results concerning $s_0 \rightarrow s_1$. In our work, the $s_0 \rightarrow s_1$ transition energies of Si_2H_6 and $\text{Si}_3\text{O}_8\text{H}_6$ clusters are, respectively, calculated to be 5.47 eV and 5.20 eV, which agree well with the previously reported excitation energies. Analyzing these data, the nature of the 5.0 eV absorption band can be ascribed to a single electron promotion from the Si lone pair sp orbital to a vacant p_{π} orbital on the same atom.

3.4. Photoinduced Interconversions of ODC Defects in α -Quartz. A theoretical study of the interconversion models of amorphous silicon dioxide has been performed by Uchino et al. [39] who proposed a mechanism for the ODC(I) \rightarrow ODC(II) transformation based on photoionization of ODC(I). However, a detailed mechanism of this interconversion in α -quartz is unknown. To get better knowledge about the detailed photoinduced interconversion mechanism of ODC defects in α -quartz, we here employ quantum-chemical program (ORCA) using $\text{Si}_5\text{O}_{15}\text{H}_{12}$ cluster model.

Starting from the ground state geometry of $\text{Si}_5\text{O}_{15}\text{H}_{12}$ cluster model with ODC(I) (see Figure 1(c)), we have excited

TABLE 3: Summary of computed $s_0 \rightarrow s_1$ transition energy for the ODC(II) defects cluster configurations, neglecting other paramagnetic defects.

| Cluster size | Transition energy (eV) | Oscillator strength f | Reference value (eV) | Experiment (eV) |
|-----------------------------------|------------------------|-------------------------|---------------------------------------|------------------|
| Si_2H_6 | 5.47 | 0.17 | 5.50 ^a , 5.60 ^b | 5.0 ^d |
| $\text{Si}_3\text{O}_8\text{H}_6$ | 5.20 | 0.14 | 5.17 ^c , 5.30 ^b | |

^aReference [24]. ^bReferences [8, 28]. ^cReference[27]. ^dReference [6].

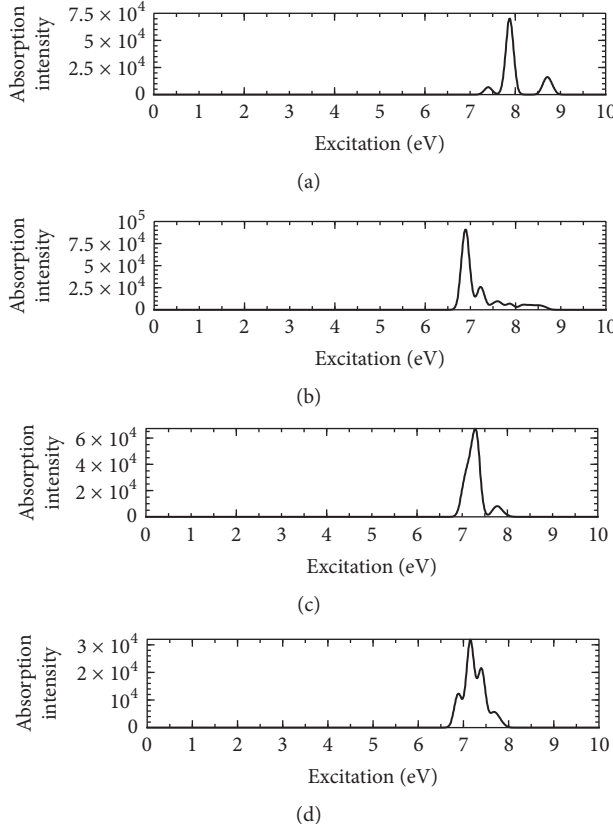


FIGURE 5: The OA spectra of four clusters calculated by TDDFT, which have ODC(I) defects. Gaussian broadening of 0.5 eV is used. (a) Si_2H_6 , (b) $\text{Si}_2\text{O}_6\text{H}_6$, (c) $\text{Si}_5\text{O}_{15}\text{H}_{12}$, and (d) $\text{Si}_8\text{O}_{24}\text{H}_{18}$.

the model into the triplet (T_1) state which is 4.11 eV higher in single point energy [31]. The cluster model relaxes under the modified potential energy surface, the Si-Si disconnects and expands up to 3.02 Å (see Figure 8(a)), which is slightly longer than the equilibrium bond length (2.53 Å) calculated for Figure 1(c), thus inducing a large distortion surrounding the defect. Following the reaction path toward the ODC(II) (see Figure 8(c)), we find the transition state (see Figure 8(b)) and the computed relaxation energy is 0.46 eV higher than the T_1 state of $\text{Si}_5\text{O}_{15}\text{H}_{12}$ cluster model with ODC(I). The transition state cannot be stable.

By further decreasing the reaction coordinate, $\text{Si}_5\text{O}_{15}\text{H}_{12}$ cluster transforms spontaneously into the ODC(II) configuration and the computed relaxation energy is 0.30 eV lower than the transition state of $\text{Si}_5\text{O}_{15}\text{H}_{12}$ cluster model. This implies that the transition state configuration corresponds to

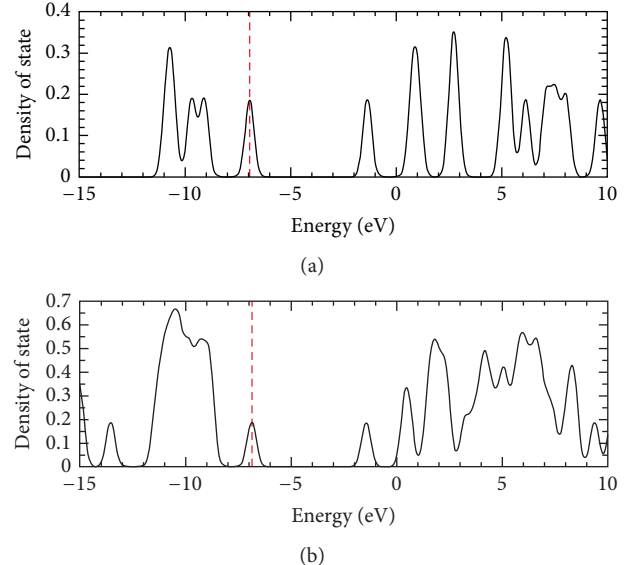


FIGURE 6: Total density of states (TDOS) of two clusters with ODC(II) defect. (a) SiO_2H_2 ; (b) $\text{Si}_3\text{O}_8\text{H}_6$. The red vertical dashed lines align to highlight highest occupied molecular orbital (HOMO) level.

a metastable minimum and is possible to relax into a lower energy configuration shown in Figure 8(c) during thermal processes. Among the many possible local configurations of the ODC(I) defect in α -quartz, only a small fraction is expected to transform into the ODC(II) upon excitation. Although our used cluster model is small, other local configurations different from ours may be more favorable for the interconversion.

4. Conclusions

The DFT method was employed to study the structures of six different cluster models for α -quartz with ODCs defects. We predict the apposite Si-Si band length in order to search for the stable structure of cluster models with ODC(I) defects. For $\text{Si}_2\text{O}_6\text{H}_6$, $\text{Si}_5\text{O}_{15}\text{H}_{12}$, and $\text{Si}_8\text{O}_{24}\text{H}_{18}$ cluster models with ODC(I) defect, with the increasing of cluster size and shape, the equilibrium Si-Si bond length decreases. The OA spectroscopic properties and excitation energies are calculated based on TDDFT. For clusters with ODC(I), the nature of the 7.6 eV absorption band can be explained as a manifestation of the localized states of the disordered structure of silica modified by an oxygen deficit. However, for clusters with ODC(II), the nature of the 5.0 eV absorption band can be

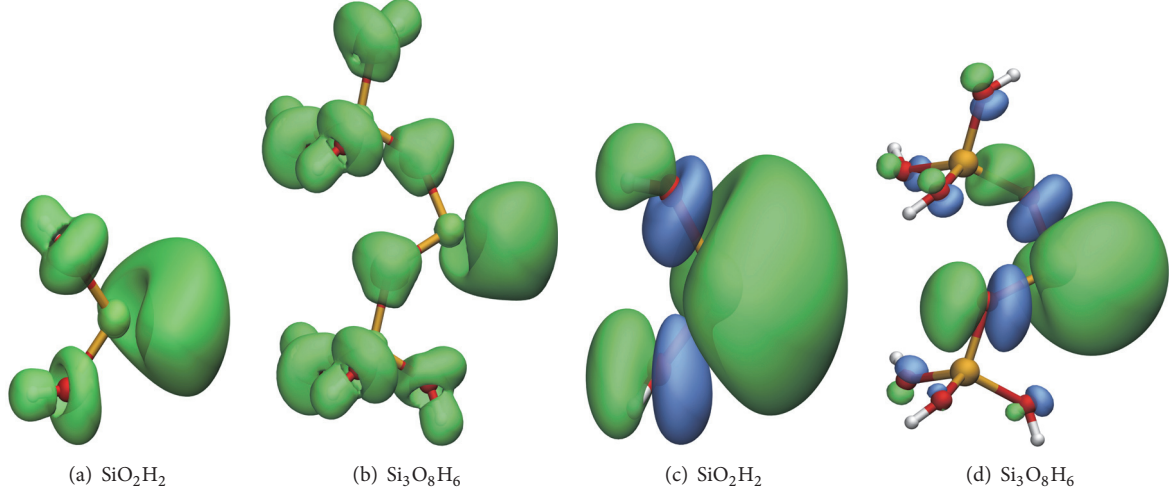


FIGURE 7: (a)-(b) ELF of the divalent Si in α -quartz cluster configurations with ODC(II). (c)-(d) Orbital wave function of HOMO in α -quartz cluster configurations with ODC(II). Green and blue color represent positive and negative phase of the orbital wave function, respectively.

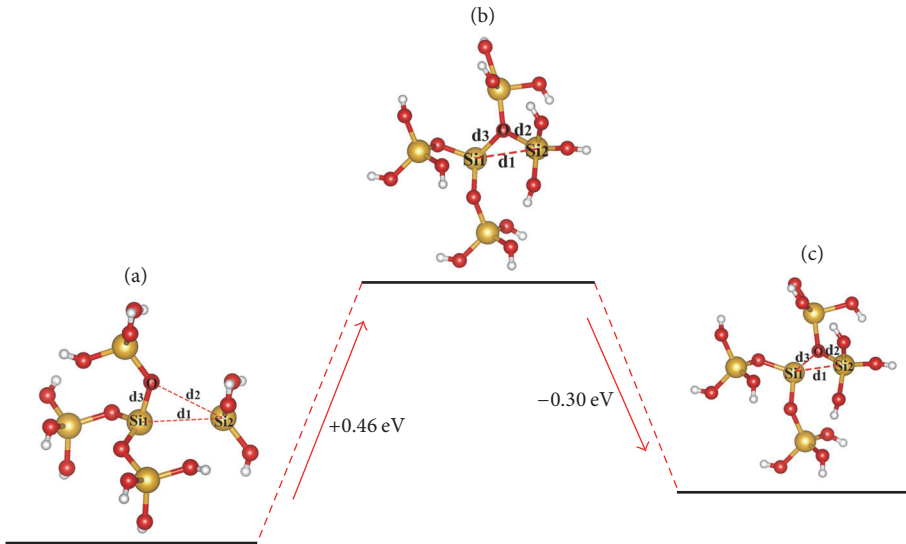


FIGURE 8: Schematic illustration of the proposed interconversion mechanism from ODC(I) defect into ODC(II) defect in the lowest triplet (T_1) excited state. The red arrows stand for transformation of preexisting point defects and recombinations. (a) Optimized geometry of the $\text{Si}_5\text{O}_{15}\text{H}_{12}$ cluster with ODC(I), $d_1 = 3.02 \text{ \AA}$, $d_2 = 3.05 \text{ \AA}$, and $d_3 = 1.65 \text{ \AA}$. (b) The transition state geometry of the $\text{Si}_5\text{O}_{15}\text{H}_{12}$ cluster, $d_1 = 3.13 \text{ \AA}$, $d_2 = 1.86 \text{ \AA}$, and $d_3 = 1.80 \text{ \AA}$. (c) Optimized geometry of the $\text{Si}_5\text{O}_{15}\text{H}_{12}$ cluster with ODC(II), $d_1 = 3.07 \text{ \AA}$, $d_2 = 1.64 \text{ \AA}$, and $d_3 = 1.91 \text{ \AA}$.

ascribed to a single electron promotion from the Si lone pair sp orbital to a vacant p_{π} orbital on the same atom. We also study the detailed photoinduced interconversion mechanism of ODCs defects in α -quartz. We predicted the existence of a metastable structure of ODC(I) for the first time. Our results provide strong theoretical support to the viability of the processes.

Conflicts of Interest

There are no conflicts of interest related to this paper.

Acknowledgments

This work is supported by the National Natural Science Foundation of China (nos. 61377097, 61675032, and 61671085), the National Basic Research Program of China (973 Program) under Grant no. 2014CB643900, the Open Program of State Key Laboratory of Functional Materials for Informatics, National Natural Science Foundation for Theoretical Physics Special Fund “Cooperation Program” (no. 11547039), Shaanxi Institute of Scientific Research Plan Projects (no. SLGKYQD2-05), and the Fund of State Key Laboratory

of Information Photonics and Optical Communications (BUPT) (no. IPOC2015ZT05). The authors acknowledge the computational support from the Beijing Computational Science Research Center (CSRC).

References

- [1] A. N. Trukhin, K. Smits, J. Jansons, and A. Kuzmin, "Luminescence of polymorphous SiO₂," *Radiation Measurements*, 2015.
- [2] S. Basu, "Defect related luminescence in silicon dioxide network: a review," *Crystalline Silicon-Properties and Uses: InTech*, 2011.
- [3] M. Liu, P.-F. Lu, Y. Yang, L.-Y. Wu, R. Su, and J. Chen, "Structural and Optical Properties of Point Defects in α -SiO₂ Cluster," *Communications in Theoretical Physics*, vol. 64, no. 2, pp. 244–248, 2015.
- [4] L. Skuja, "Optically active oxygen-deficiency-related centers in amorphous silicon dioxide," *Journal of Non-Crystalline Solids*, vol. 239, no. 1–3, pp. 16–48, 1998.
- [5] R. Saavedra, D. Jiménez-Rey, P. Martin, and R. Vila, "Ionoluminescence of fused silica under swift ion irradiation," *Nuclear Instruments and Methods in Physics Research Section B: Beam Interactions with Materials and Atoms*, vol. 382, pp. 96–100, 2016.
- [6] A. N. Trukhin, "Radiation processes in oxygen-deficient silica glasses: Is ODC(I) a precursor of E¹-center?" *Journal of Non-Crystalline Solids*, vol. 352, no. 28–29, pp. 3002–3008, 2006.
- [7] N. Adelstein, D. Lee, J. L. DuBois, and V. Lordi, *Magnetic fluctuation from oxygen deficiency centers on the SiO₂ surface*, 2014, <https://arxiv.org/abs/1403.0685>.
- [8] H.-B. Lü, S.-Z. Xu, H.-J. Wang, X.-D. Yuan, C. Zhao, and Y. Q. Fu, "Evolution of oxygen deficiency center on fused silica surface irradiated by ultraviolet laser and posttreatment," *Advances in Condensed Matter Physics*, vol. 2014, Article ID 769059, 2014.
- [9] M. L. Crespillo, J. T. Graham, Y. Zhang, and W. J. Weber, "In-situ luminescence monitoring of ion-induced damage evolution in SiO₂ and Al₂O₃," *Journal of Luminescence*, vol. 172, pp. 208–218, 2016.
- [10] A. N. Trukhin, "Luminescence of localized states in silicon dioxide glass. A short review," *Journal of Non-Crystalline Solids*, vol. 357, no. 8–9, pp. 1931–1940, 2011.
- [11] H. Imai, K. Arai, H. Imagawa, H. Hosono, and Y. Abe, "Two types of oxygen-deficient centers in synthetic silica glass," *Physical Review B: Condensed Matter and Materials Physics*, vol. 38, no. 17, pp. 12772–12775, 1988.
- [12] N. L. Anderson, R. P. Vedula, P. A. Schultz, R. M. Van Ginhoven, and A. Strachan, "First-principles investigation of low energy E¹ center precursors in amorphous silica," *Physical Review Letters*, vol. 106, no. 20, Article ID 206402, 2011.
- [13] N. L. Anderson, R. Pramod Vedula, P. A. Schultz, R. M. V. Ginhoven, and A. Strachan, "Defect level distributions and atomic relaxations induced by charge trapping in amorphous silica," *Applied Physics Letters*, vol. 100, no. 17, Article ID 172908, 2012.
- [14] D. L. Griscom, "Trapped-electron centers in pure and doped glassy silica: A review and synthesis," *Journal of Non-Crystalline Solids*, vol. 357, no. 8–9, pp. 1945–1962, 2011.
- [15] K. Awazu, H. Kawazoe, and K.-I. Muta, "Optical properties of oxygen-deficient centers in silica glasses fabricated in H₂ or vacuum ambient," *Journal of Applied Physics*, vol. 70, no. 1, pp. 69–74, 1991.
- [16] A. R. Silin and L. N. Skuja, "Intrinsic defects in fused silica," *Journal of Non-Crystalline Solids*, vol. 71, no. 1–3, pp. 443–445, 1985.
- [17] L. Skuja, "Isoelectronic series of twofold coordinated Si, Ge, and Sn atoms in glassy SiO₂: a luminescence study," *Journal of Non-Crystalline Solids*, vol. 149, no. 1–2, pp. 77–95, 1992.
- [18] G. Pacchioni and R. Ferrario, "Optical transitions and EPR properties of two-coordinated Si, Ge, Sn and related H(I), H(II), and H (III) centers in pure and doped silica from ab initio calculations," *Physical Review B: Condensed Matter and Materials Physics*, vol. 58, no. 10, pp. 6090–6096, 1998.
- [19] B. B. Stefanov and K. Raghavachari, "Cluster models for the photoabsorption of divalent defects in silicate glasses: Basis set and cluster size dependence," *Applied Physics Letters*, vol. 71, no. 6, pp. 770–772, 1997.
- [20] B. L. Zhang and K. Raghavachari, "Photoabsorption and photoluminescence of divalent defects in silicate and germanosilicate glasses: First-principles calculations," *Physical Review B: Condensed Matter and Materials Physics*, vol. 55, no. 24, pp. R15993–R15996, 1997.
- [21] M. Boero, A. Pasquarello, J. Sarnthein, and R. Car, "Structure and hyperfine parameters of E¹/I centers in α -quartz and in vitreous SiO₂," *Physical Review Letters*, vol. 78, no. 5, pp. 887–890, 1997.
- [22] K. C. Snyder and W. B. Fowler, "Oxygen vacancy in α -quartz: A possible bi- and metastable defect," *Physical Review B: Condensed Matter and Materials Physics*, vol. 48, no. 18, pp. 13238–13243, 1993.
- [23] H. Hosono, H. Kawazoe, and N. Matsunami, "Experimental evidence for Frenkel defect formation in amorphous SiO₂ by electronic excitation," *Physical Review Letters*, vol. 80, no. 2, pp. 317–320, 1998.
- [24] K. Kajihara, M. Hirano, L. Skuja, and H. Hosono, "Formation of intrinsic point defects in fluorine-doped synthetic SiO₂ glass by ^{60}Co γ -ray irradiation," *Chemistry Letters*, vol. 36, no. 2, pp. 266–267, 2007.
- [25] K. Kajihara, M. Hirano, L. Skuja, and H. Hosono, "Intrinsic defect formation in amorphous SiO₂ by electronic excitation: Bond dissociation versus Frenkel mechanisms," *Physical Review B: Condensed Matter and Materials Physics*, vol. 78, no. 9, Article ID 094201, 2008.
- [26] L. Skuja, B. Gütter, D. Schiel, and A. R. Silin, "Infrared photoluminescence of preexisting or irradiation-induced interstitial oxygen molecules in glassy SiO₂ and α -quartz," *Physical Review B: Condensed Matter and Materials Physics*, vol. 58, no. 21, pp. 14296–14304, 1998.
- [27] M. A. Stevens-Kalceff, "Electron-Irradiation-Induced Radiolytic Oxygen Generation and Microsegregation in Silicon Dioxide Polymorphs," *Physical Review Letters*, vol. 84, no. 14, pp. 3137–3140, 2000.
- [28] T. E. Tsai and D. L. Griscom, "Experimental evidence for excitonic mechanism of defect generation in high-purity silica," *Physical Review Letters*, vol. 67, no. 18, pp. 2517–2520, 1991.
- [29] K. Kajihara, L. Skuja, and H. Hosono, "Formation and annihilation of intrinsic defects induced by electronic excitation in high-purity crystalline SiO₂," *Journal of Applied Physics*, vol. 113, no. 14, Article ID 143511, 2013.
- [30] G. Pacchioni and G. Ieraño, *Physical Review B: Condensed Matter and Materials Physics*, vol. 57, no. 2, pp. 818–832, 1998.
- [31] B. B. Stefanov and K. Raghavachari, "Photoabsorption of the neutral oxygen vacancy in silicate and germanosilicate glasses:

- First-principles calculations,” *Physical Review B: Condensed Matter and Materials Physics*, vol. 56, no. 9, pp. 5035–5038, 1997.
- [32] A. D. Becke, “Density-functional thermochemistry. III. The role of exact exchange,” *The Journal of Chemical Physics*, vol. 98, no. 7, pp. 5648–5652, 1993.
 - [33] C. Lee, W. Yang, and R. G. Parr, “Development of the Colle-Salvetti correlation-energy formula into a functional of the electron density” *Physical Review B: Condensed Matter and Materials Physics*, vol. 37, no. 2, pp. 785–789, 1988.
 - [34] A. Schäfer, C. Huber, and R. Ahlrichs, “Fully optimized contracted Gaussian basis sets of triple zeta valence quality for atoms Li to Kr,” *The Journal of Chemical Physics*, vol. 100, no. 8, pp. 5829–5835, 1994.
 - [35] P. Pulay, “Convergence acceleration of iterative sequences. the case of scf iteration,” *Chemical Physics Letters*, vol. 73, no. 2, pp. 393–398, 1980.
 - [36] P. Pulay, “Improved SCF convergence acceleration,” *Journal of Computational Chemistry*, vol. 3, no. 4, pp. 556–560, 1982.
 - [37] A. D. Becke and K. E. Edgecombe, “A simple measure of electron localization in atomic and molecular systems,” *The Journal of Chemical Physics*, vol. 92, no. 9, pp. 5397–5403, 1990.
 - [38] G. Pacchioni and G. Ieranò, “Computed optical absorption and photoluminescence spectra of neutral oxygen vacancies in α -quartz,” *Physical Review Letters*, vol. 79, no. 4, pp. 753–756, 1997.
 - [39] T. Uchino, M. Takahashi, and T. Yoko, “Mechanism of interconversion among radiation-induced defects in amorphous silicon dioxide,” *Physical Review Letters*, vol. 86, no. 9, pp. 1777–1780, 2001.

Research Article

First-Principles Calculations on Atomic and Electronic Properties of Ge/4H-SiC Heterojunction

Bei Xu,¹ Changjun Zhu,¹ Xiaomin He,² Yuan Zang,² Shenghuang Lin,³
Lianbi Li ,¹ Song Feng ,¹ and Qianqian Lei¹

¹School of Science, Xi'an Polytechnic University, Xi'an 710048, China

²Department of Electronic Engineering, Xi'an University of Technology, Xi'an 710048, China

³Department of Applied Physics, The Hong Kong Polytechnic University, Hung Hom, Hong Kong

Correspondence should be addressed to Lianbi Li; xpu_lilianbi@163.com

Received 26 October 2017; Revised 16 January 2018; Accepted 10 February 2018; Published 20 March 2018

Academic Editor: Mohindar S. Seehra

Copyright © 2018 Bei Xu et al. This is an open access article distributed under the Creative Commons Attribution License, which permits unrestricted use, distribution, and reproduction in any medium, provided the original work is properly cited.

First-principles calculation is employed to investigate atomic and electronic properties of Ge/SiC heterojunction with different Ge orientations. Based on the density functional theory, the work of adhesion, relaxation energy, density of states, and total charge density are calculated. It is shown that Ge(110)/4H-SiC(0001) heterointerface possesses higher adhesion energy than that of Ge(111)/4H-SiC(0001) interface, and hence Ge/4H-SiC(0001) heterojunction with Ge[110] crystalline orientation exhibits more stable characteristics. The relaxation energy of Ge(110)/4H-SiC(0001) heterojunction interface is lower than that of Ge(111)/4H-SiC(0001) interface, indicating that Ge(110)/4H-SiC(0001) interface is easier to form at relative low temperature. The interfacial bonding is analysed using partial density of states and total charge density distribution, and the results show that the bonding is contributed by the Ge-Si bonding.

1. Introduction

SiC semiconductor has become one of the most excellent materials for ultraviolet-sensitive devices owing to its wide bandgap [1, 2]. However, it is not sensitive to the infrared and visible light region. Ge/SiC heterojunction was employed to solve the problem, in which the Ge layer of micro-nanostructure was used as an absorption layer for near-infrared (NIR) light [3]. By using the Ge/SiC heterojunction, SiC-based NIR light-operated device could be realized. The Ge/4H-SiC heterostructures are prepared by using low pressure chemical vapor deposition (LPCVD) on 4H-SiC(0001) substrates. Details of the growth process could be found in [4–6]. However, the lattice mismatch between Ge(111) primitive cell ($a_{\text{Ge}(111)} = 4.000 \text{ \AA}$) and 4H-SiC(0001) primitive cell ($a_{\text{4H-SiC}(0001)} = 3.078 \text{ \AA}$) is as large as 23.0%, which can cause distortion or even dislocation near the interface, leading to a poor crystalline quality of the Ge epilayer. Hence, it is necessary and imperative to investigate the atomic and electronic properties of the Ge/SiC heterojunction.

First-principles calculation based on density functional theory (DFT) has been widely used as an important microscopic study method in recent years. The first-principles calculation can be implemented to predict material properties and, consequently, a lot of valuable results have been achieved. Li et al. [7] used the first-principles method to investigate the interface adhesion energy, interface energy, interface fracture toughness, and electronic structure of the $\beta\text{-SiC}(111)/\alpha\text{-Ti}(0001)$ heterojunction. Six kinds of C-terminated $\beta\text{-SiC}(111)/\alpha\text{-Ti}(0001)$ models were established to study the effect of stack position and inclination angle on interface bonding and fracture toughness. Lin et al. [8] investigated the atomic structures and electronic properties of interfaces between aluminum and four kinds of ceramics with different orientations. They discovered that aluminum metal carbide interface is more stable than aluminum metal nitrides interface and, moreover, the (111) interfaces were found to possess the largest adhesion energy. He et al. [9, 10] studied the $\text{Si}(111)/6\text{H-SiC}(0001)$ heterojunction by using the first-principles. It is found that

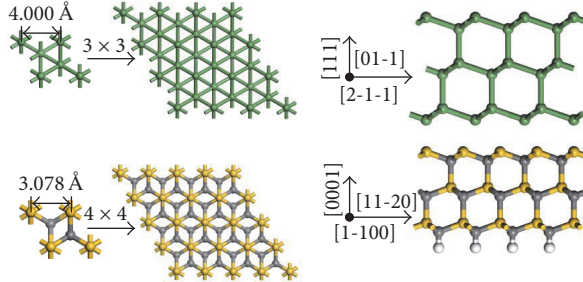


FIGURE 1: A schematic of Ge(111)/4H-SiC(0001) heterointerface model.

the Si-terminated Si(111)/6H-SiC(0001) heterojunction has higher adhesion energy and lower relaxation degree than C-terminated Si(111)/6H-SiC(0001) heterojunction. Xu et al. [11] have studied interfacial properties and electronic structure of Al(111)/4H-SiC(0001) interface.

In this paper, we present first-principles calculations of adhesion energy, relaxation energy, density of states, and total charge density of Ge(111)/4H-SiC(0001) interface and Ge(110)/4H-SiC(0001) interface, while analysing the electronic structure, geometry property, and the corresponding physical picture. Furthermore, the first-principles methods are used to investigate the structure of Ge/SiC heterointerface, which can provide a theoretical basis for the growth of Ge/SiC heterojunctions in experiment.

2. Methods

All the calculations in this work were implemented by using the Cambridge Serial Total Energy Package (CASTEP) Code [12, 13], which are based on the density functional theory (DFT) [14]. Generalized gradient approximation (GGA) of Perdew–Burke–Ernzerhof (PBE) scheme was employed to describe the exchange-correlation functional [15]. By comparing the lattice constants of GGA(PBE) and local density approximation (LDA) [16] with Ceperley–Alder Perdew–Zunger (CA-PZ) approximation algorithms, it is shown that the deviation of GGA(PBE) is smaller than that of LDA(CA-PZ). Therefore, the GGA-PBE function is implemented in the following Ge/4H-SiC(0001) heterojunction calculation. In order to make the system stable and the calculation speed optimal, plane wave cut-off energy was selected as 550 eV for a bulk, a surface, and an interface. The sampling of irreducible edge of Brillouin zone was performed with a regular Monkhorst-Pack grid with $7 \times 7 \times 7$ k points for the bulk and $5 \times 5 \times 1$ k points for the surface and interface, respectively. The SCF convergence threshold was 2.0×10^{-6} eV/atom, and the convergence tolerance for energy was selected as 2.0×10^{-5} eV/atom. The force tolerance, stress, and displacement tolerance were set as 0.05 eV/Å, 0.1 GPa, and 0.002 Å, respectively. To avoid interaction between surface atoms, a vacuum layer of 13 Å was selected for each surface and interface system.

3. Results and Discussions

3.1. Ge/4H-SiC Heterojunction Model. Figure 1 displays the interface structure of the Ge(111)/4H-SiC(0001) heterojunction based on the TEM characterizations [3]. The primitive cells of Ge(111) surface and 4H-SiC(0001) surface possess lattice constants of $[01-1]_{\text{Ge}} = 4.000 \text{ \AA}$, $[11-20]_{\text{SiC}} = 3.078 \text{ \AA}$. The lattice matching is 3:4 of Ge to SiC with a residual mismatch of 2.60% in the two parallel orientations using the smallest supercell mismatch. In order to saturate suspension bonding, H atoms are employed to passivate the surface. Figure 2 shows the Ge(110)/4H-SiC(0001) heterojunction. The primitive cells of Ge(110) surface and 4H-SiC(0001) surface with constants lattice of $[001]_{\text{Ge}} = 5.658 \text{ \AA}$, $[1-10]_{\text{Ge}} = 4.000 \text{ \AA}$, $[10-10]_{\text{SiC}} = 5.331 \text{ \AA}$, and $[-12-10]_{\text{SiC}} = 3.078 \text{ \AA}$ are cleaved due to the Ge[110] growth orientation on 4H-SiC(0001). The lattice matching is revealed as 1:1 Ge to SiC with a residual mismatch of -5.78% and 3:4 Ge to SiC with a lattice mismatch of 2.60% in the two parallel orientations. The interlayer distances of Ge(111)/4H-SiC(0001) interface and Ge(110)/4H-SiC(0001) interface are optimized by energy calculation before evaluating the interfacial properties of heterostructures. The functional relationship between energy and interlayer spacing is shown in Figure 3. Both of the Ge(111)/4H-SiC(0001) and Ge(110)/4H-SiC(0001) heterostructures have the same optimized interlayer distances of 2.30 Å. Similar conclusions are given in [17].

Because of the large lattice mismatch strain, the lattice mismatch between 4H-SiC and Ge is totally accommodated by misfit dislocations (MD) rather than by uniform elastic strains [1, 2]. The lattice mismatch of the Ge/4H-SiC interfaces can be calculated, as shown in Table 1. The Ge(111)/4H-SiC(0001) interface has the same 3:4 Ge-to-SiC matching mode with a residual mismatch of 2.60% along both the Ge[01-1] and Ge[2-1-1] orientations. In contrast, the situation of the Ge(110)/4H-SiC(0001) interface is different, along Ge[1-10] orientation, the Ge-to-SiC matching mode is still 3:4; along the vertical orientation of Ge[001], the Ge-to-SiC mode changes to 1:1 and the residual mismatch changes to -5.78% correspondingly. The MD densities of the Ge(111)/4H-SiC(0001) interface and Ge(110)/4H-SiC(0001) interface are as low as $5.334 \times 10^{14} \text{ cm}^{-2}$ and $1.523 \times 10^{14} \text{ cm}^{-2}$,

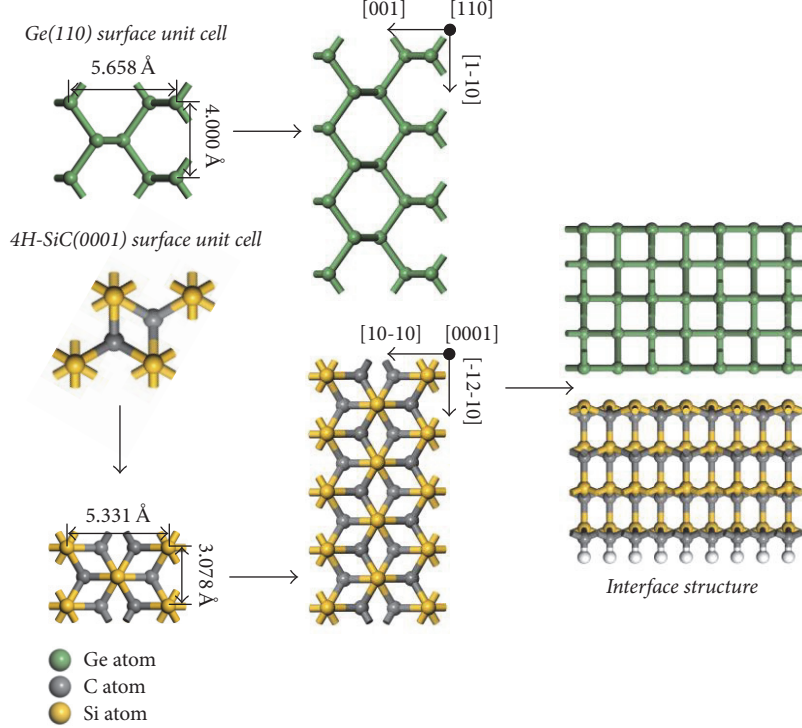


FIGURE 2: A schematic of Ge(110)/4H-SiC(0001) heterointerface model.

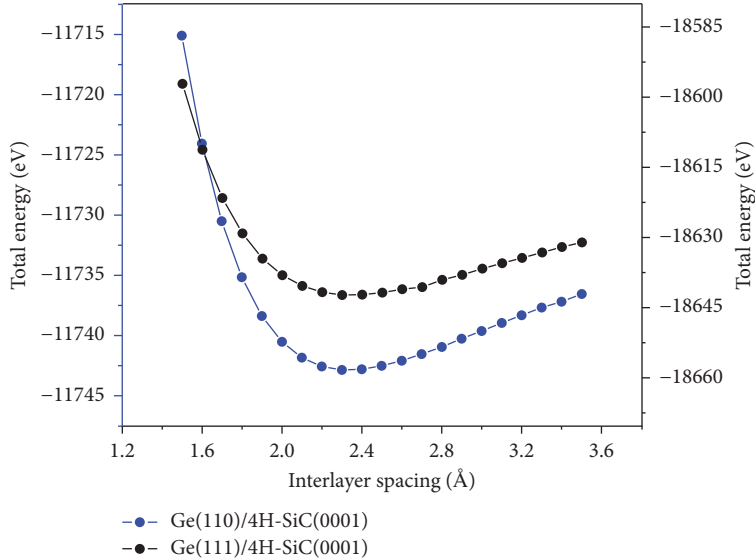


FIGURE 3: The interlayer spacing of Ge(110)/4H-SiC(0001) and Ge(111)/4H-SiC(0001) heterointerfaces.

respectively, as shown in Table 1. In addition, the Ge(110)/4H-SiC(0001) interface has fewer defects than the Ge(111)/4H-SiC(0001) interface.

3.2. Heterointerfaces Properties

3.2.1. Adhesion Energy and Relaxation Energy. To gain an insight into the binding strength of the interface, we calculated the work of adhesion (W_{ad}), which is defined as the

reversible work to separate an interface into two free surfaces given by the difference in total energy between the interface and its initial isolated slabs according to the following formula [18–20]:

$$W_{ad} = \frac{(E_{Ge} + E_{SiC} - E_{Ge/4H-SiC})}{(NA)}, \quad (1)$$

where E_{Ge} and E_{SiC} are the total energy of Ge slab and SiC slab, where one slab remained and the other is replaced by

TABLE 1: The lattice mismatch of the Ge/4H-SiC heterostructures calculated with the domain matching model.

| Growth orientation | Ge-to-SiC matching mode | | Residual mismatch | | MD density |
|----------------------|-------------------------|-------------|-------------------|-------------|--|
| Ge(111)/4H-SiC(0001) | Ge[01-1] | Ge[2-1-1] | Ge[01-1] | Ge[2-1-1] | $5.334 \times 10^{14} \text{ cm}^{-2}$ |
| | SiC[11-20] | SiC[1-100] | SiC[11-20] | SiC[1-100] | |
| | 3:4 | 3:4 | 2.60% | 2.60% | |
| Ge(110)/4H-SiC(0001) | Ge[001] | Ge[1-10] | Ge[001] | Ge[1-10] | $1.523 \times 10^{14} \text{ cm}^{-2}$ |
| | SiC[10-10] | SiC[-12-10] | SiC[10-10] | SiC[-12-10] | |
| | 1:1 | 3:4 | -5.78% | 2.60% | |

TABLE 2: Unrelaxed and relaxed E_{Ge} , $E_{\text{4H-SiC}(0001)}$, $E_{\text{Ge}/\text{4H-SiC}}$, and W_{ad} .

| | $E_{\text{Ge}(111)}$ (eV) | $E_{\text{4H-SiC}(0001)}$ (eV) | $E_{\text{Ge}(111)/\text{4H-SiC}(0001)}$ (eV) | W_{ad} (J/m ²) |
|-----------|---------------------------|--------------------------------|---|-------------------------------------|
| Unrelaxed | -5777.006 | -12844.091 | -18642.163 | 0.104 |
| Relaxed | -5777.551 | -12845.745 | -18644.926 | 0.106 |
| | $E_{\text{Ge}(110)}$ (eV) | $E_{\text{4H-SiC}(0001)}$ (eV) | $E_{\text{Ge}(110)/\text{4H-SiC}(0001)}$ (eV) | W_{ad} (J/m ²) |
| Unrelaxed | -3207.981 | -8523.457 | -11742.871 | 0.193 |
| Relaxed | -3208.026 | -8524.842 | -11746.039 | 0.222 |

TABLE 3: Relaxation energies of Ge(111)/4H-SiC(0001) and Ge(110)/4H-SiC(0001) interfaces.

| Heterojunction | E'_{total} (eV) | E_{total} (eV) | E_{relaxion} (eV/atom) |
|----------------------|--------------------------|-------------------------|---------------------------------|
| Ge(111)/4H-SiC(0001) | -18642.163 | -18644.926 | -0.017 |
| Ge(110)/4H-SiC(0001) | -11742.871 | -11746.039 | -0.030 |

vacuum in the same supercell, respectively. $E_{\text{Ge}/\text{4H-SiC}}$ denotes the total energy of the interface system, N is the number of atoms at the interface in the model, and A is the interfacial area. Based on (1), the variable values are obtained and listed in Table 2.

In addition, the relaxation energy E_{relaxion} can be determined by an expression as follows:

$$E_{\text{relaxion}} = \frac{(E_{\text{total}} - E'_{\text{total}})}{N}, \quad (2)$$

where E'_{total} and E_{total} are the total energies of the unrelaxed and relaxed interface systems, respectively, and N is the number of atoms in the system. Based on (2), the variable values are obtained and listed in Table 3.

Table 2 shows that the bonding energy of the unrelaxed interface is smaller than that of the relaxed one, indicating that the relaxed interface is more stable. It is also shown that the adhesion energy of Ge(110)/4H-SiC(0001) interface is higher than that of the Ge(111)/4H-SiC(0001) interface, indicating that Ge(110)/4H-SiC(0001) heterointerface is more energetically stable than Ge(111)/4H-SiC(0001) heterointerface. As shown in Table 3, the relaxation energy of Ge(110)/4H-SiC(0001) interface is lower than that of Ge(111)/4H-SiC(0001) interface, suggesting that Ge(110) films are easier to deposit on 4H-SiC(0001) substrates at relative low temperatures, which is consistent with the conclusions in [6].

The influence of relaxation on the atom positions at the Ge/4H-SiC interfaces is investigated. Figures 4(a) and 4(b) represent the atom-stacking structures of the post-optimized

Ge(110)/4H-SiC(0001) interface and Ge(111)/4H-SiC(0001) interface, respectively. It is shown that the position of atoms near the interface deviates from the original position to some extent, displaying certain displacements. To quantitatively compare the extent of relaxation between Ge(110)/4H-SiC(0001) and Ge(111)/4H-SiC(0001) interface, corresponding variations of XYZ coordinates and variations of distance were calculated, as shown in Figures 4(c)–4(j). The first and second layers of atoms at the interface severely deviate from the equilibrium position. Approaching to the bulk materials, the deviations decrease drastically, suggesting that, as the interface formed, merely one or two layers of atoms at the interface were significantly influenced. In the meantime, one can also observe that at the interface the variation of Ge atoms is larger than that of SiC atoms, indicating that the relaxation occurs mainly on the Ge side. It is shown that the variation of atoms in Figure 4(d) is larger than that in Figure 4(c), which is attributed to the fact that the lattice mismatch in the Y direction is greater than that in the X direction at the Ge(110)/4H-SiC(0001) interface. However, the variation of the atoms in Figure 4(g) is almost the same as that in Figure 4(h), since the lattice mismatch in the Y direction is commensurate to that in the X direction at the Ge(111)/4H-SiC(0001) interface.

3.2.2. Electronic Structure and Bonding. In order to understand the essence of bonds of Ge(111)/4H-SiC(0001) and Ge(110)/4H-SiC(0001) interfaces, the total charge density and charge density difference of Ge(111)/4H-SiC(0001) and Ge(110)/4H-SiC(0001) interfaces are calculated, as shown in Figures 5(a)–5(d), respectively. High charge accumulation

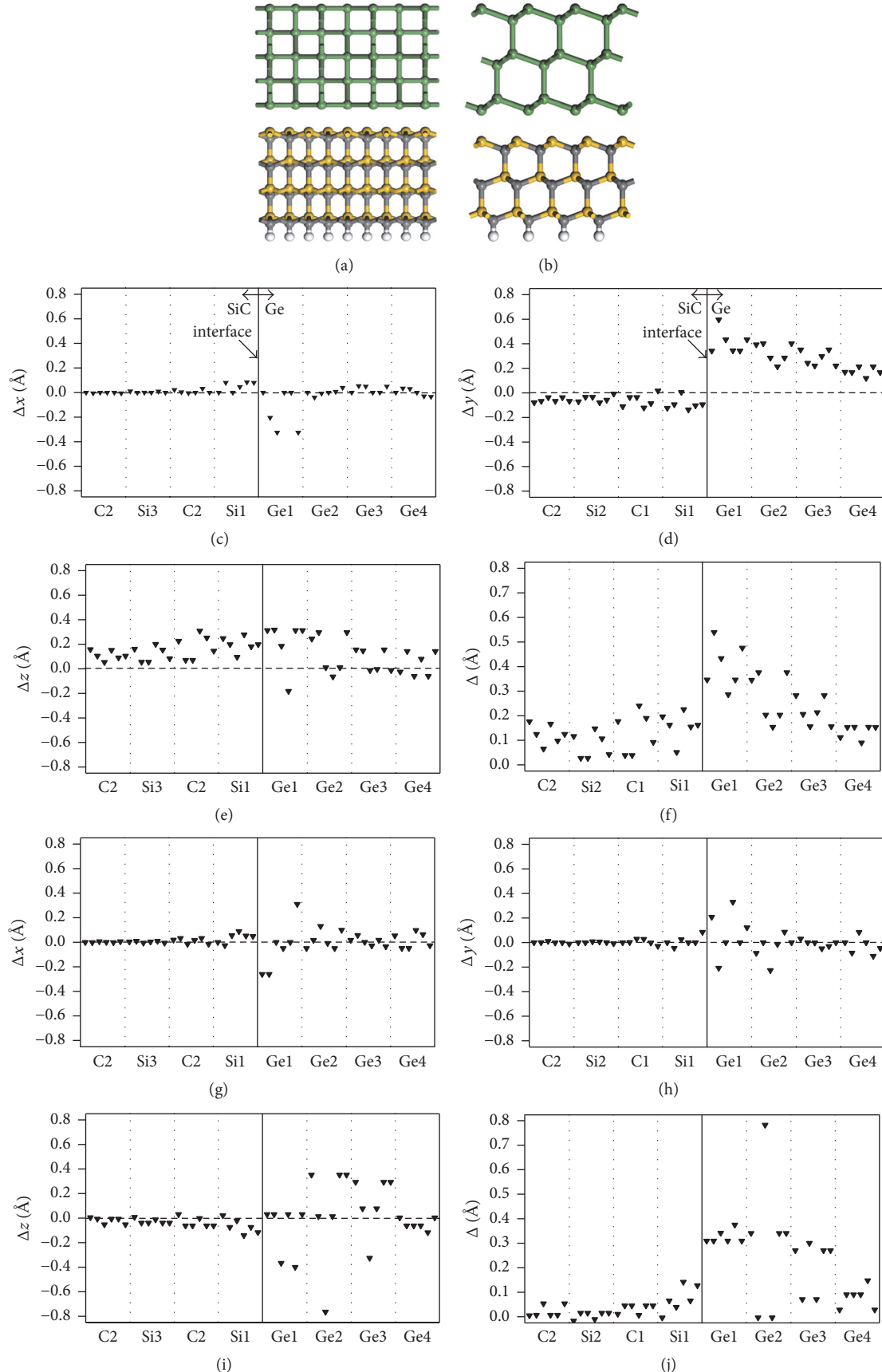


FIGURE 4: Ge(110)/4H-SiC(0001) heterointerface and variations of XYZ coordinates and variation of distance are shown in (a) and (c–f), respectively. Ge(111)/4H-SiC(0001) heterointerface and variations of XYZ coordinates and variation of distance are shown in (b) and (g–j), respectively.

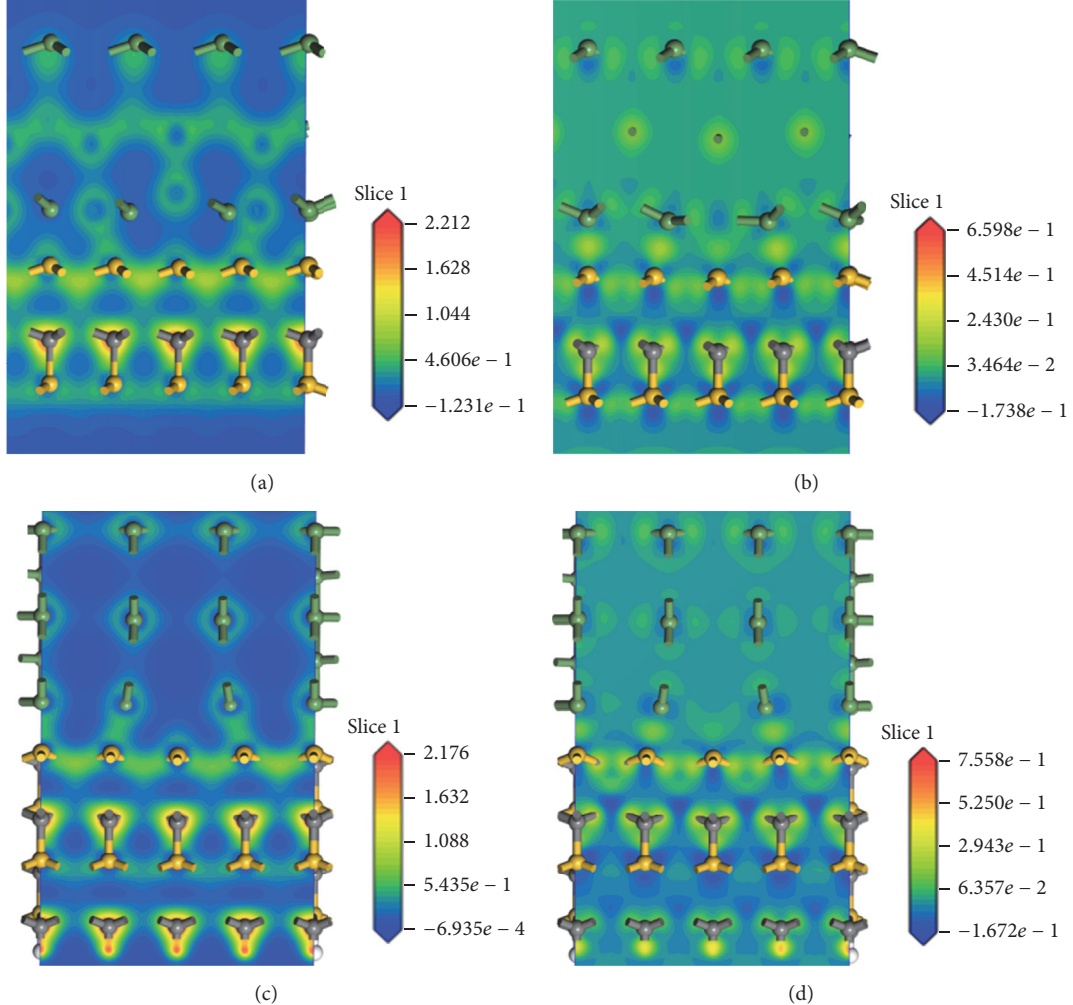


FIGURE 5: Total charge density for Ge(111)/4H-SiC(0001) (a) and Ge(110)/4H-SiC(0001) heterojunction (c). The charge density difference for Ge(111)/4H-SiC(0001) (b) and Ge(110)/4H-SiC(0001) heterojunction (d).

appears between interfacial Ge and Si atom at the Ge(111)/4H-SiC(0001) interface, indicating that Ge-Si bonding is formed at the interface. The charge density difference of Ge(111)/4H-SiC(0001) interface is displayed in Figure 5(b). The blue areas represent the depletion region of the charges, and the yellow areas show the accumulation region of the charge. It is shown that an extremely large amount of charges, which mainly come from the bulk materials near the interface, accumulated at the Ge(111)/4H-SiC(0001) interface, suggesting the formation of Ge-Si bonding at interface due to the transfer of bulk materials. For Ge(110)/4H-SiC(0001) interfaces, there are lots of charge accumulation between Ge atom of Ge crystal and Si atom of SiC crystal in interface, as shown in Figures 5(c) and 5(d). Therefore, the existence of Ge-Si bonding is proved.

An insight into the bonding properties of Ge(110)/4H-SiC(0001) interface and Ge(111)/4H-SiC(0001) interface are provided by calculating the partial density of states (PDOS) of the interface. The partial density of states (PDOS) of Ge(110)/4H-SiC(0001) interface and Ge(111)/4H-SiC(0001) interface are shown in Figures 6(a) and 6(b), respectively.

It reveals that relaxation merely occurs in one or two layers of atoms near the interface by analysing atoms position at the interface. For comparison, hereby, the partial density of states (PDOS) of Ge bulk and 4H-SiC bulk are displayed in Figures 6(a) and 6(b) as well for comparison, and, as a result, several distinct features can be observed. Firstly, compared to the case of bulk materials, the first and second layers exhibit delocalization and lower density, suggesting that electrons in the first and second layers are transferred into the interface and involved in the formation of bonding. Secondly, the distribution of density of states of the first and second layers shifts from the low energy region to the high energy region as compared to the case of bulk materials, which is largely caused by the rearrangement of the atoms and the formation of the interface. Finally, the distribution of density of states of the first and second layers on the Ge side severely deviates from that of the bulk, showing similarity to the distribution of density of states on the SiC side. Similar situation occurs on the distribution of density of states of the first and second layers on the SiC side, indicating that the distribution of

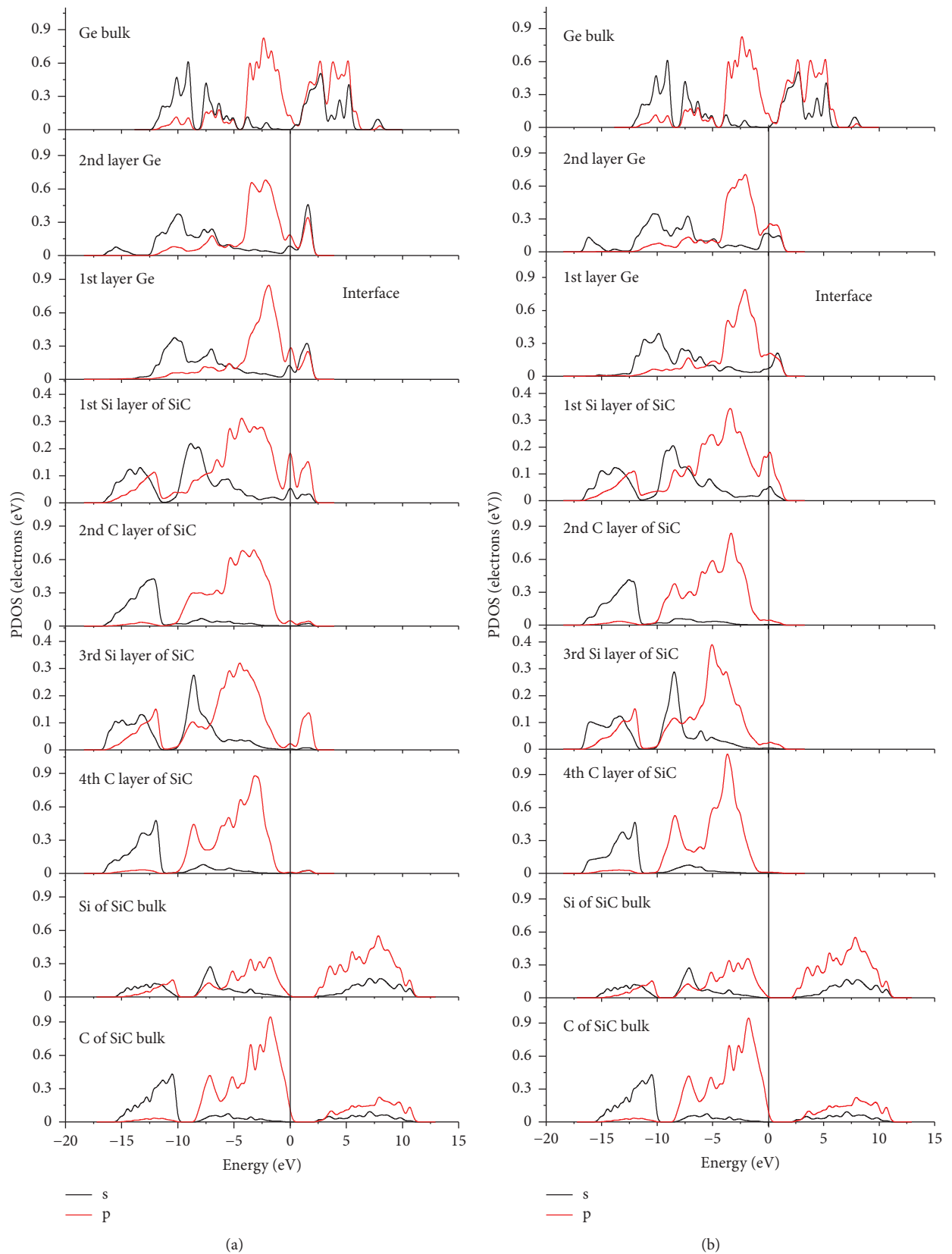


FIGURE 6: Partial density of state (PDOS) of Ge(110)/4H-SiC(0001) (a) and Ge(111)/4H-SiC(0001) heterojunctions (b).

density of states at the interface is influenced by the bulk materials on both sides. As shown in Figure 6(a), on the Ge side, the significant peaks appear in the ranges from -12.5 eV to -6 eV, -6 eV to -5 eV, -5 eV to 1 eV, and 1 eV to 2.5 eV. The densities of states from -12.5 eV to -6 eV and 1 eV to 2.5 eV originate mainly from the Ge-4s, -5 eV to 1 eV is mainly from the Ge-4p, and the Ge-4s and Ge-4p are mixed to the density of states from -6 eV to -5 eV, indicating the presence of Ge-Ge bonds. The density of states from -16 eV to -13 eV is mainly originated from the C-2s and Si-3s, -13 eV to -10 eV is mainly associated with the C-2s and Si-3p, -10 eV to -7.5 eV is mostly related to the C-2p and Si-3s, and -7.5 eV to 0 eV is largely originated from the C-2p and Si-3p. By comparing with the bulk material, the distribution of density of states at the heterointerface shifts toward low energy slightly. Furthermore, by comparing the Ge(110)/4H-SiC(0001) and Ge(111)/4H-SiC(0001) heterointerfaces, for the first Ge layer of Ge slab and the first Si layer of 4H-SiC slab, several distinct resonance peaks appear in the range of -4 eV to 0 eV as well. As shown in Figure 6(b), Ge(111)/4H-SiC(0001) heterointerface significant resonance peaks appear as well. The peaks mainly originate from the orbital hybridization of Si-3p and Ge-4P, indicating the formation of Ge-Si bond at the interface.

4. Conclusions

First-principles calculations are utilized to gain an insight into the interfacial properties of Ge/4H-SiC. The stability, electronic structure, and bonding properties of Ge(111)/4H-SiC(0001) and Ge(110)/4H-SiC(0001) are mainly studied. The works of adhesion of Ge(110)/4H-SiC(0001) and Ge(111)/4H-SiC(0001) interfaces are 0.222 J/m 2 and 0.106 J/m 2 , respectively. The work of adhesion of Ge(110)/4H-SiC(0001) interface is higher than that of the Ge(111)/4H-SiC(0001) interface, leading to that Ge(110)/4H-SiC(0001) interface is more stable than Ge(111)/4H-SiC(0001) interface. Ge(110)/4H-SiC(0001) interface is easier to form at low temperatures due to its lower relaxation energy as compared with Ge(111)/4H-SiC(0001) interface. Calculations on the electronic structure and PDOS indicate that the Ge-Si bonds have been formed at the interface, which are mainly due to the orbital hybridization of Si-3p and Ge-4P.

Conflicts of Interest

The authors declare that they have no conflicts of interest.

Acknowledgments

This work was supported financially by the National Natural Science Foundation of China (Grants nos. 51402230 and 21503153), the Project Supported by Natural Science Basic Research Plan in Shaanxi Province of China (Grants nos. 2015JM6282 and 2017JM6075), Scientific Research Program Funded by Shaanxi Provincial Education Department (Grants nos. 14JK1302 and 17JK0335), and Doctoral Scientific Research Foundation of Xi'an University of Technology (Grant no. Y201605).

References

- [1] L. B. Li, Z. M. Chen, Y. Zang, L. X. Song, Y. L. Han, and Q. Chu, "Epitaxial growth of Si/SiC heterostructures with different preferred orientations on 6H-SiC(0001) by LPCVD," *CrystEngComm*, vol. 18, no. 30, pp. 5681–5685, 2016.
- [2] L. B. Li, Z. M. Chen, Y. Zang, and S. Feng, "Atomic-scale characterization of Si(110)/6H-SiC(0001) heterostructure by HRTEM," *Materials Letters*, vol. 163, pp. 47–50, 2016.
- [3] Q. Chu, L. Li, C. Zhu, Y. Zang, S. Lin, and Y. Han, "Preparation of SiC/Ge/graphene heterostructure on 4H-SiC(0001)," *Materials Letters*, vol. 211, pp. 133–137, 2018.
- [4] Y. L. Han, H. B. Pu, Y. Zang, and L. B. Li, "Epitaxial growth of Ge film on 6H-SiC(0001) by LPCVD," *Optoelectronics and Advanced Materials – Rapid Communications*, vol. 10, no. 9-10, pp. 737–739, 2016.
- [5] K. Alissaad, V. Soulière, F. Cauwet et al., "Ge incorporation inside 4H-SiC during homoepitaxial growth by chemical vapor deposition," *Acta Materialia*, vol. 75, pp. 219–226, 2014.
- [6] P. M. Gammon, A. Pérez-Tomás, M. R. Jennings et al., "Interface characteristics of n-n and p-n Ge/SiC heterojunction diodes formed by molecular beam epitaxy deposition," *Journal of Applied Physics*, vol. 107, no. 12, p. 124512, 2010.
- [7] J. Li, Y. Q. Yang, L. L. Li et al., "Interfacial properties and electronic structure of β -SiC(111)/ α -Ti(0001): A first principle study," *Journal of Applied Physics*, vol. 113, Article ID 023516, 2013.
- [8] Z. Lin, X. Peng, T. Fu et al., "Atomic structures and electronic properties of interfaces between aluminum and carbides/nitrides: A first-principles study," *Physica E: Low-dimensional Systems and Nanostructures*, vol. 89, pp. 15–20, 2017.
- [9] X. M. He, Z. M. Chen, H. B. Pu et al., "First-principles calculations on Si (220) located 6H-SiC (10 $\bar{1}$ 0) surface with different stacking sites," *Chinese Physics B*, vol. 23, no. 10, Article ID 106802, 2014.
- [10] X.-M. He, Z.-M. Chen, L. Huang, and L.-B. Li, "First-principles calculations on atomic and electronic properties of Si(111)/6H-SiC(0001) heterojunction," *Modern Physics Letters B*, vol. 29, no. 29, Article ID 1550182, 2015.
- [11] X. Xu, H. Wang, M. Zha, C. Wang, Z. Yang, and Q. Jiang, "Effects of Ti, Si, Mg and Cu additions on interfacial properties and electronic structure of Al(111)/4H-SiC(0001) interface: A first-principles study," *Applied Surface Science*, vol. 437, pp. 103–109, 2018.
- [12] H. Xiong, Z. Liu, H. Zhang, Z. Du, and C. Chen, "First principles calculation of interfacial stability, energy and electronic properties of SiC/ZrB₂ interface," *Journal of Physics and Chemistry of Solids*, vol. 107, pp. 162–169, 2017.
- [13] J. Yang, J. Huang, D. Fan, and S. Chen, "First-principles investigation on the electronic property and bonding configuration of NbC (111)/NbN (111) interface," *Journal of Alloys and Compounds*, vol. 689, pp. 874–884, 2016.
- [14] J. Martinez, S. B. Sinnott, and S. R. Phillpot, "Adhesion and diffusion at TiN/TiO₂ interfaces: A first principles study," *Computational Materials Science*, vol. 130, pp. 249–256, 2017.
- [15] W. H. Lee and X. H. Yao, "First principle investigation of phase transition and thermodynamic properties of SiC," *Computational Materials Science*, vol. 106, pp. 76–82, 2015.
- [16] M. Piasecki, M. G. Brik, and I. V. Kityk, "Tl₄CdI₆ – Wide band gap semiconductor: First principles modelling of the structural, electronic, optical and elastic properties," *Materials Chemistry and Physics*, vol. 163, pp. 562–568, 2015.

- [17] N. Chandran, M. Sall, J. Arvanitidis et al., “On the Formation of Graphene by Ge Intercalation of a 4H-SiC Surface,” *Materials Science Forum*, vol. 821-823, pp. 961–964, 2015.
- [18] J. Li, Y. Yang, G. Feng, X. Luo, Q. Sun, and N. Jin, “First-principles study of stability and properties on β -SiC/TiC(111) interface,” *Journal of Applied Physics*, vol. 114, no. 16, Article ID 163522, 2013.
- [19] D. Yin, X. Peng, Y. Qin, and Z. Wang, “Electronic property and bonding configuration at the TiN(111)/VN(111) interface,” *Journal of Applied Physics*, vol. 108, no. 3, Article ID 033714, 2010.
- [20] D. Y. Dang, L. Y. Shi, J. L. Fan, and H. R. Gong, “First-principles study of W-TiC interface cohesion,” *Surface and Coatings Technology*, vol. 276, pp. 602–605, 2015.

Research Article

External Electric Field Effect on Shallow Donor Impurity States in Zinc-Blende $\text{In}_x\text{Ga}_{1-x}\text{N}/\text{GaN}$ Symmetric Coupled Quantum Dots

Guang-Xin Wang,¹ Li-Li Zhang,² and Huan Wei¹

¹College of Science, North China University of Science and Technology, Tangshan 063000, China

²Publishing Management Center, North China University of Science and Technology, Tangshan 063000, China

Correspondence should be addressed to Guang-Xin Wang; guangxinwang@126.com

Received 18 July 2017; Accepted 12 September 2017; Published 3 December 2017

Academic Editor: Gongxun Bai

Copyright © 2017 Guang-Xin Wang et al. This is an open access article distributed under the Creative Commons Attribution License, which permits unrestricted use, distribution, and reproduction in any medium, provided the original work is properly cited.

Based on the effective-mass approximation and variational procedure, the ground-state donor binding energy in a cylindrical zinc-blende $\text{In}_x\text{Ga}_{1-x}\text{N}/\text{GaN}$ symmetric coupled quantum dots (SCQDs) is investigated in the presence of the external electric field. Numerical results show that the donor binding energy increases firstly until a maximum value, and then it begins to drop quickly in all the cases with decreasing the dot radius. As the thickness of left dot and right dot decreases, the donor binding energy increases monotonically at first, reaches a maximum value, and then drops rapidly for an impurity ion located at the right dot center and the middle barrier center. Moreover, the donor binding energy for an impurity ion located at the center of the left dot is insensitive to the variation of dot thickness for large dot thickness due to the Stark effect. Meanwhile, the impurity position plays an important role on the change of the donor binding energy under the external electric field. In particular, the impurity position corresponding to the peak value of the donor binding energy is shifted toward the left QD with increasing the external electric field strength.

1. Introduction

Recent advances in modern fabrication techniques have made it possible to grow wide-band-gap GaN-based low-dimensional semiconductor quantum structures [1, 2] and $\text{In}_x\text{Ga}_{1-x}\text{N}$ ternary alloys, as one of the most important members of the group III nitride semiconductor family such as quantum wells (QWs), quantum well wires (QWWs), and quantum dots (QDs), and have attached considerable attention due to their unique electronic and optical properties, as well as their potential applications in electronics and optoelectronic devices [3, 4]. Using molecular-beam epitaxy and metal-organic chemical-vapor deposition methods, the distance between two material layers can precisely be controlled within a few angstroms experimentally. Therefore, the coupling effects between adjacent dots become significant and cannot be neglected, and their electronic structure and optical properties may be adjusted effectively. In the past many years, much theoretical and experimental work

have been devoted in investigating electronic structure and binding energy of a hydrogenic impurity in different shape QDs [5–19]. Liu et al. [5] studied the oscillator strengths of the optical transitions of vertically stacked self-assembled InAs quantum disks. Dong et al. [6] studied single-electron and two-electron vertically assembled quantum disks in an axial magnetic field using the effective-mass approximation. Liu et al. [7] theoretically analyzed the influence of compressive stress on shallow donor impurity states in symmetric GaAs/ $\text{Al}_x\text{Ga}_{1-x}\text{As}$ double quantum dots. L. Z. Liu and J. J. Liu studied [8] hydrogenic-donor impurity states in coupled quantum disks in the presence of a magnetic field. Wang [9] also investigated the ground-state donor binding energy and the average interparticle distances for a hydrogenic impurity in double quantum dots by using variational method. Pressure-dependent shallow donor binding energies have been reported in single QDs [10] and coupled QDs [11]. Xia et al. [12] investigated hydrostatic pressure effect of donor impurity states in zinc-blende (ZB) InGaN/GaN asymmetric

coupled quantum dots. Several factors affect the binding energy of an impurity ion, including the applied external perturbation (magnetic field, hydrostatic pressure), the size of QDs, the barrier thickness, and the position of the donor ion.

On the other hand, applying an external electric field is also a powerful tool to change the electronic and optical properties of low-dimensional semiconductor structures. The Stark effect of donor impurity states in a QD is a major subject for QD physics and applications [13, 14]. The external electric field effect on donor binding energy has been the subject of intensive investigation [15–19]. Xia et al. studied the hydrogenic impurity states in ZB InGaN single QD in the absence of the applied electric field (GaN/AlN coupled QDs) [15, 16]. Jiang et al. [17, 18] presented the external electric field influence on the donor binding energy in a ZB GaN/AlGaN cylindrical (spherical) QD. We also investigated the combined effects of an intense laser field, electric field, and hydrostatic pressure on donor impurity states in zinc-blende InGaN/GaN quantum dots [19].

However, as we know, multiple QDs rather than single QD are adopted in the commonly used GaN-based optoelectronic devices. And few papers are involved in investigating the shallow donor impurity states in ZB $\text{In}_x\text{Ga}_{1-x}\text{N}/\text{GaN}$ SCQDs under the external electric field to date. Thus, it is necessary to study the external electric field effect of the donor impurity states in ZB GaN-based coupled QDs. In this paper, using effective-mass approximation and variational procedure, we report the calculation of ground-state donor binding energy in coupled QDs in the presence of an electric field along the growth direction of the SCQDs. The effects of the structure parameters of the SCQDs, the impurity position, and the applied electric field are all taken into account. This work is organized as follows: in Section 2 we present our theoretical framework, the numerical results are discussed in Section 3, and finally, the conclusions are given in Section 4.

2. Theoretical Framework

2.1. Hamiltonian. Within the effective-mass approximation, the Hamiltonian for a hydrogenic impurity in a cylindrical ZB $\text{In}_x\text{Ga}_{1-x}\text{N}/\text{GaN}$ SCQDs under the influence of applied electric field F in the z -direction, as shown in Figure 1, may be written by [8]

$$\widehat{H} = \widehat{H}_0 - \frac{e^2}{4\pi\epsilon_0\epsilon |\vec{r} - \vec{r}_0|} \quad (1)$$

with

$$\begin{aligned} \widehat{H}_0 = & -\frac{\hbar^2}{2m_{w,b}^*} \left[\frac{1}{\rho} \frac{\partial}{\partial \rho} \left(\rho \frac{\partial}{\partial \rho} \right) + \frac{1}{\rho^2} \frac{\partial^2}{\partial \varphi^2} + \frac{\partial^2}{\partial z^2} \right] \\ & - \frac{e^2}{\epsilon_{w,b} |\vec{r} - \vec{r}_0|} + V(\rho, z) + e\vec{F} \cdot \vec{z}, \end{aligned} \quad (2)$$

where $|\vec{r} - \vec{r}_0| = [\rho^2 + (z - z_0)^2]^{1/2}$ is the distance between an impurity ion and the electron. F is the applied electric

field along the SCQDs growth direction. The subscripts w and b stand for dot layer and barrier layer materials, respectively. $m_{w,b}^*$ and $\epsilon_{w,b}$ are the conduction effective masses and dielectric constants of dot layer and barrier layer, respectively. $V(\rho, z)$ is the radial and z -direction confinement potential due to the conduction band offset in ZB $\text{In}_x\text{Ga}_{1-x}\text{N}/\text{GaN}$ SCQDs, which can be given as follows [10]:

$$V(\rho, z)$$

$$= \begin{cases} V(\rho) & \rho \leq R, \rho > R \\ V(z) & z < -\frac{L_{mb}}{2}, -\frac{L_{mb}}{2} \leq z \leq \frac{L_{mb}}{2}, z > \frac{L_{mb}}{2} \end{cases}$$

$$V(\rho) = \begin{cases} 0 & \rho \leq R \\ V_0 & \rho > R \end{cases}$$

$$V(z) = \begin{cases} V_0 & z < -\frac{(L_{lw} + L_{mb})}{2} \\ 0 & -\frac{(L_{lw} + L_{mb})}{2} < z < -\frac{L_{mb}}{2} \\ V_0 & -\frac{L_{mb}}{2} \leq z \leq \frac{L_{mb}}{2} \\ 0 & \frac{L_{mb}}{2} < z < \frac{(L_{rw} + L_{mb})}{2} \\ V_0 & z > \frac{(L_{rw} + L_{mb})}{2}, \end{cases} \quad (3)$$

where $V_0 = Q[E_g(\text{GaN}) - E_g(\text{In}_x\text{Ga}_{1-x}\text{N})]$. $E_g(\text{GaN})$ and $E_g(\text{In}_x\text{Ga}_{1-x}\text{N})$ are the band gap energies of the materials GaN and $\text{In}_x\text{Ga}_{1-x}\text{N}$, respectively. In order to calculate the ground-state donor binding energy in ZB $\text{In}_x\text{Ga}_{1-x}\text{N}/\text{GaN}$ SCQDs, the trial wave function may be written as follows [11, 12]:

$$\phi(\rho, \phi, z) = Nf(\rho)h(z)e^{il\phi}e^{-\lambda\rho^2-\beta(z-z_0)^2}, \quad l = 0, \pm 1, \pm 2, \dots, \quad (4)$$

where N is the normalization constant and λ and β are variational parameters. Former $f(\rho)$ and latter $h(z)$ are the radial and the axial wave functions, respectively. The former can be obtained through the Bessel function J_m and the modified Bessel function K_m , while the latter can be expressed by means of the Airy functions Ai and Bi . l is the electron z -component angular momentum quantum number. The former is given by [19]

$$f(\rho) = \begin{cases} J_0(\alpha\rho) & \rho \leq R \\ \frac{J_0(\alpha R)}{K_0(\tau R)} K_0(\tau\rho) & \rho > R, \end{cases} \quad (5)$$

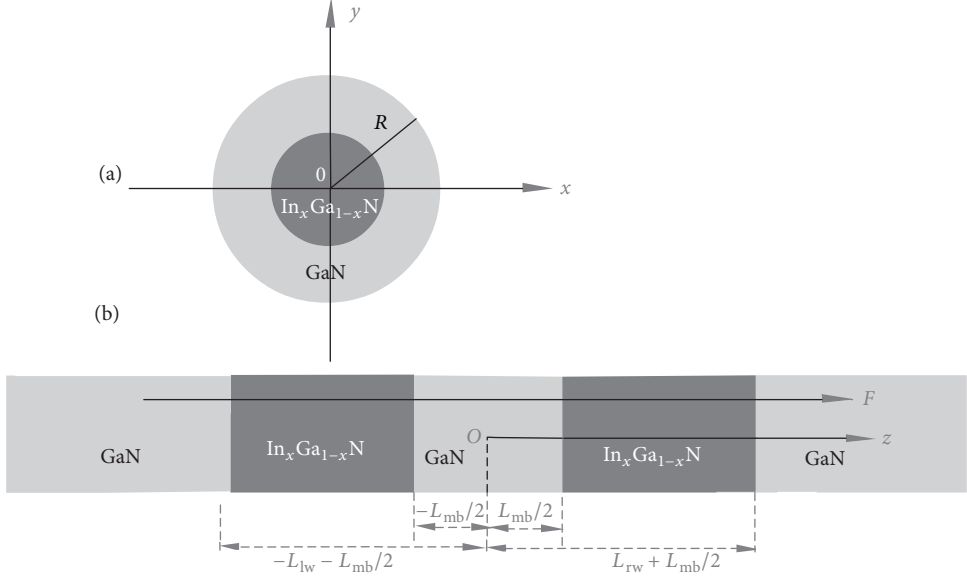


FIGURE 1: A diagram of a cylindrical ZB $\text{In}_x\text{Ga}_{1-x}\text{N}/\text{GaN}$ symmetric coupled QDs of the radius R , the left dot height L_{lw} , the middle barrier width L_{mb} , and the right dot height L_{rw} . The z -axis is defined to be the growth direction of the SCQDs, and the external electric field F is applied along z -axis of the coupled QDs.

where the constants (α and τ) in (5) are determined from the continuity of the derivative of the radial wave function at the SCQDs boundary. The latter is given by

$$h(z) = \begin{cases} C_1 \text{Ai}(\varepsilon_1) + D_1 \text{Bi}(\varepsilon_1) & -L_b - L_{\text{lw}} - \frac{L_{\text{mb}}}{2} < z \leq -L_{\text{lw}} - \frac{L_{\text{mb}}}{2} \\ C_2 \text{Ai}(\varepsilon_2) + D_2 \text{Bi}(\varepsilon_2) & -L_{\text{lw}} - \frac{L_{\text{mb}}}{2} < z \leq -\frac{L_{\text{mb}}}{2} \\ C_3 \text{Ai}(\varepsilon_3) + D_3 \text{Bi}(\varepsilon_3) & -\frac{L_{\text{mb}}}{2} < z \leq \frac{L_{\text{mb}}}{2} \\ C_4 \text{Ai}(\varepsilon_4) + D_4 \text{Bi}(\varepsilon_4) & \frac{L_{\text{mb}}}{2} < z \leq L_{\text{rw}} + \frac{L_{\text{mb}}}{2} \\ C_5 \text{Ai}(\varepsilon_5) + D_5 \text{Bi}(\varepsilon_5) & L_{\text{rw}} + \frac{L_{\text{mb}}}{2} < z < L_{\text{rw}} + \frac{L_{\text{mb}}}{2} + L_b. \end{cases} \quad (6)$$

Here $\varepsilon_j = ((2m_{w,b}^*(p)/\hbar^2)eF)^{1/3}(z - E_z - V(z)/eF)$. The coefficients C_j and D_j ($j=1, 2, 3, 4$, and 5) of the eigenfunction $h(z)$ at the interfaces can be obtained by using transfer matrix methods [20]. The ground-state donor impurity energy is evaluated by minimizing the expectation value of the Hamiltonian with respect to the parameters λ and β . With the adiabatic approximation, the donor binding energy of a hydrogenic impurity E_b is defined as the difference between the ground-state energy of the system with and without impurity; that is, [20]

$$E_b = E_{0\rho} + E_{0z} - \min_{\lambda, \beta} \frac{\langle \psi | H | \psi \rangle}{\langle \psi | \psi \rangle}, \quad (7)$$

where $E_{0\rho}$ and E_{0z} are the radial and the axial ground-state energies of the electron in ZB $\text{In}_x\text{Ga}_{1-x}\text{N}/\text{GaN}$ SCQDs, respectively.

3. Results and Discussion

We have calculated the ground-state donor binding energy E_b as functions of the dot radius R , the dot thickness L ($L_{\text{lw}} = L_{\text{rw}} = L$), the middle barrier width L_{mb} , the impurity positions z_0 , and the applied electric field F in a ZB $\text{In}_x\text{Ga}_{1-x}\text{N}/\text{GaN}$ SCQDs. All parameters used in the present paper are the same as in [21]. The electron effective mass is $m_w^* = [0.2(1-x)+0.12x]m_0$ for $\text{In}_x\text{Ga}_{1-x}\text{N}$ material and $m_b^* = 0.2m_0$ for GaN material [21], and m_0 is the free space electron mass. The band gap energy of ZB $\text{In}_x\text{Ga}_{1-x}\text{N}$ of indium composition x can be given as follows [21]: $E_g(\text{In}_x\text{Ga}_{1-x}\text{N}) = 0.78x + 3.52(1-x) - 1.4x(1-x)$. The band offset ratio is assumed to be 80 : 20. The concentration x in the $\text{In}_x\text{Ga}_{1-x}\text{N}$ material is selected as 0.15.

The ground-state donor binding energy in a ZB $\text{In}_x\text{Ga}_{1-x}\text{N}/\text{GaN}$ SCQDs is displayed in Figure 2 as a function of the dot radius for different external electric fields ($F = 0, 30$, and 50 kV/cm). The impurity ion is located at the left dot center ($z_0 = -(L_{\text{lw}} + L_{\text{mb}})/2$). It can be seen obviously in Figure 2 that the donor binding energy increases firstly until a maximum value, and then it begins to drop quickly in all the cases with the decrease of the dot radius. The behavior is related to the variation of the electron confinement in ZB $\text{In}_x\text{Ga}_{1-x}\text{N}/\text{GaN}$ SCQDs. The electron wave function is more firmly localized inside the QD with decreasing the dot radius, and the Coulomb interaction between the electron and the impurity ion is enhanced, so the donor binding energy increases correspondingly. However, below a certain value of the radius, the donor binding energy starts decreasing due to leakage of the electron wave function into the barrier region. In addition, curves (1–3) also display that the donor binding energy becomes larger with the increase of the applied electric field. This can be explained that as

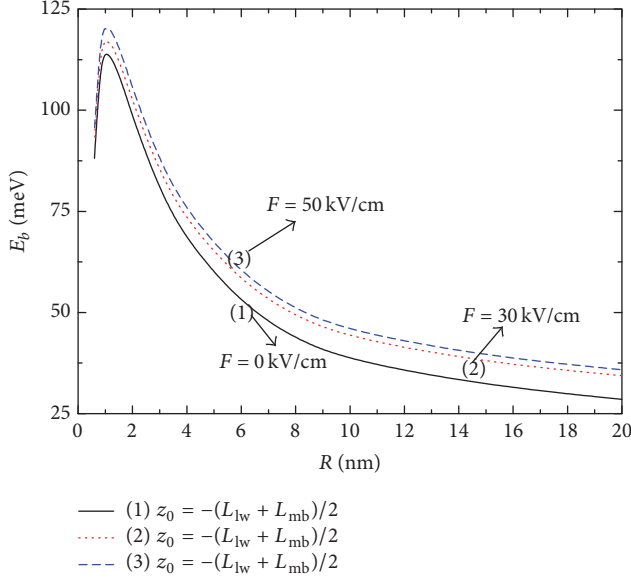


FIGURE 2: The ground-state donor binding energy E_b in a ZB $\text{In}_x\text{Ga}_{1-x}\text{N}/\text{GaN}$ symmetric coupled QDs as a function of the dot radius R with $L_{\text{lw}} = 5 \text{ nm}$, $L_{\text{mb}} = 1 \text{ nm}$, $L_{\text{rw}} = 5 \text{ nm}$, $\rho_0 = 0$. In these calculations were considered three values of the applied electric field—zero (curve 1), $F = 30 \text{ kV/cm}$ (curve 2), and $F = 50 \text{ kV/cm}$ (curve 3).

the applied electric field becomes large, the electron wave function can be shifted toward the left QD in the same spatial confinement, thus leading to a larger donor binding energy.

Figure 3 displays the QD thickness effect on the ground-state donor binding energy with the parameters ($L_{\text{mb}} = 1.0 \text{ nm}$, $R = 10 \text{ nm}$, and $\rho_0 = 0$) for three different positions of the impurity ion: at the right dot center (curve 1), at the left dot center (curve 2), and at the middle barrier center (curve 3). The external electric field along the growth direction of the SCQDs is selected as $F = 30 \text{ kV/cm}$. The thickness of left dot and right dot are selected as the same L in the calculation. It can be seen from curves (1 and 3) that the donor binding energy increases monotonically at first, reaches a maximum value, and then drops rapidly as the dot thickness decreases. The physical reason can be explained as follows: the size quantization confinement of the electron wave function goes stronger with decreasing the thickness of left dot and right dot, and the Coulomb interaction between the electron and the impurity ion becomes larger, and the donor binding energy increases correspondingly. When the thickness of left dot and right dot decreases to a certain value, the probability of the electron leaking into barrier region increases greatly, and hence the Coulomb action between the electron and the impurity ion diminishes accordingly. Comparing curve 2 with the others, it is found that the donor binding energy is insensitive (sensitive) to the variation of the dot thickness for large (small) dot thickness for an impurity ion located at the left dot center. This can be explained by the fact that the electron wave function is strongly shifted into the left QD for large dot thickness under the external electric field and has less freedom to penetrate into the

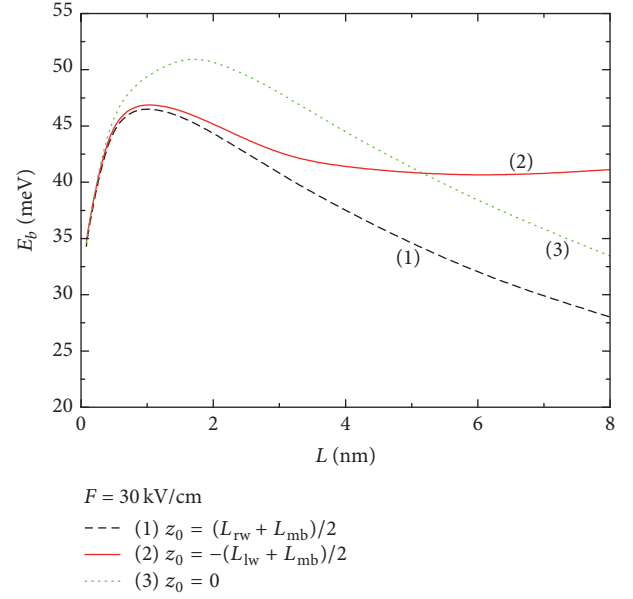


FIGURE 3: The ground-state donor binding energy E_b in a ZB $\text{In}_x\text{Ga}_{1-x}\text{N}/\text{GaN}$ symmetric coupled QDs as a function of the QD thickness L ($L_{\text{lw}} = L_{\text{rw}} = L$) for $R = 10 \text{ nm}$, $L_{\text{mb}} = 1 \text{ nm}$, $F = 30 \text{ kV/cm}$, $\rho_0 = 0$. Curves 1, 2, and 3 are for the impurity positions $z_0 = (L_{\text{rw}} + L_{\text{mb}})/2$, $-(L_{\text{rw}} + L_{\text{mb}})/2$, 0, respectively.

right QD. The average distance between the electron and the impurity ion remains almost constant. Moreover, the spatial confinement effect of the electron wave function is much higher than the external electric field effect for smaller dot thickness. When the dot thickness decreases to a certain value, the probability of the electron penetrating into the potential barrier increases greatly, and the Coulomb interaction between the electron and the impurity ion is weakened accordingly. These behaviors can be explained as the competition effects between external electric field and spatial confinement in a ZB $\text{In}_x\text{Ga}_{1-x}\text{N}/\text{GaN}$ SCQDs.

The effect of the middle barrier width on the donor binding energy for different impurity positions with the parameters ($R = 10 \text{ nm}$, $L_{\text{lw}} = 4 \text{ nm}$, $L_{\text{mb}} = 1 \text{ nm}$, $L_{\text{rw}} = 4 \text{ nm}$, $F = 30 \text{ kV/cm}$) is displayed in Figure 4. It can be seen in Figure 4 that when the middle barrier width L_{mb} is zero, the donor binding energy for the impurity ion located at the center of left dot (curve 1) and right dot (curve 3) is smaller than the one for the impurity ion located at the center of middle barrier (curve 2). These behaviors can be explained as follows. When the middle barrier width goes to zero, the donor binding energy goes to the exact values for a single QD with $R = 10 \text{ nm}$ and $L_w = 8 \text{ nm}$. Therefore, the electron can occupy a larger free space without the middle barrier. The electron cloud is distributed mainly around the impurity position $z_0 = 0$. The average distance between the electron and the impurity ion decreases, which leads to the increase of the donor binding energy. Curves (1 and 3) demonstrate that the donor binding energy decreases firstly, reaches a minimum value, and then increases gradually as the middle barrier thickness L_{mb} increases. This is because

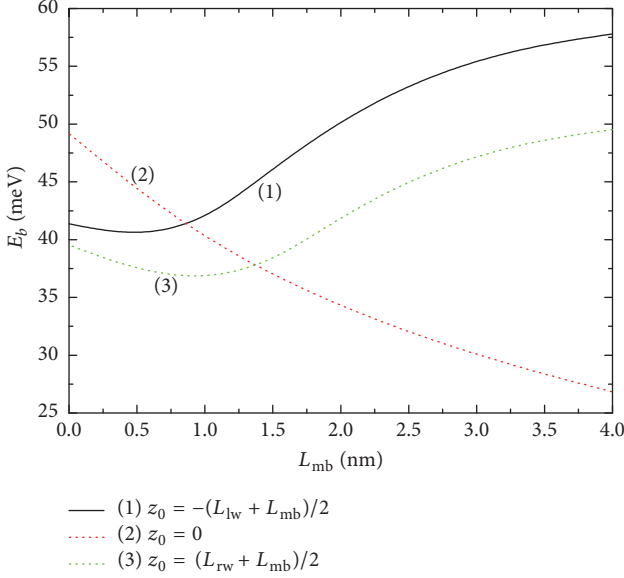


FIGURE 4: The ground-state donor binding energy E_b in a ZB $\text{In}_x\text{Ga}_{1-x}\text{N}/\text{GaN}$ symmetric coupled QDs as a function of the middle barrier width L_{mb} for $R = 10 \text{ nm}$, $L_{lw} = 4 \text{ nm}$, $L_{rw} = 4 \text{ nm}$, $F = 30 \text{ kV/cm}$, $\rho_0 = 0$ for different impurity positions z_0 .

the two QDs are decoupled due to the existence of the small middle barrier width, and the probability of the electron wave function in left dot and right dot penetrating into the middle barrier becomes larger, which leads to the weakening of the Coulomb interaction between the electron and the impurity ion. Therefore, the donor binding energy decreases slightly. Moreover, when the middle barrier thickness increases to a certain value, the coupling effect between the two QDs on the donor binding energy becomes weaker gradually under the external electric field. The bigger the middle barrier width is, the stronger the localization effect of the electron wave function in left dot and right dot is due to the Stark effect. The probability of the electron wave function confined around the impurity ion becomes large. Therefore, the donor binding energy for the impurity ion located at the center of left dot and right dot increases correspondingly. Comparing curve 1 and curve 2, in the same spatial confinement, the donor binding energy for the impurity ion located at the center of left dot is much larger than the one for the impurity ion located at the center of right dot. This is because that the applied electric field pushes greatly the electron wave function into the left QD of the SCQDs. In addition, curve 2 also demonstrates that the donor binding energy for the impurity ion located at the center of the middle barrier decreases gradually with the increase of the middle barrier width. This is because that the probability of the electron wave function penetrating into the middle barrier becomes small under the external electric field with the increase of the middle barrier width. The Coulomb interaction between the electron and the impurity ion weakens gradually, and the donor binding energy decreases correspondingly.

In Figure 5, the external electric field effect on the ground-state donor binding energy for different impurity positions

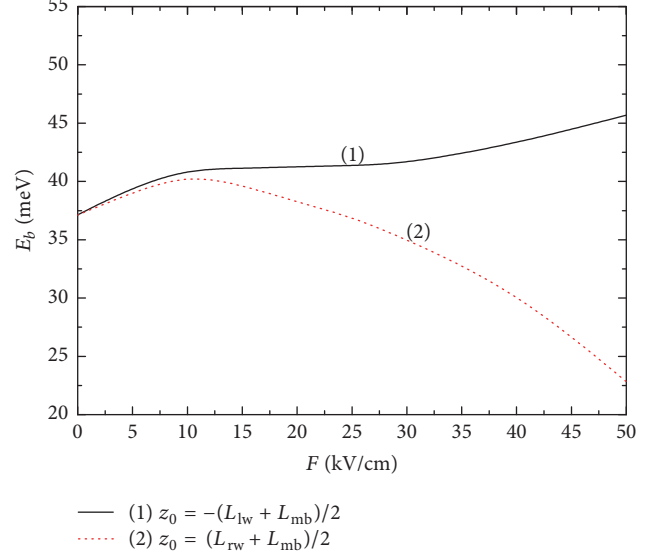


FIGURE 5: The ground-state donor binding energy E_b in a ZB $\text{In}_x\text{Ga}_{1-x}\text{N}/\text{GaN}$ symmetric coupled QDs as a function of the electric field F for $R = 10 \text{ nm}$, $L_{lw} = 4 \text{ nm}$, $L_{mb} = 1 \text{ nm}$, $L_{rw} = 4 \text{ nm}$, $\rho_0 = 0$. Curves 1, 2 are for the impurity positions $z_0 = -(L_{lw} + L_{mb})/2$, $(L_{rw} + L_{mb})/2$, respectively.

($z_0 = -(L_{lw} + L_{mb})/2$ (curve 1), $z_0 = (L_{rw} + L_{mb})/2$ (curve 2)) is showed with the parameters ($R = 10 \text{ nm}$, $L_{lw} = 4 \text{ nm}$, $L_{mb} = 1 \text{ nm}$, $L_{rw} = 4 \text{ nm}$). For the impurity ion located at the center of the left QD (curve 1), the increase of the applied electric field F leads to an enhancement of the donor binding energy. It is because that as the applied electric field increases, the probability of the electron penetrating into the left dot increases greatly, and the electron is strongly confined around the impurity ion. In addition, curve 2 also shows that the donor binding energy increases firstly, reaches a maximum value, and then decreases gradually. The main reason is as follows: the smaller external electric field enhances the localization effect of the electron wave function in the right dot. The distance between the electron and the impurity ion decreases, which causes the increase of the donor binding energy. When the applied electric field increases to a certain value, the probability of the electron in the right dot leaking into barrier layer and left dot increases greatly, which leads to the decrease of the donor binding energy. In addition, the stronger the applied electric field is, the more significant the change of the donor binding energy is. The same effect has also been observed for vertical-stacked InGaN/GaN multiple-quantum wells [20].

In Figure 6, the ground-state donor binding energy is investigated as a function of the axial position z_0 of the impurity ion in the ZB $\text{In}_x\text{Ga}_{1-x}\text{N}/\text{GaN}$ SCQDs with the parameters $R = 10 \text{ nm}$, $L_{lw} = 4 \text{ nm}$, $L_{mb} = 1 \text{ nm}$, $L_{rw} = 4 \text{ nm}$, $\rho_0 = 0$ and with different external electric fields ($F = 0$, 30 kV/cm , and 50 kV/cm). Curve 1 demonstrates that, in the absence of the electric field, the donor binding energy has two maximum values, which are located at the center of left and right QDs and symmetrical with respect to the middle barrier center. This can be understood such that the electric

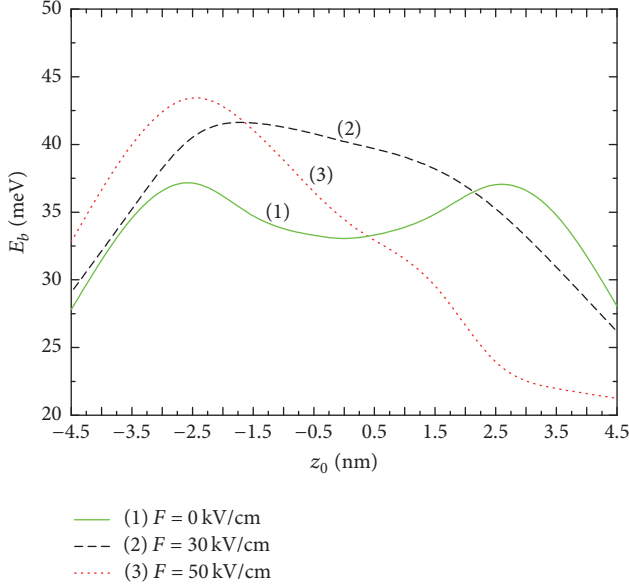


FIGURE 6: The ground-state donor binding energy E_b in a ZB $\text{In}_x\text{Ga}_{1-x}\text{N}/\text{GaN}$ symmetric coupled QDs as a function of the impurity position z_0 for $R = 10$ nm, $L_{\text{lw}} = 4$ nm, $L_{\text{mb}} = 1$ nm, $L_{\text{rw}} = 4$ nm, $\rho_0 = 0$ for different external electric field $F = 0$, 30 kV/cm, and 50 kV/cm.

field effect on the system disappears and leads to the coupled QDs becoming a symmetrical configuration. The electron wave function is strongly and symmetrically confined inside left dot and right dot of the ZB $\text{In}_x\text{Ga}_{1-x}\text{N}/\text{GaN}$ SCQDs in the spatial confinement, and therefore the increment of the Coulomb interaction between the electron and the impurity ion that causes the increase of the donor binding energy. In addition, it may also be seen in curves (2-3) that when the external electric field is applied, only a maximum value is remained. And the impurity position corresponding to the peak value of the donor binding energy is shifted toward left dot of the ZB $\text{In}_x\text{Ga}_{1-x}\text{N}/\text{GaN}$ SCQDs with increasing the external electric field. This is because the applied electric field pushes greatly the electron wave function into left dot of the SCQDs. Figure 6 also demonstrates that the stronger the applied electric field is, the bigger the peak value of the donor binding energy is. It is because the maximum localization effect of the electron wave function in the ZB $\text{In}_x\text{Ga}_{1-x}\text{N}/\text{GaN}$ SCQDs strengthens as the applied electric field increases. As a general feature, these behaviors can be explained as the combined effects between external electric field, quantum confinement, and coupled action of the SCQDs.

4. Conclusion

In conclusion, we have investigated the combined effects of an external electric field, spatial confinement, and coupled action on a shallow donor impurity confined in a cylindrical ZB $\text{In}_x\text{Ga}_{1-x}\text{N}/\text{GaN}$ symmetric coupled QDs. The calculations were performed by using a variational procedure based on the effective-mass approximation. The donor binding

energy is investigated as a function of the dot radius, the dot thickness, the external electric field, and the impurity position. Number results can be summarized as follows: (1) as the QD radius increases, the donor binding energy increases firstly until a maximum value, and then it begins to drop quickly in all the cases; (2) as the dot thickness L decreases, the donor binding energy increases monotonically at first, reaches a maximum value, and then drops rapidly for the impurity located at right dot center and middle barrier center. Moreover, the donor binding energy is insensitive to the variation of dot thickness for large dot thickness when the impurity ion is located at the left dot center. (3) When the impurity ion is located at the center of left dot and right dot, respectively, as the middle barrier thickness L_{mb} increases, the donor binding energy decreases firstly, reaches a minimum value, and then increases gradually. And the donor binding energy for the impurity ion located at the center of middle barrier decreases gradually with the increase of the middle barrier width. (4) The external electric field significantly affects the distribution of the electron wave function in the ZB $\text{In}_x\text{Ga}_{1-x}\text{N}/\text{GaN}$ SCQDs. And the electron wave function is shifted toward the left QD under the external electric field. (5) In the absence of the electric field, the donor binding energy has two maximum values, which are symmetrically located on the center of left dot and right dot of ZB $\text{In}_x\text{Ga}_{1-x}\text{N}/\text{GaN}$ SCQDs. When the external electric field is applied, only a maximum value is remained, and the stronger the applied electric field is, the bigger the peak value of the donor binding energy is. The main results obtained in this paper might be suitable for other ZB semiconductor quantum structures. We hope that these calculation results can stimulate further investigations of the physics and device applications of group III nitride materials.

Conflicts of Interest

The authors declare that there are no conflicts of interest regarding the publication of this paper.

Acknowledgments

This work was supported by The Education Department Foundation of Hebei Province (no. QN2015050).

References

- [1] A. Lotsari, G. P. Dimitrakopoulos, T. Kehagias, A. Das, E. Monroy, and P. Komninou, "Structural properties of semipolar InGaN/GaN quantum dot superlattices grown by plasma-assisted MBE," *Microelectronic Engineering*, vol. 90, pp. 108–111, 2012.
- [2] S. Nakamura and S. F. Chichibu, *Introduction to Nitride Semiconductor Blue Lasers and Light Emitting Diodes*, Taylor & Francis, London, UK, 2000.
- [3] W. S. Tan, V. Bousquet, M. Kauer, K. Takahashi, and J. Hefernan, "Ingan-based blue-violet laser diodes using AlN as the electrical insulator," *Japanese Journal of Applied Physics*, vol. 48, no. 7, Article ID 072102, 2009.

- [4] M. Gladysiewicz, R. Kudrawiec, J. Misiewicz et al., "The surface boundary conditions in GaN/AlGaN/GaN transistor heterostructures," *Applied Physics Letters*, vol. 98, no. 1, Article ID 231902, 2011.
- [5] J. L. Liu, S. S. Li, Z. C. Niu, F. H. Yang, and S. L. Feng, "Optical spectra and exciton state in vertically stacked self-assembled quantum discs," *Chinese Physics Letters*, vol. 20, no. 7, pp. 1120–1123, 2003.
- [6] Q. R. Dong, S. S. Li, Z. C. Niu, S. L. Feng, and H. Z. Zheng, "Electronic structure of self-assembled InAs quantum disks in an axial magnetic field and two-electron quantum-disk qubit," *Journal of Applied Physics*, vol. 96, no. 6, pp. 3277–3281, 2004.
- [7] J. J. Liu, M. Shen, and S. W. Wang, "The influence of compressive stress on shallow-donor impurity states in symmetric GaAs-Ga_{1-x}Al_xAs double quantum dots," *Journal of Applied Physics*, vol. 101, no. 7, Article ID 073703, 2007.
- [8] L. Z. Liu and J. J. Liu, "Hydrogenic-donor impurity states in coupled quantum disks in the presence of a magnetic field," *Journal of Applied Physics*, vol. 102, no. 3, Article ID 033709, 2007.
- [9] X. F. Wang, "Hydrogenic impurity in double quantum dots," *Physics Letters A*, vol. 364, no. 1, pp. 66–69, 2007.
- [10] G. X. Wang, X. Z. Duan, and W. Chen, "Barrier thickness and hydrostatic pressure effects on hydrogenic impurity states in wurtzite GaN/Al_xGa_{1-x}N strained quantum dots," *Journal of Nanomaterials*, vol. 2015, Article ID 937310, 9 pages, 2015.
- [11] M. Zhang and J. J. Shi, "Influence of pressure on exciton states and interband optical transitions in wurtzite InGaN/GaN coupled quantum dot nanowire heterostructures with polarization and dielectric mismatch," *Journal of Applied Physics*, vol. 111, Article ID 113516, 11 pages, 2012.
- [12] C. X. Xia, Z. P. Zeng, Q. Chang, and S. Y. Wei, "Donor impurity states in zinc-blende InGaN/GaN asymmetric coupled quantum dots: Hydrostatic pressure effect," *Physica E: Low-dimensional Systems and Nanostructures*, vol. 42, no. 8, pp. 2041–2046, 2010.
- [13] H. El Ghazi, A. Jorio, and I. Zorkani, "Theoretical investigation of stark effect on shallow donor binding energy in InGaN spherical QD-QW," *Physica B: Condensed Matter*, vol. 422, pp. 47–50, 2013.
- [14] B. E. Kane, "A silicon-based nuclear spin quantum computer," *Nature*, vol. 393, no. 6681, pp. 133–137, 1998.
- [15] C. X. Xia, Y. M. Liu, and S. Y. Wei, "Hydrogenic impurity states in zinc-blende GaN/AlN coupled quantum dots," *Physics Letters A*, vol. 372, no. 42, pp. 6420–6423, 2008.
- [16] F. C. Jiang, C. X. Xia, and S. Y. Wei, "Hydrogenic impurity states in zinc-blende InGaN quantum dot," *Physica B: Condensed Matter*, vol. 403, no. 1, pp. 165–169, 2008.
- [17] L. M. Jiang, H. L. Wang, H. T. Wu, Q. Gong, and S. L. Feng, "External electric field effect on the hydrogenic donor impurity in zinc-blende GaN/AlGaN cylindrical quantum dot," *Journal of Applied Physics*, vol. 105, no. 5, Article ID 053710, 2009.
- [18] L. M. Jiang, H. L. Wang, H. T. Wu, Q. Gong, and S. L. Feng, "External electric field effect on hydrogenic donor impurity in zinc-blende InGaN quantum dot," *Chinese Physics Letters*, vol. 25, no. 8, pp. 3017–3020, 2008.
- [19] G. X. Wang, R. Zhou, and X. Z. Duan, "Combined effects of an intense laser field, electric field and hydrostatic pressure on donor impurity states in zinc-blende InGaN/GaN quantum dots," *Journal of the Korean Physical Society*, vol. 69, no. 2, pp. 189–196, 2016.
- [20] C. X. Xia, Z. P. Zeng, S. Y. Wei, and J. B. Wei, "Shallow-donor impurity in vertical-stacked InGaN/GaN multiple-quantum wells: electric field effect," *Physica E: Low-dimensional Systems and Nanostructures*, vol. 43, no. 1, pp. 458–461, 2010.
- [21] T. Vurgaftman and J. R. Meyer, "Band parameters for III-V compound semiconductors and their alloys," *Journal of Applied Physics*, vol. 94, no. 6, pp. 3676–3696, 2003.

Research Article

Surface Plasmon Resonance Enhanced Spontaneous Upconversion and Stimulated Emissions in Glass Ceramics Containing Ba₂LaF₇ Nanocrystals

Sai Li,¹ Wei Lu,² Qihua Yang,¹ Dacheng Zhou,^{1,3} Jianbei Qiu,^{1,3} Xuhui Xu,^{1,3} and Xue Yu^{1,3}

¹College of Materials Science and Engineering, Kunming University of Science and Technology, Kunming 650093, China

²University Research Facility in Materials Characterization and Device Fabrication,

The Hong Kong Polytechnic University, Hung Hom, Hong Kong

³Key Laboratory of Advanced Materials of Yunnan Province, Kunming 650093, China

Correspondence should be addressed to Xue Yu; yuyu6593@126.com

Received 19 June 2017; Accepted 10 August 2017; Published 13 September 2017

Academic Editor: Zaiquan Xu

Copyright © 2017 Sai Li et al. This is an open access article distributed under the Creative Commons Attribution License, which permits unrestricted use, distribution, and reproduction in any medium, provided the original work is properly cited.

Glass ceramics containing Yb³⁺, Er³⁺ codoped Ba₂LaF₇ nanocrystals were fabricated via melt quenching method and the subsequent heating treatment. The formation of Ba₂LaF₇ nanocrystals in the glass ceramics was confirmed by X-ray diffraction (XRD) and transmission electron microscope (TEM). The spontaneous upconversion (UC) emission and the stimulated counterpart as a random lasing action of Er³⁺, which were related to the characteristic transitions of Er³⁺ ions, were achieved in the Yb³⁺, Er³⁺-doped Ba₂LaF₇ nanocrystals embedded glass ceramic hybrid. Furthermore, the absorption spectra verified the surface plasmon resonance (SPR) band of Ag, which precipitated from the matrix glasses as Ag nanoparticles (NPs). By incorporating Ag NPs in the glass ceramic hybrid, spontaneous UC emission intensity of Er³⁺ in visible region was significantly enhanced, while the threshold of the random lasing was decreased from 480 to 350 nJ/cm².

1. Introduction

The integration of novel luminescent nanometer materials into glassy matrix can bring about new and promising optical hybrid materials and photonic devices in recent years [1]. Great enhancement of optical emission efficiency was realized in fluorosilicate glasses by the growth of the lanthanide doped fluoride nanocrystals embedded in the glass matrix [2]. Lanthanide-containing UC nanocrystals have become distinct candidates for biomedical imaging, anticounterfeiting, biological sensing, solar energy management, data storage, and 3D volumetric displays, which enable higher-energy emissions in the ultraviolet to visible spectral range by upconverting two or more near-infrared excitation photons [3, 4]. Once lanthanide ions are located inside the fluoride nanocrystals, they will be in the low phonon energy environment. So the multiphonon relaxation rates can be significantly reduced from some excited states [5, 6]. Oxyfluoride glass ceramics combine the favorable properties of fluoride

crystal (low refractive index and phonon energy) and the oxide glasses (high chemical stability and large solubility of rare-earth (RE) ions). Thus, oxyfluoride glass ceramics have potential applications in the fields of luminescence applications and laser [7].

Er³⁺-doped UC materials are popular due to their high luminescence quenching concentration compared to other rare-earth ions. In addition, Er³⁺ ions have a large spectral overlap with Yb³⁺, and Yb³⁺ ions can absorb the photons of 980 nm effectively. Therefore, Yb³⁺ and Er³⁺ codoping materials can enhance the UC efficiency through the energy transfer, which demonstrated that the Yb³⁺ and Er³⁺ codoping materials exhibit excellent luminescent properties. SPR arises by the collective oscillation of electrons on the metal nanoparticles, which can have either beneficial or deleterious effect depending on the position of the SPR peak and the distance of the luminophore from the metal surface [8, 9]. Recently, SPR has been energetically used to improve the emission efficiency of luminescent materials and devices.

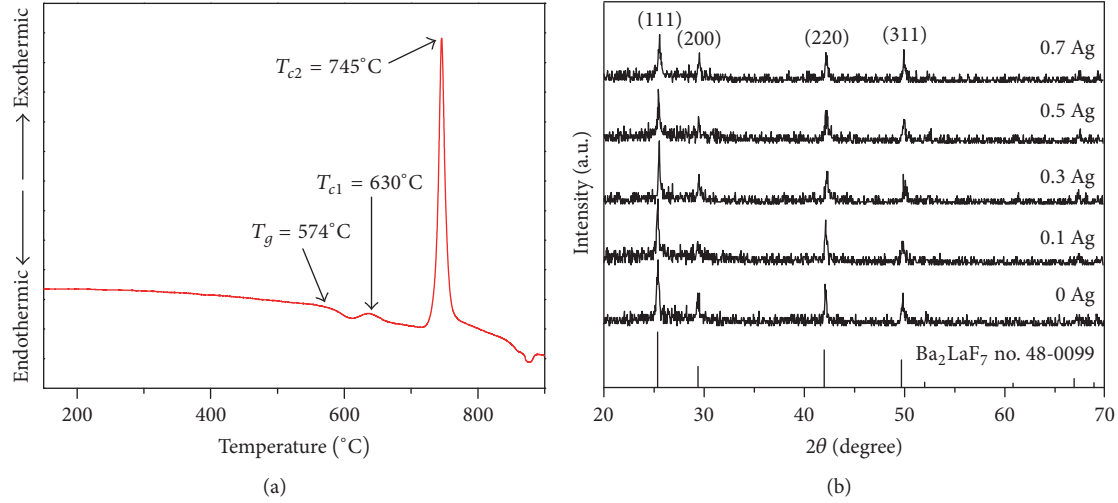


FIGURE 1: (a) DSC of 0.5 Ag sample. (b) XRD patterns of glass ceramic samples with different Ag concentration.

For example, the photoluminescence (PL) intensity in the dye-doped polymers [10], CdSe quantum dots [11], Si quantum dots [12], ZnO films [13, 14], and InGaN quantum wells [15] was improved significantly due to the SPR excitation. In contrast to the continuous efforts to spontaneous emissions, little knowledge has been known in the stimulated counterparts. However, the incorporation of metallic nanostructures into optical gain media may lead to a breakthrough of laser devices, that is, to beat the diffraction limit with regard to both of the physical dimension and optical mode size [16]. Besides, the enhanced local field occurring in hot spots is particularly important to trigger low threshold lasing resonance because it can locally enhance the pump rate of gain media [7, 17].

Thus, in this work, Yb^{3+} , Er^{3+} -doped Ba_2LaF_7 glass ceramic as an effective UC material was synthesized via conventional melt quenching technique and the subsequently heat treatment. Besides, a nanosecond laser pumped random lasing action has been achieved in the silicate oxyfluoride glass ceramics containing Ba_2LaF_7 nanocrystals. By incorporating Ag NPs, spontaneous UC emission intensity of Er^{3+} in visible region was drastically enhanced, while the threshold of the random lasing decreased significantly from 450 to 350 nJ/cm².

2. Experimental

The glass ceramic samples were prepared according to the following composition (mol%): 45SiO₂-15Al₂O₃-12Na₂CO₃-20BaF₂-6.5LaF₃-1YbF₃-0.5ErF₃ doped with x wt% of Ag₂O by the conventional melt quenching technique ($x = 0, 0.1, 0.3, 0.5, 0.7$), denoted as 0 Ag, 0.1 Ag, 0.3 Ag, 0.5 Ag, and 0.7 Ag. About 10 g of original material was fully mixed and then melted in an air atmosphere at 1500°C for 45 min. The crucible was covered with an alumina cap to avoid volatilization loss. The molten glass was cast into a carbon plate maintained at about 300°C. The glass samples were annealed at 500°C for 8 h to avoid internal stress. The

obtained glass was thermally treated at 670°C for 2 h to induce crystallization.

XRD was performed using a D8 Focus diffractometer (Bruker) with Cu-K α radiation ($\lambda = 0.15405$ nm) in the 2θ range from 20° to 70°. The UC photoluminescence spectra in the wavelength range of 450 to 700 nm were recorded by using a HITACHI-7000. Fluorescence spectrophotometer was under the excitation of 980 nm laser diode with the power of 2 W. The absorption spectra were recorded in the wavelength range from 350 to 600 nm using a Model U-4100 Spectrophotometer. To detect the nucleation and growth of Ag NPs, a TEM (JEM-2100) operating at an accelerating voltage of 200 kV was used. For the laser measurement, a Continuum Panther EX optical parametric oscillator and a 355 nm frequency-tripled Continuum Powerlite DLS 9010 Q-switched Nd: YAG laser were used to generate 980 nm pump pulses of width and repetition rate of ≈ 6 ns and 10 Hz, respectively. The laser beam of diameter equal to 8 mm was focused on the surface of the glass ceramics by a cylindrical lens with focal length of 100 mm. Light emitted from the side of the glass was recorded by an optical fiber connected to a spectrum analyzer (Oriel MS257 monochromator with spectral resolution ≈ 0.1 nm). The sample was placed in a temperature regulating chamber with N₂ (Linkam DSC 600 stage system). For the sample under pulse excitation, the temperature rise was negligible due to the influence of the optical pumping. However, for continuous wave excitation samples, the average temperature of the sample must be offset 18 K.

3. Results and Discussion

Figure 1(a) shows the differential scanning calorimetry (DSC) spectrum of the 0.5 Ag sample. As can be seen in this figure, there are three temperature parameters: the glass transition temperature (T_g) located in the vicinity of 574°C and temperature of two crystallization peaks (T_{c1} , T_{c2}) located at the vicinity of 630°C and 745°C. According to the

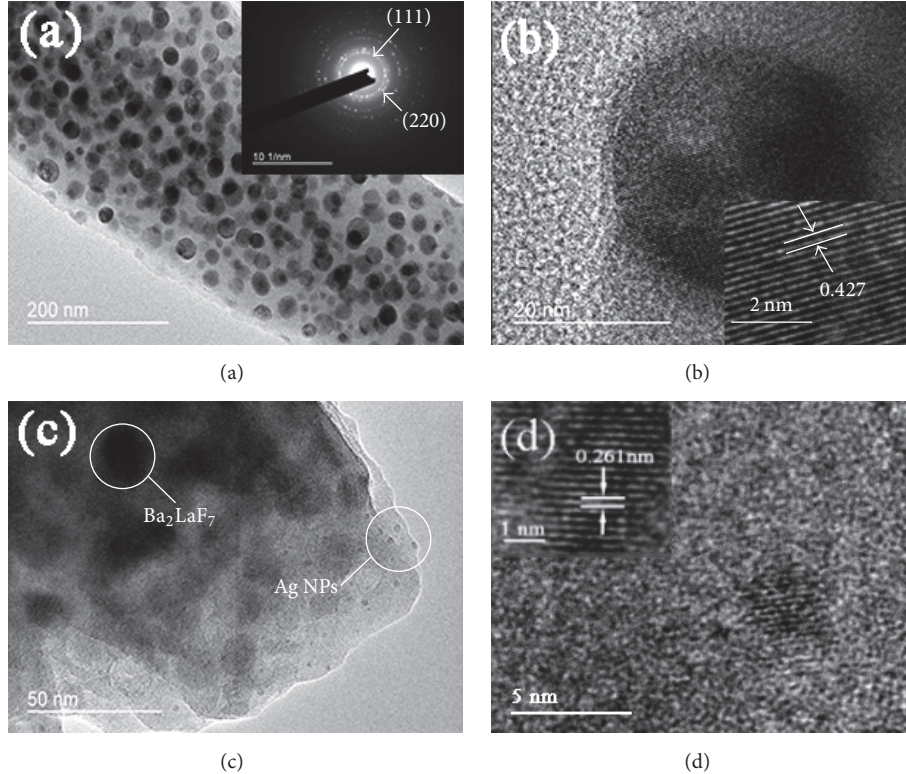


FIGURE 2: (a) TEM micrograph of 0 Ag sample; the inset is the SAED pattern of the 0 Ag sample. (b) HR-TEM image of 0 Ag sample; the inset is the enlargement of HR-TEM image of the corresponding sample. (c) TEM micrograph of 0.5 Ag sample. (d) HR-TEM image of 0.5 Ag sample; the inset is the enlargement of HR-TEM image of the corresponding sample.

differential thermal analysis (DTA) results analysis, in this study, all the prepared glasses were heat-treated at 670°C for 2 h to precipitate nanocrystals. Figure 1(b) displays the XRD patterns of the samples by modulating the Ag concentration, respectively. All the diffraction peaks of the samples are in good agreement with hexagonal Ba_2LaF_7 (the standard JCPDS 48-0099). No second phase is detected in the XRD pattern, revealing that the high purity cubic phase of Ba_2LaF_7 has been fabricated.

The TEM micrograph of the 0 Ag sample in Figure 2(a) demonstrates that Ba_2LaF_7 nanocrystals with the diameter of 7–12 nm distribute homogeneously among the glass matrix. HR-TEM image of Figure 2(b) shows the presence of clear and resolved lattice fringes of 0 Ag sample. The inset in Figure 2(b) is the enlargement of HR-TEM image of the corresponding sample. As shown in the inset of Figure 2(b), the interplanar distance between the adjacent fringes is determined to be 0.427 nm, which matches well, respectively, with those of the (111) plane of the cubic Ba_2LaF_7 . The TEM image of the 0.5 Ag sample is shown in Figure 2(c), indicating the presence of near-spherical NPs distributed homogeneously in the glass matrix with the particle size of about 2 to 4 nm. Figure 2(d) is the HR-TEM image of 0.5 Ag sample and the enlargement of HR-TEM image of the corresponding (the inset of Figure 2(d)). It shows that the interplanar distance between the adjacent fringes is determined to be 0.261 nm ascribed to the (200) planes of Ag. Thus, it is unambiguous

evidence that Ag NPs are randomly distributed in the glass matrix.

Figure 3(a) shows the UC photoluminescence spectra of 0 Ag, 0.1 Ag, 0.3 Ag, 0.5 Ag, and 0.7 Ag samples pumped by 980 nm with 60 W/cm^2 excitation density. The characteristic green (540 nm) and red (658 nm) emissions, corresponding to ${}^4\text{S}_{3/2} \rightarrow {}^4\text{I}_{15/2}$ and ${}^4\text{F}_{9/2} \rightarrow {}^4\text{I}_{15/2}$ transitions of Er^{3+} , respectively, are simultaneously observed. The UC emission intensity is greatly improved with increasing concentration of Ag_2O , and the maximum enhancement is realized when the concentration of Ag_2O is up to 0.5 wt%. Then, the UC emission intensity decreases with further increase of Ag_2O concentrations. The inset exhibits the absorption spectra of the 0 Ag, 0.1 Ag, 0.3 Ag, 0.5 Ag, and 0.7 Ag samples. Absorption bands attributed to 4f-4f transitions of Er^{3+} ions corresponding to transitions starting from the ground state to the excited states are observed. As shown in the inset, the absorption spectra of the sample with Ag_2O show a distinctive band centered at 420 nm that is attributed to the SPR associated with the Ag NPs [18]. The primary reason for such fluorescence intensification of RE ions which is attributed to a local field enhancement induced by SPR of metal NPs has been accepted [19–23].

In order to investigate the dependence of the UC emission intensities on the Ag_2O concentrations in detail, the emission decay curves of the ${}^4\text{S}_{3/2} \rightarrow {}^4\text{I}_{15/2}$ transitions of Er^{3+} in the series of Ag doped samples were measured under the 980 nm

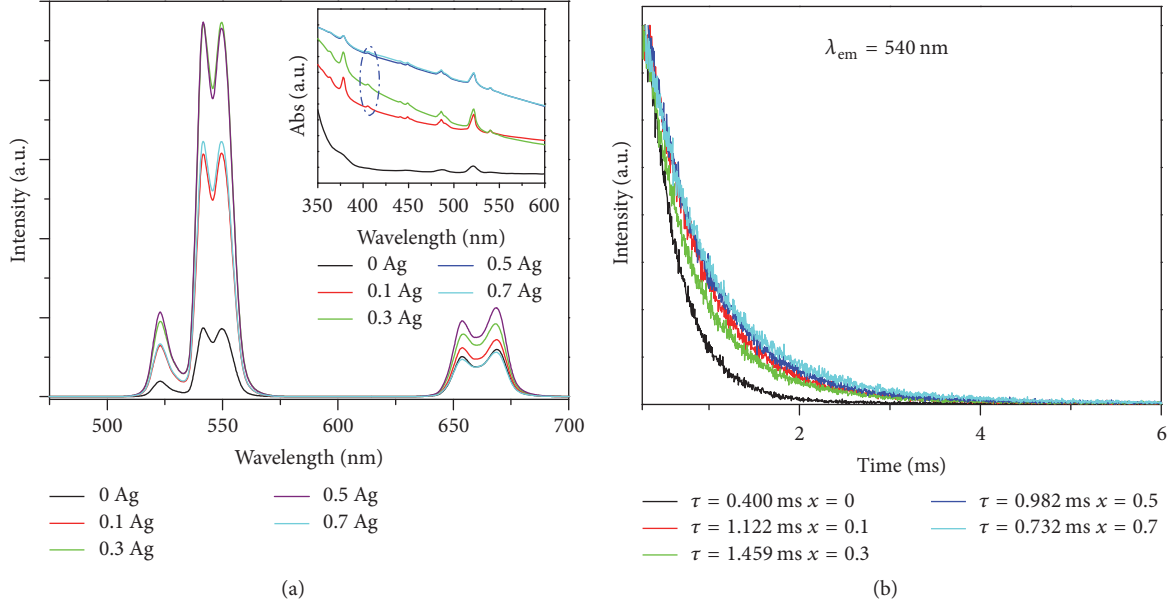


FIGURE 3: (a) UC luminescence spectra of samples with different Ag concentration under the excitation of 980 nm laser diode: the inset is absorption spectra of samples by modulating the Ag concentration. (b) Room temperature luminescence decay curves of ${}^4S_{3/2} \rightarrow {}^4I_{15/2}$ (Er^{3+}) transition of the 0 Ag, 0.1 Ag, 0.3 Ag, 0.5 Ag, and 0.7 Ag samples.

excitation, as displayed in Figure 3(b). The effective experimental lifetime can be evaluated as follows:

$$\tau_{\text{eff}} = \frac{\int [I(t) * t * dt]}{\int [I(t) * dt]}, \quad (1)$$

where $I(t)$ represents the luminescence intensity at time t after the cut-off of the excitation light. The lifetime of the transitions of ${}^4S_{3/2} \rightarrow {}^4I_{15/2}$ is determined to be 0.400, 1.122, 1.459, 0.982, and 0.732 ms in the 0 Ag, 0.1 Ag, 0.3 Ag, 0.5 Ag, and 0.7 Ag samples, respectively. The lifetime decreases after the first increase, and the variation tendency agrees well with the change of UC luminescence intensities of green emission. The lifetime result is an evidence of an accelerating energy transfer from Yb^{3+} to Er^{3+} with increasing Ag NPs content [24, 25], which indicates that some energy transfer from fluorescent Ag NPs to Er^{3+} cannot be totally ignored.

Interestingly, microcavities can be realized by randomly embedding $Ba_2LaF_7:Yb^{3+}, Er^{3+}$ nanocrystals inside the glass and random lasing action can be achieved in the glass ceramic. The optically pumped spectra of 0.5 Ag sample were collected under the 980 nm nanosecond laser beam; it was found that the Ag NPs decorated glass ceramics containing Ba_2LaF_7 nanocrystals exhibit a similar optically pumped random lasing characteristic as the corresponding glass ceramics without Ag. Figure 4(a) shows the lasing characteristics of the glass ceramics with the decoration of Ag NPs under different 980 nm pulsed excitation power at room temperature. As the pump energy exceeds an excitation threshold, P_{th} , of 385 nJ/cm² (i.e., kink of the light-light curve as shown in Figure 4(b)), one sharp peak emerges from the emission spectrum. In addition, further increase of the excitation intensity increases the number of sharp peaks. In

this case, the sharp peaks represent the formation of closed-loop paths for light (i.e., the realization of microcavities due to the coherent optical feedback from the Ag NPs). Figure 4(b) provides a direct proof of the central role of local field enhancement in the emergence of low threshold lasing resonance, and the threshold of the lasing decreased from 480 to 350 nJ/cm² with decorating of Ag NPs. It can be safe to say that the enhanced local field occurring in hot spots is particularly important to trigger low threshold lasing resonance since it can locally enhance the pump rate of gain media [26, 27]. The corresponding plot of Fourier transform spectrum, as shown in Figure 4(c), exhibits periodic features, indicating the formation of closed-loop paths, and the round-trip cavity length of the random modes inside the glass hybrid is ca. 9.81 μ m. The inset of Figure 4(a) is the photograph of the 0.5 Ag under the excitation of 980 nm nanosecond laser. It is clearly seen that a collimated output beam is emitted from one of the edge facets from the glass. The green spot projected behind a lens represents an output beam of lasing. This indicates that the output beam is highly directional and spatially coherent at a particular direction.

4. Conclusions

The spontaneous UC emissions intensity of Er^{3+} is drastically improved with the Ag NPs emerged in Ba_2LaF_7 glass ceramic for the contribution of the SPR and some of the energy transfer from Ag NPs to Er^{3+} . Meanwhile, the stimulated emission as a random lasing action is achieved in this hybrid material. It is found that the incorporation of Ag NPs is advantageous in reducing the threshold of the lasing action. Therefore, the new class of hybrid glasses allows for fiber-based devices to be developed for photonic applications or

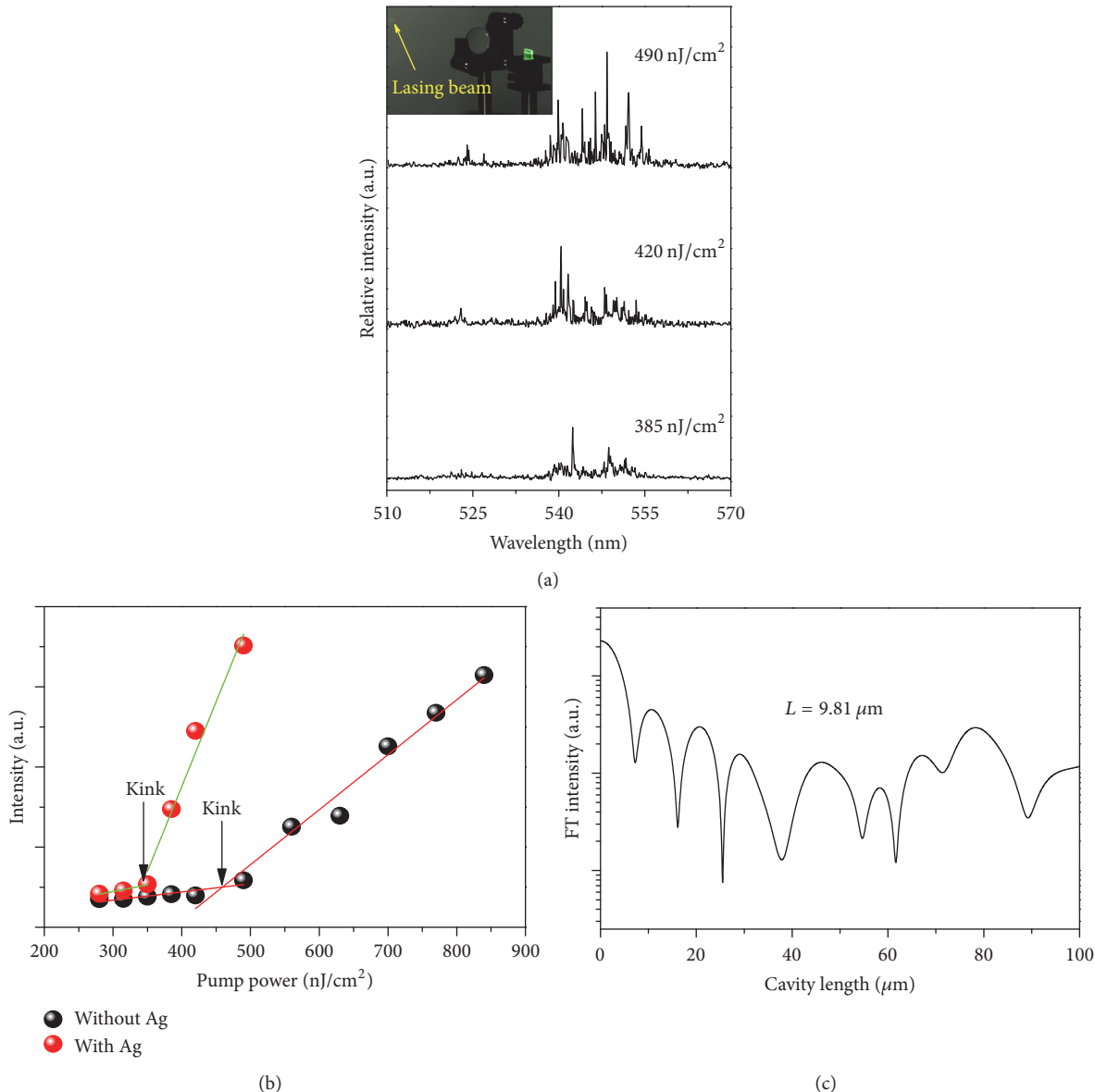


FIGURE 4: (a) Emission spectra of 0.5 Ag sample under different pump intensity of 980 nm nanosecond lasers: the inset is the photograph of 0.5 Ag sample under excitation of 980 nm nanosecond. (b) Integrated emission intensity of 0 Ag and 0.5 Ag samples versus pumping energy density. (c) Plot of Fourier transform (FT) patterns of the lasing spectra of the 0.5 Ag sample.

as a useful tool for tailoring light-nanoparticles interactions study.

Conflicts of Interest

The authors declare that they have no conflicts of interest.

Acknowledgments

This work was financially supported by the National Nature Science Foundation of China (61565009, 61308091), the Foundation of Natural Science of Yunnan Province (2016FB088), the Young Talents Support Program of Faculty of Materials Science and Engineering, Kunming University of Science

and Technology (14078342), and the Postdoctoral Science Foundation of China (2013M540720).

References

- [1] J. Zhao, X. Zheng, E. P. Schartner et al., "Upconversion nano-crystal-doped glass: a new paradigm for photonic materials," *Advanced Optical Materials*, vol. 4, no. 10, pp. 1507–1517, 2016.
- [2] J. Zhao, R. Ma, X. Chen et al., "From phase separation to nanocrystallization in fluorosilicate glasses: structural design of highly luminescent glass-ceramics," *Journal of Physical Chemistry C*, vol. 120, no. 31, pp. 17726–17732, 2016.
- [3] D. Chen, Y. Wang, Y. Yu, F. Liu, and P. Huang, "Sensitized thulium ultraviolet upconversion luminescence in $\text{Tm}^{3+}/\text{Yb}^{3+}/\text{Nd}^{3+}$

- triply doped nanoglass ceramics," *Optics Letters*, vol. 32, no. 21, pp. 3068–3070, 2007.
- [4] D. Chen, Y. Wang, N. Yu, P. Huang, and F. Weng, "Near-infrared quantum cutting in transparent nanostructured glass ceramics," *Optics Letters*, vol. 33, no. 16, pp. 1884–1886, 2008.
- [5] G. A. Kumar, C. W. Chen, J. Ballato, and R. E. Rimann, "Optical characterization of infrared emitting rare-earth-doped fluoride nanocrystals and their transparent nanocomposites," *Chemistry of Materials*, vol. 19, no. 6, pp. 1523–1528, 2007.
- [6] D. Chen, Y. Yu, P. Huang, and Y. Wang, "Nanocrystallization of lanthanide trifluoride in an aluminosilicate glass matrix: dimorphism and rare earth partition," *CrystEngComm*, vol. 11, no. 8, pp. 1686–1690, 2009.
- [7] X. Xu, W. Zhang, D. Yang, W. Lu, J. Qiu, and S. F. Yu, "Phonon-assisted population inversion in lanthanide-doped upconversion ba₂la_f7nanocrystals in glass-ceramics," *Advanced Materials*, vol. 28, no. 36, pp. 8045–8050, 2016.
- [8] P. Bharadwaj, B. Deutsch, and L. Novotny, "Optical antennas," *Advances in Optics and Photonics*, vol. 1, no. 3, pp. 438–483, 2009.
- [9] S. Chowdhury, V. R. Bhethanabotla, and R. Sen, "Silver-copper alloy nanoparticles for metal enhanced luminescence," *Applied Physics Letters*, vol. 95, no. 13, Article ID 131115, 2009.
- [10] D. G. Zhang, X.-C. Yuan, and J. Teng, "Surface plasmon-coupled emission on metallic film coated with dye-doped polymer nanogratings," *Applied Physics Letters*, vol. 97, no. 23, Article ID 231117, 2010.
- [11] N. A. Harun, M. J. Benning, B. R. Horrocks, and D. A. Fulton, "Gold nanoparticle-enhanced luminescence of silicon quantum dots co-encapsulated in polymer nanoparticles," *Nanoscale*, vol. 5, no. 9, pp. 3817–3827, 2013.
- [12] F. Nan, Z.-Q. Cheng, Y.-L. Wang et al., "Manipulating nonlinear emission and cooperative effect of CdSe/ZnS quantum dots by coupling to a silver nanorod complex cavity," *Scientific Reports*, vol. 4, article no. 4839, 2014.
- [13] G. W. Shu, C. H. Chiu, L. T. Huang et al., "Efficient energy transfer from InGaN quantum wells to Ag nanoparticles," *Physical Chemistry Chemical Physics*, vol. 15, no. 10, pp. 3618–3622, 2013.
- [14] A. P. Abiyasa, S. F. Yu, S. P. Lau, E. S. P. Leong, and H. Y. Yang, "Enhancement of ultraviolet lasing from Ag-coated highly disordered ZnO films by surface-plasmon resonance," *Applied Physics Letters*, vol. 90, no. 23, Article ID 231106, 2007.
- [15] X. Li, Y. Zhang, and X. Ren, "Effects of localized surface plasmons on the photoluminescence properties of Au-coated ZnO films," *Optics Express*, vol. 17, no. 11, pp. 8735–8740, 2009.
- [16] O. Popov, A. Zilbershtein, and D. Davidov, "Random lasing from dye-gold nanoparticles in polymer films: Enhanced gain at the surface-plasmon-resonance wavelength," *Applied Physics Letters*, vol. 89, no. 19, Article ID 191116, 2006.
- [17] Q. Qiao, C.-X. Shan, J. Zheng et al., "Surface plasmon enhanced electrically pumped random lasers," *Nanoscale*, vol. 5, no. 2, pp. 513–517, 2013.
- [18] P. Piasecki, A. Piasecki, Z. Pan, R. Mu, and S. H. Morgan, "Formation of Ag nanoparticles and enhancement of Tb³⁺ luminescence in Tb and Ag co-doped lithium-lanthanum-aluminosilicate glass," *Journal of Nanophotonics*, vol. 4, no. 1, Article ID 043522, 2010.
- [19] T. Som and B. Karmakar, "Nanosilver enhanced upconversion fluorescence of erbium ions in Er³⁺: Ag-antimony glass nanocomposites," *Journal of Applied Physics*, vol. 105, no. 1, Article ID 013102, 2009.
- [20] W. L. Barnes, A. Dereux, and T. W. Ebbesen, "Surface plasmon subwavelength optics," *Nature*, vol. 424, no. 6950, pp. 824–830, 2003.
- [21] C. D. Geddes and J. R. Lakowicz, "Metal-enhanced fluorescence," *Journal of Fluorescence*, vol. 12, no. 2, pp. 121–129, 2002.
- [22] K.-H. Su, Q.-H. Wei, X. Zhang, J. J. Mock, D. R. Smith, and S. Schultz, "Interparticle coupling effects on plasmon resonances of nanogold particles," *Nano Letters*, vol. 3, no. 8, pp. 1087–1090, 2003.
- [23] A. Bouhelier, "Field-enhanced scanning near-field optical microscopy," *Microscopy Research and Technique*, vol. 69, no. 7, pp. 563–579, 2006.
- [24] X. Zhang, L. Zhou, Q. Pang, and M. Gong, "Novel broadband excited and linear red-emitting Ba₂Y (BO₃)₂ Cl: Ce³⁺, Tb³⁺, Eu³⁺ phosphor: luminescence and energy transfer," *Journal of the American Ceramic Society*, vol. 97, no. 7, pp. 2124–2129, 2014.
- [25] L.-L. Wang, Q.-L. Wang, X.-Y. Xu et al., "Energy transfer from Bi³⁺ to Eu³⁺ triggers exceptional long-wavelength excitation band in ZnWO₄:Bi³⁺, Eu³⁺ phosphors," *Journal of Materials Chemistry C*, vol. 1, no. 48, pp. 8033–8040, 2013.
- [26] X. Xu, W. Zhang, L. Jin, J. Qiu, and S. F. Yu, "Random lasing in Eu³⁺ doped borate glass-ceramic embedded with Ag nanoparticles under direct three-photon excitation," *Nanoscale*, vol. 7, no. 39, pp. 16246–16250, 2015.
- [27] X. Meng, K. Fujita, S. Murai, T. Matoba, and K. Tanaka, "Plasmonically controlled lasing resonance with metallic-dielectric core-shell nanoparticles," *Nano Letters*, vol. 11, no. 3, pp. 1374–1378, 2011.